UNIVERSITY OF PATRAS
DEPARTMENT OF MECHANICAL ENGINEERING & AERONAUTICS
DIVISION OF APPLIED MECHANICS, TECHNOLOGY OF MATERIALS & BIOMECHANICS
LABORATORY OF APPLIED MECHANICS AND VIBRATIONS

DIPLOMA THESIS

Design, Analysis and Optimization of a 6U CubeSat using Composite Materials

Georgiou Nikolaos

1059734

Supervisor: Kostopoulos Vasilios, Professor

Thesis submitted to Department of Mechanical Engineering & Aeronautics at University of Patras

Patras, October/2022

To my parents, Politimi and Nakos

University of Patras, Department of Mechanical Engineering & Aeronautics
Georgiou Nikolaos
© 2022 – All rights reserved

UNIVERSITY OF PATRAS
DEPARTMENT OF MECHANICAL ENGINEERING & AERONAUTICS
DIVISION OF APPLIED MECHANICS, TECHNOLOGY OF MATERIALS & BIOMECHANICS
LABORATORY OF APPLIED MECHANICS AND VIBRATIONS

The present thesis was presented

by

Georgiou Nikolaos

1059734

on the 24th of October 2022

The approval of the thesis does not mean the acceptance of the writer's views. During the authorship, the principles of academic ethics have been respected.

ΠΕΡΙΛΗΨΗ

Σχεδιασμός, Ανάλυση και Βελτιστοποίηση ενός 6U Μικροδορυφόρου με χρήση Συνθέτων Υλικών

Γεωργίου Νικόλαος

Δυο από τα βασικότερα ζητήματα που απασχολούσαν την ανθρωπότητα για πολλούς αιώνες και θα συνεχίσουν να την απασχολούν, δεδομένου της συνέχισης της τεχνολογικής ανάπτυξης, είναι τόσο η δημιουργία όσο και η κατάληξη του σύμπαντος. Τα τελευταία χρόνια, η επιστήμη έχει στραφεί στον σχεδιασμό μικροδορυφόρων, οι οποίοι πέρα από την κάλυψη καθημερινών αναγκών, αποτελούν τον θεμελιώδη λίθο για την μετέπειτα ανάπτυξη καινοτόμων δορυφόρων, οι οποίοι σε κάποια μελλοντική φάση της ανθρώπινης ιστορίας θα δύνανται να δώσουν μια τελική απάντηση στα προαναφερθέντα θέματα. Η παρούσα εργασία πραγματεύεται τον σχεδιασμό ενός κυβοειδούς μικροδορυφόρου τύπου 6U-XL, κάνοντας χρήση πολύστρωτων δομών συνθέτων υλικών, ο οποίος αποσκοπεί στην μεταφορά ενός πτυσσόμενου ρομποτικού βραχίονα στο διάστημα. Σε πρώτο στάδιο, πραγματοποιείται η απαραίτητη βιβλιογραφική ανασκόπηση, ενώ αξιοσημείωτη είναι η αναφορά στην θεωρία της επιστήμης υλικών και ιδιαιτέρως των συνθέτων, τα οποία αποτελούν τόσο το παρόν όσο και το μέλλον των αεροδιαστημικών εφαρμογών. Επακόλουθα, παρουσιάζονται και σχολιάζονται επαρκώς όλα τα βασικά εξαρτήματα της δομής του μικροδορυφόρου, τα οποία σχεδιάστηκαν στο περιβάλλον του CATIA. Στην συνέχεια, εκτελούνται, εντός του πακέτου πεπερασμένων στοιχείων MSC PATRAN/NASTRAN, όλες οι απαραίτητες αναλύσεις (ταλαντωτικής συμπεριφοράς, αντοχής και ελαστικής ευστάθειας), οι οποίες τουλάχιστον υπολογιστικά επιβεβαιώνουν την ορθή λειτουργία του δορυφόρου κατά την διάρκεια της εκτόξευσης. Εν κατακλείδι, πραγματοποιείται μια απόπειρα βελτίωσης της παρούσας δομής, μέσω της μελέτης διαφορετικών πολύστρωτων δομών, αποσκοπώντας στην μείωση του συνολικού βάρους του μικροδορυφόρου, η οποία αποτελεί έναν από τους πιο κρίσιμους παράγοντες κάθε διαστημικής αποστολής.

Λέξεις κλειδιά

Μικροδορυφόροι, Σχεδιασμός με Χρήση Υπολογιστή, Ανάλυση με χρήση Πεπερασμένων Στοιχείων, Σύνθετα Υλικά, Αεροδιαστημική Μηχανική

ABSTRACT

Design, Analysis and Optimization of a 6U CubeSat using Composite Materials

Georgiou Nikolaos

Two of the most fundamental issues that have preoccupied humanity for many centuries and will continue to concern it, given the continuation of technological development, are both the creation and the end of the universe. In recent years, science has turned to the design of CubeSats, which beyond meeting daily needs, are also the cornerstone for the subsequent construction of new satellites, that will have the potential, at some later stage of the human history, to give a final answer to the aforementioned issues. The current thesis deals with the design of a 6U-XL CubeSat using laminated composite materials, which is planned to transport a deployable robotic arm in space. At a first stage, the appropriate literature overview is made, with a special reference to material science and especially to composites, which constitute both the present and the future of aerospace applications. Followingly, the primary structural components of the CubeSat, which were designed in CATIA environment, are presented and sufficiently commented. Then all the necessary analyses (modal, quasi-static, buckling and random vibrations), which confirm at least computationally the proper functionality of the satellite during the launch, are carried out in the MSC PATRAN/NASTRAN software. Finally, an attempt is made to optimize the present structure through the study of different composite materials with the aim of reducing the total weight of the satellite, which represents one of the most crucial driving-factors of every space mission.

Keywords

CubeSat, Computer Aided Design (CAD), Finite Element Analysis (FEA), Composites, Aerospace Engineering

LIST OF TABLES

Table 1: Material Requirements for Space Structures 16

Table 2: Comparison of Aluminum 6061-T6 and Aluminum 7075-T6 Properties 17

Table 3: Examples of typical 6Us chassis..... 39

Table 4: Material Properties of the FE model..... 66

Table 5: The first 10 Natural Frequencies of the Structure 69

Table 6: Quasi-Static Analyses Results (All Cases)..... 97

Table 7: Interpretation of the Buckling Load Factor (BLF) 98

Table 8: The first 10 Natural Frequencies of the Full-Aluminum Structure 112

Table 9: Comparison between Hybrid and Aluminum Structures based on the Worst Quasi-Static Scenario..... 114

Table 10: The first 10 Natural Frequencies of the Optimized Hybrid Structure 117

Table 11: Quasi-Static Analyses Results of the Optimized Hybrid Structure (All Cases)..... 119

Table 12: Mass List of the Optimized Hybrid Structure..... 123

LIST OF FIGURES

Figure 1: Artistic illustration of ESA's Rosetta approaching Comet 67P/Churyumov–Gerasimenko [2] 4

Figure 2: Small Satellites Categories [4] 5

Figure 3: Structural Types of CubeSats 6

Figure 4: Nanosatellite Launches 8

Figure 5: Types of Nanosatellite 9

Figure 6: Poly Picosatellite Orbital Deployer [8] 10

Figure 7: Isis (left) and Tyvak (right) 6U Dispensers [9] 11

Figure 8: Rails and Decks of a 2U Chassis 12

Figure 9: Full Structure of a 2U CubeSat and Antenna System (ISIS) [10] 13

Figure 10: 1U CubeSat Frame by SatPy [46] (top left), ZAPHOD - 1U CubeSat Frame [47] (top right), Chassis Walls for a 3U CubeSat by PUMPKIN [48] (bottom left), 3D Printing Lattice Structures for CubeSat Bus [49] (bottom right) 14

Figure 11: Transition from a single Lamina to a Laminated Material 19

Figure 12: Example of a Composite Sandwich 20

Figure 13: Example of a Carbon-Aramid Reinforced Epoxy 21

Figure 14: Representation of a typical Woven Composite 21

Figure 15: Properties of Several Composite Materials 23

Figure 16: Representation of an On-Axis Orthotropic Ply [11] 28

Figure 17: Representation of an Off-Axis Orthotropic Ply [11] 29

Figure 18: Transverse Cross Section of a Laminate with n- Plies [11] 30

Figure 19: Fiber Orientations in π/3 , π/4 and π/6 Quasi-Isotropic Laminates [16] 31

Figure 20: Fully Assembled View of UPSAT 33

Figure 21: UPSAT completed Structural System 35

Figure 22: Simplified Model with Solid and Surface Parts (left), Finite Element Model (right). 36

Figure 23: Pumpkin [21] (left), Nanoavionics [22] (middle), Zaphod [23](right) 38

Figure 24: EnduroSat [24] (left), Cervos [25] (middle), SM06 by spacemind [26] (right)..... 38

Figure 25: Gomspace [27] (left), ISIS [10] (right) 39

Figure 26: Fully Assembled View of the Present 6U-XL (left: Shading with Edges, right: Shading with Materials)..... 43

Figure 27: Fully Assembled View of the CubeSat's Interior 44

Figure 28: Geometrical Characteristics of the CAD's model 44

Figure 29: Center of Gravity (CAD Model – Internal View) 45

Figure 30: Main Rail (left), Intermediate Rail (right)..... 47

Figure 31: Imaginary 1U System (left), Deck - Crossmember (right)..... 49

Figure 32: Isometric View of a Side Panel 51

Figure 33: Isometric View of the Back Main Panel (left) and the Primary Part of the Front Main Panel (right) 52

Figure 34: Isometric View of a Base 54

Figure 35: Isometric View of a Piano Hinge 55

Figure 36: Isometric View of the Deployable Panel..... 56

Figure 37: A closer Inspection of the Bolted Connections 58

Figure 38: FE Model Summary 62

Figure 39: Boundary Conditions applied on the FE Model 63

Figure 40: Center of Gravity position (mm), Mass (tons) and Volume (mm^3) 64

Figure 41: Representation of the CG in the 3D Space 64

Figure 42: Manufacturing Standpoint of the Current Layup [32] 66

Figure 43: Material Properties Assignment on the Assembly 67

Figure 44: Mode Shapes of the 6U-XL CubeSat 71

Figure 45: Displacement Distributions [mm] of the 1st Case 79

Figure 46: Max Principal Stresses [MPa] (left) and Max Principal Strains [-] Distributions (right) of the 1st Case 80

Figure 47: Von Mises Stresses [MPa] on Aluminum Decks (left) and Maximum von Mises Stress [MPa] Detail (right) of the 1st Case 81

Figure 48: 1D Beam Elements (of intermediate rails) Stresses [MPa] (left) and Maximum Combined Beam Stress [MPa] Detail (right) of the 1st Case 82

Figure 49: 1D Bar Elements (of main rails and threaded rods) Stresses [MPa] (left) and Maximum Combined Bar Stress [MPa] Detail (right) of the 1st Case 83

Figure 50: Worst Margins of Safety (MOS) of Composite Parts (Tsai-Wu-EPFS Criterion) of the 1st Case 84

Figure 51: Minimum Margin of Safety Detail of the 1st Case 84

Figure 52: Displacement Distributions [mm] of the 2nd Case 85

Figure 53: Side View of the Displacement Distributions [mm] of the 2nd Case – Model Scale with a Scale Factor of 0.1 (left) and True Scale (right) 86

Figure 54: Max Principal Stresses [MPa] (left) and Max Principal Strains [-] Distributions (right) of the 2nd Case 87

Figure 55: Von Mises Stresses [MPa] on Aluminum Decks (left) and Maximum von Mises Stress [MPa] Detail (right) of the 2nd Case 88

Figure 56: 1D Beam Elements (of intermediate rails) Stresses [MPa] (left) and Maximum Combined Beam Stress [MPa] Detail (right) of the 2nd Case 88

Figure 57: 1D Bar Elements (of main rails and threaded rods) Stresses [MPa] (left) and Maximum Combined Bar Stress [MPa] Detail (right) of the 2nd Case 89

Figure 58: Worst Margins of Safety (MOS) of Composite Parts (Tsai-Wu-EPFS Criterion) of the 2nd Case 90

Figure 59: Minimum Margin of Safety Detail of the 2nd Case 90

Figure 60: Displacement Distributions [mm] on the Entire Model (left) and Internal View (right) of the 3rd Case 91

Figure 61: Max Principal Stresses [MPa] (left) and Max Principal Strains [-] Distributions (right) of the 3rd Case 92

Figure 62: Von Mises Stresses [MPa] on Aluminum Decks (left) and Maximum von Mises Stress [MPa] Detail (right) of the 3rd Case 93

Figure 63: 1D Beam Elements (of intermediate rails) Stresses [MPa] (left) and Maximum Combined Beam Stress [MPa] Detail (right) of 3rd Case 93

Figure 64: 1D Bar Elements (of main rails and threaded rods) Stresses [MPa] (left) and Maximum Combined Bar Stress [MPa] Detail (right) of the 3rd Case 94

Figure 65: Worst Margins of Safety (MOS) of Composite Parts (Tsai-Wu-EPFS Criterion) of the 3rd Case 95

Figure 66: Minimum Margin of Safety Detail of the 3rd Case 95

Figure 67: BLF and First Buckling Eigen-Mode Shape of the 1st Load Case 100

Figure 68: BLF and First Buckling Eigen-Mode Shape of the 2nd Load Case 100

Figure 69: BLF and First Buckling Eigen-Mode Shape of the 3rd Load Case 101

Figure 70: First Buckling Eigen-Mode Shape Detail of the 3rd Load Case 101

Figure 71: Random Vibration Input 103

Figure 72: PSD (X-Axis) Results 105

Figure 73: PSD (Y-Axis) Results 105

Figure 74: PSD (Z-Axis) Results 106

Figure 75: Displacement Output for the Z-Axis Loading Case 106

Figure 76: RMS Displacements [mm] for the X-Axis Loading Case (X-Component [left], Y-Component [middle], Z-Component [right]) 107

Figure 77: RMS Displacements [mm] for the Y-Axis Loading Case (X-Component [left], Y-Component [middle], Z-Component [right]) 108

Figure 78: RMS Displacements [mm] for the Z-Axis Loading Case (X-Component [left], Y-Component [middle], Z-Component [right]) 108

Figure 79: RMS von Mises Stresses [MPa] (left) and Maximum Combined RMS Bar Stresses [MPa] (right) of the X-Axis Loading Case 109

Figure 80: RMS von Mises Stresses [MPa] (left) and Maximum Combined RMS Bar Stresses [MPa] (right) of the Y-Axis Loading Case 110

Figure 81: RMS von Mises Stresses [MPa] (left) and Maximum Combined RMS Bar Stresses [MPa] (right) of the Z-Axis Loading Case 110

Figure 82: Center of Gravity position (mm), Mass (tons) and Volume (mm^3) of the Full-Aluminum Structure 112

Figure 83: Fundamental Frequency's Mode Shape of the Full-Aluminum Structure 113

Figure 84: Center of Gravity position (mm), Mass (tons) and Volume (mm3) of the Optimized Hybrid Structure 116

Figure 85: Mode Shapes of the Optimized Hybrid Structure 118

Figure 86: Worst Margins of Safety (MOS) of Composite Parts (Tsai-Wu-EPFS Criterion) during the Worst-Case Scenario (Y-Axis Loading) of the Optimized Hybrid Structure 121

Figure 87: Minimum Margin of Safety detail during the Worst-Case Scenario (Y-Axis Loading) of the Optimized Hybrid Structure 121

Figure 88: Mass Percentage of each Component of the Optimized Hybrid Structure..... 123

Figure 89: Mass Percentage of each Material used in the Optimized Hybrid Structure..... 123

SYMBOLS

g (m/s^2)	Gravitational Acceleration
σ (MPa)	Stress
ε (-)	Strain
C	Stiffness Tensor
S	Compliance Tensor
γ (-)	Engineering Strain
E (MPa)	Young's modulus
G (MPa)	Shear Modulus
v (-)	Poisson's Ratio
T_σ	Transformation Matrix for Stresses
T_ε	Transformation Matrix for Strains
Q (N/m^2)	Reduced Stiffness Matrix
N (N/m)	Reduced Force Resultants
M (N)	Reduced Moment Resultants
ε^o (-)	Membrane Strain
k (1/m)	Bending Strain
A (N/m)	Extensional Stiffness Matrix
B (N)	Coupling Stiffness Matrix
D (Nm)	Flexural Stiffness Matrix
M2 (mm)	Outer Diameter of a Screw (2mm)
Φ2 (mm)	Inner Diameter of a Threaded Hole (2mm)
ρ (kg/m^3)	Density

X_t (MPa)	Longitudinal Tension Stress Limit
Y_t (MPa)	Transverse Tension Stress Limit
X_c (MPa)	Longitudinal Compression Stress Limit
Y_c (MPa)	Transverse Compression Stress Limit
M (kg)	Mass Matrix
K (N/m)	Stiffness Matrix
u (mm)	Displacement
ω_n (rad/s) or f (Hz)	Natural Frequency
φ_n (-)	Eigen-Mode
I	Identity Matrix
F	Forces Vector
σ_y	Elastic Stress Limit
σ_v	Von Mises Stress
F_{ij}	Failure Tensors
F_{12} (1/MPa^2)	Interaction Term
BLF or λ (-)	Buckling Load Factor
λ_{cr} (-)	Critical Buckling Load Factor
***G* (kg)**	Geometric Matrix
δ_b (-)	Buckling Eigen-Mode
F_{ref} (N)	Reference Buckling Load
F_{cr} (N)	Critical Buckling Load

ABBREVIATIONS

ESA	European Space Agency
NASA	National Aeronautics and Space Administration
SSDL	Space Systems Development Laboratory
U	U-class Spacecraft
GPS	Global Positioning System
POD	Picosatellite Orbital Deployer
P-POD	Poly Picosatellite Orbital Deployer
COTS	Commercially Off-The-Shelf
AL	Aluminum
PMC	Polymer Matrix Composites
MMC	Metallic Matrix Composites
CMC	Ceramic Matrix Composites
FRP	Fiber Reinforced Plastic
CLPT	Classical Laminated Plate Theory
UPSAT	University of Patras SATellite
CFRP	Carbon Fiber Reinforced Polymer
PCB	Printed Circuit Board
QUAD4	Surface Finite Element with 4 Nodes
RBE2	Rigid Body Element
MPC	Multi Point Constraints
DOF	Degrees Of Freedom
CAD	Computer Aided Design

FEA	Finite Element Analysis
FE	Finite Element
1-2-3D	One-Two-Three Dimensional
C.O.G or CG	Center Of Gravity
EPFS	Elliptic Paraboloid Failure Surface
UD	Unidirectional
SR	Strength Ratio
SF	Safety Factor
RF	Reserve Factor
MOS	Margins Of Safety
FPF	First Ply Failure
BLF	Buckling Load Factor
PSD	Power Spectral Density
Grms	Root Mean Square Acceleration
RMS	Root Mean Square

CONTENTS

ΠΕΡΙΛΗΨΗ..... V

ABSTRACT..... VII

LIST OF TABLES..... IX

LIST OF FIGURES..... XI

SYMBOLS..... XVII

ABBREVIATIONS..... XIX

CONTENTS..... XXI

PREFACE..... 1

1.0 INTRODUCTION..... 3

1.1 HISTORY OF SATELLITES..... 3

1.2 MICRO-SATELLITES OVERVIEW..... 5

1.3 CUBESATS..... 6

1.3.1 Scope Of CubeSats..... 7

1.3.2 Deployment System (POD)..... 10

1.3.3 General Design Specifications..... 11

1.3.4 Structure..... 12

1.3.5 Materials..... 15

1.3.6 Mechanics of Composites..... 24

1.3.7 The UPSAT Project..... 33

2.0 COMPUTER AIDED DESIGN (CAD) PHASE..... 37

2.1 6U CUBESAT STRUCTURES..... 37

2.2 DESIGN SPECIFICATIONS AND OPERATIONAL REQUIREMENTS FOR A 6U-XL CUBESAT 39

2.3 6U-XL STRUCTURE COMPONENTS 41

2.3.1 Rails 46

2.3.2 Decks 48

2.3.3 Side Panels 50

2.3.4 Main Panels 51

2.3.5 Top and Bottom Base 53

2.3.6 Deployment System 54

2.3.7 Deployable Panel 55

2.4 ASSEMBLY 56

3.0 FINITE ELEMENT ANALYSIS (FEA) PHASE 59

3.1 SIMULATION APPROACH 59

3.2 COMPUTATIONAL MODEL 62

3.3 MATERIAL PROPERTIES AND COMPOSITES MODELING 65

3.4 MODAL ANALYSIS 68

3.5 QUASI-STATIC ANALYSIS 72

3.5.1 1st Quasi-static case with -30g inertial load on xx direction 79

3.5.2 2nd Quasi-static case with -30g inertial load on yy direction 85

3.5.3 3rd Quasi-static case with -30g inertial load on zz direction 91

3.5.4 Conclusions of the Quasi-static Analyses 96

3.6 BUCKLING ANALYSIS 98

3.7 RANDOM VIBRATION (PSD)..... 103

4.0 OPTIMIZATION..... 111

4.1 COMPARISON BETWEEN ALUMINUM AND HYBRID STRUCTURES 111

4.2 OPTIMIZED HYBRID STRUCTURE MADE OF UD CELION GY-70/EPOXY..... 114

4.2.1 Optimization Remarks..... 122

5.0 CONCLUSIONS AND DISCUSSION..... 125

5.1 CONCLUSIONS..... 125

5.2 FUTURE WORK..... 126

REFERENCES..... 127

APPENDIX A..... 133

APPENDIX B..... 135

APPENDIX C..... 3

PREFACE

On the completion of my Diploma Thesis, I feel the need to express my gratitude to the people that helped and motivated me to successfully reach this point.

Firstly, I would like to thank my supervisor, *Professor Vasilios Kostopoulos*, for the collaboration we had during this year and for encouraging me to deal with the design of composite structures. I would also like to thank *Professor Vaios Lappas* for introducing me to the world of space technologies and for suggesting me the current topic, which I loved to work from start to finish. Additionally, i can't help but mention *Professor Theodoros Phillipidis*, who guided me on the demanding path of the design with composite materials and without a question I owe all the acquired knowledge about this field entirely to him.

Furthermore, I would like to express my gratitude to *Andreas Ampatzoglou*, whose PhD thesis related to UPSAT became my inspiration. Undoubtedly, one of the most important people to whom I owe my deepest thanks, is *George Moraitis*. His constant guidance and support since our very first meeting back in April 2021, played a crucial role and led to the completion of the present thesis. Thank you for taking time out of your personal agenda to help me. It was a challenging period, but you made it easier.

Last but not least, I would like to thank my family for their unfaltering support and belief in me, which shaped the person that I am today. Words cannot express how grateful I am.

1.0 INTRODUCTION

1.1 History Of Satellites

It is a fact that the idea of a man-made satellite has been around for a long time. In 1610 *Johannes Kepler*, who was a German astronomer, uses for the first time, the term 'satellite' to describe the moons orbiting Jupiter. Some years later, Sir *Isaac Newton* publishes *Principia* in which he states the three laws of motion and describes universal gravity, which played a crucial role for our following understanding of rockets, satellites, and orbits. In addition to the above, in 1879 *Jules Verne* published a book called '*The Begum's Fortune*', that referred to the first fictional depictions of satellites being launched into orbit.

In 1903 *Konstantin Tsiolkovsky* proposes the use of rockets to launch spacecrafts. He calculated the orbital speed required for a minimal orbit around the Earth at 8 km/s and wrote that a multi-stage rocket fueled by liquid propellants could be used to achieve this. Several years later, *Arthur C. Clarke*, who was a science fiction writer as well as an inventor, publishes an article that shows how geostationary satellites could be used for worldwide radio and television broadcasts and communication.

The first artificial satellite, Sputnik 1, was launched by the Soviet Union in 1957 and had a mass of 83.6 kg, orbiting elliptically the Earth at a height between 215 and 939 km. After that, NASA launched Tiros-1, which was the first weather satellite, and also Tekstar-1, that broadcasted the first live transatlantic telecast.

A remarkable date was 1979, when the European Space Agency launches Ariane-1, which is designed primarily to put two telecommunications satellites into orbit and created that way ESA's space program that continues into the present. In the middle of the 90s the first Global Positioning System constellation, that provides location and time information in all weather, anywhere on or near the Earth, becomes operational [1].

In March of 2004, ESA launches ‘Rosseta’, a space probe, from French Guiana. On 6 August 2014, the spacecraft Rosetta becomes the first to catch up with a comet and land its lander module called ‘Philae’, on the comet 67P/Churyumov-Gerasimenko. From the collected data, scientists found out that Earth's water is unlikely to have originated from comets like 67P.



Figure 1: Artistic illustration of ESA’s Rosetta approaching Comet 67P/Churyumov–Gerasimenko [2]

1.2 Micro-Satellites Overview

Nowadays, more than 7000 individual satellites are in space, according to the Index of *«Objects Launched into Outer Space»*, maintained by United Nations Office for Outer Space Affairs [3]. As understood, the dependence of various industries upon the satellite data has made the numbers go up every year. With time, some of the satellites have become increasingly large and powerful, making their cost unbearable, especially for small companies that target to invest on such projects. Therefore, small satellites meet some success for lower cost spatial missions. In general, they can be categorized according to their mass into 4 classes as presented in Figure 2 .

Class	Wet Mass (kg)
Minisatellite	100 - 500
Microsatellite	10 - 100
Nanosatellite	1 - 10
Picosatellite	0.1 - 1

Figure 2: Small Satellites Categories [4]

The main advantage of small satellites, as said before, is the reduction in cost associated with access to space. The elements contributing to this philosophy are low launch costs, a short design, build and test period, a less complex ground interface and operations, and the recognition of a means of testing new spacecraft technologies in a relatively low financial risk environment [5].

To conclude, the era of nanosatellites is still to come, while humanity is only in the beginning of a big future. Greatly more launches, novel technologies and especially miniaturized subsystems and payloads will pave the way of thrilling exploration missions all over the Solar System and will give us also the opportunity to visit many more moons and asteroids. Many missions that were thought to be impossible with small satellites, such as CubeSats, even a few years ago are now being demonstrated or planned and as NASA Associate Administrator, *Dr. Thomas Zurbuchen*, once said: *"Just because a spacecraft is small, it doesn't make it easy. A highly constrained spacecraft can push the engineering, push the ingenuity of the team in a way that, in every way, is comparable to some of these big missions that we're doing."* [6]

1.3 CubeSats

The CubeSat concept and program started in 1999 at SSDL of Stanford University under the leadership of Robert J. Twiggs. A CubeSat, also known as U-class spacecraft, is a miniaturized satellite made of multiple cubic units of 10cm x 10cm x 10cm. One of the simplest categories is the 1U CubeSat that consists of one cubic block and weights about 1kg. Depending on the purpose of each mission there can be stacked more than one 1U units and form a new type of CubeSat, such as a 2U,3U,6U etc. For example, a 2U CubeSat has 20x10x10 cm size, whereas a 3U has 30x10x10 cm size, and their weights increase respectively. These little satellites tend to hitch a ride into space using extra space available on rockets, meaning lots of launch opportunities and low launch cost. In the Figure 3 that follows, one can see some of the most known types of CubeSats [7].

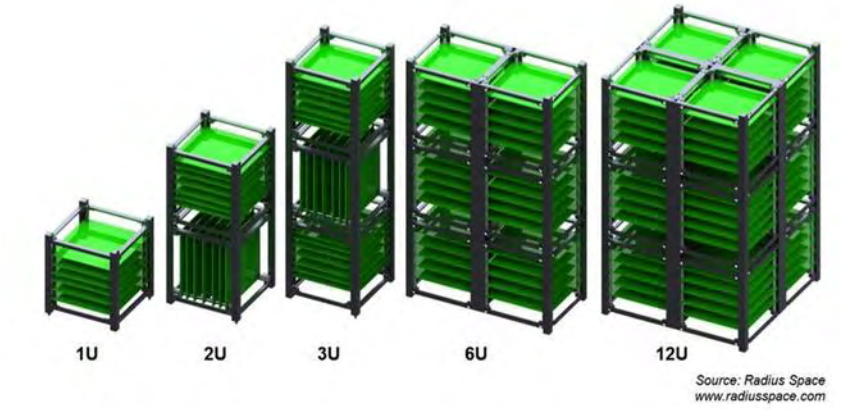


Figure 3: Structural Types of CubeSats

1.3.1 Scope Of CubeSats

In recent years, CubeSats have become a unique tool in the scientific community. Firstly, they can be used to missions that are focused to technology demonstration. Moreover, through the small instruments that they curry, there can be experiments or measurements from the harsh environment of space, that can validate the functionality of the structure or its materials and also deem their readiness to be integrated into a more complex space mission.

Except of that, CubeSats can also be used for scientific reasons such as weather forecasts, via imaging clouds and measuring temperature and rainfall. They are applied also for solar radiation studies, monitoring of climate change and even deeper understanding of the earth's magnetic field, that could be drive the scientist to predict its fluctuations in order to improve earthquake detection.

Additionally, especially these days there are many educational projects, runned by universities all around the world, that are related to CubeSats and provide students with a unique hands-on experience in developing space missions from design, to launch and operations. In that way, they can easily be not only applied but also evolved on the educational field.

Lastly, they can be used for commercial applications, with most known the scope of telecommunications for instance television, phone, or internet transmissions. CubeSats are also accustomed to GPS services or to remote sensing in order to obtain information for a highflying aircraft for example. Furthermore, they usually carry high precision cameras, with which they are imaging not only Earth, but also space objects, other planets or even nebulas.

As it can be seen on the graph in Figure 4, the number of nanosatellites sent into space every year has considerably increased since 2012 and the number of announced launches for this year has been exploded. According to Figure 5, it is a fact that, 3U CubeSats are the most famous types worldwide, occupying the first place in terms of launches, while their planned launches tend to increase their total number to 1385. Nevertheless, it seems that in recent years and especially in the future, the scientific community will turn into 6Us, whose number will tend to 460 till the end of 2025 [6].

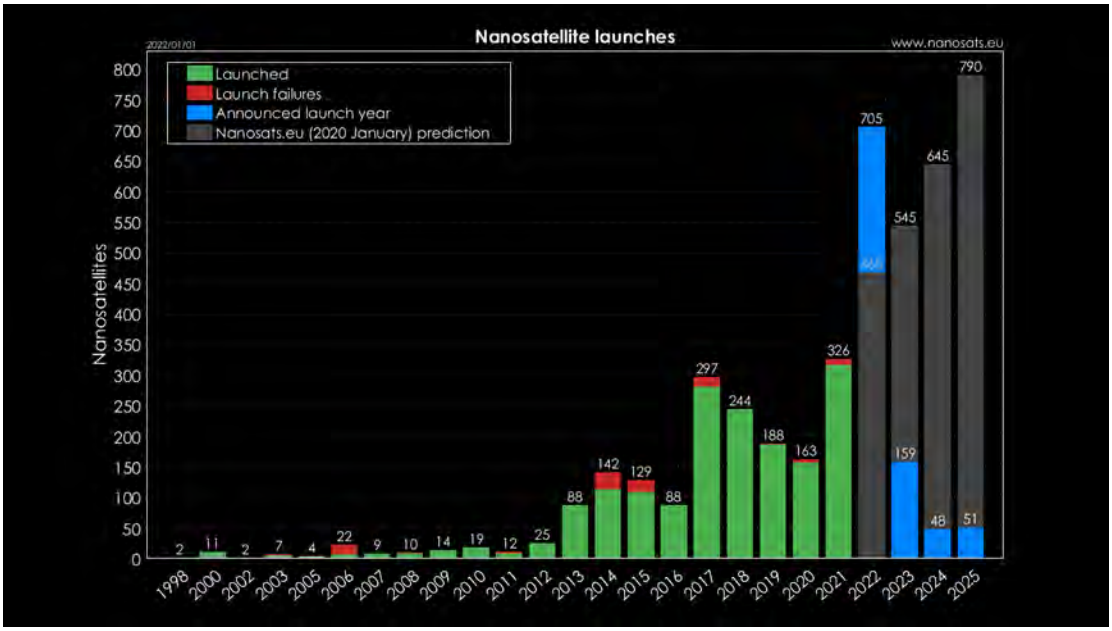


Figure 4: Nanosatellite Launches

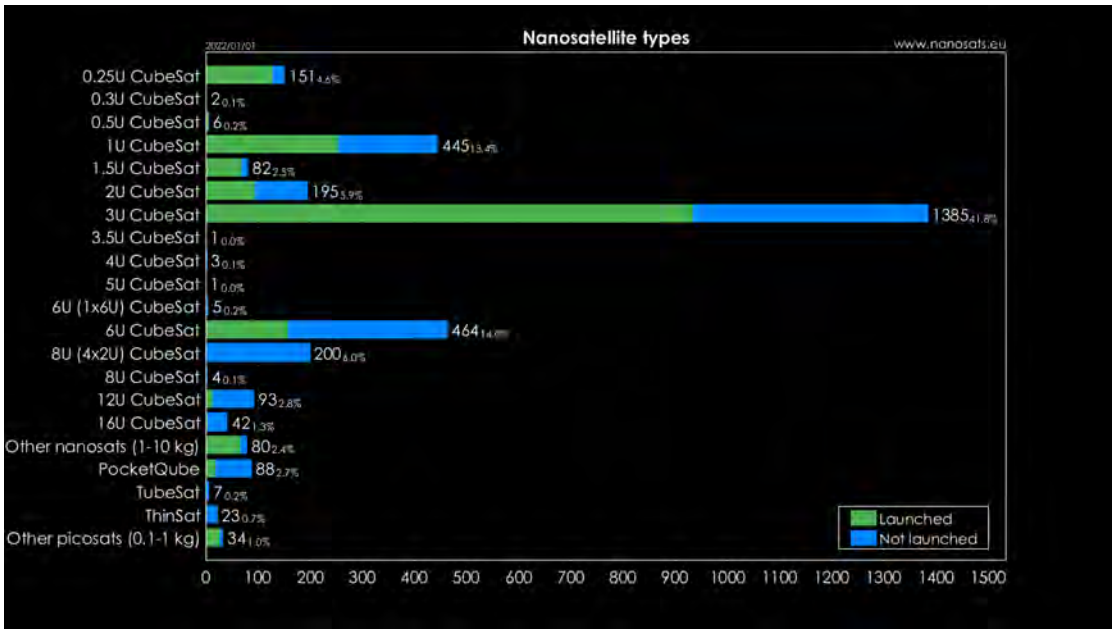


Figure 5: Types of Nanosatellite

1.3.2 Deployment System (POD)

During launch, CubeSats are stacked inside a standard deployment system, better known as POD (Picosatellite Orbital Deployer), that ejects them after reaching orbital altitude. The POD, also called dispenser, plays a critical role as the interface between the launch vehicle and CubeSats. Moreover, it minimizes any potential interactions with the primary payload(s) on a launch vehicle by physically enclosing the CubeSats and requiring that they be launched in a dormant "off" state. In this way, PODs ensure the safety and success of CubeSat missions.

Originally, there was only the P-POD used, which can contain up to three 1U CubeSats, or a single 3U, but is not compatible with bigger satellites. Fortunately, multiple companies like ISIS or Tyvak are developing 6U dispensers which are represented in Figure 7.

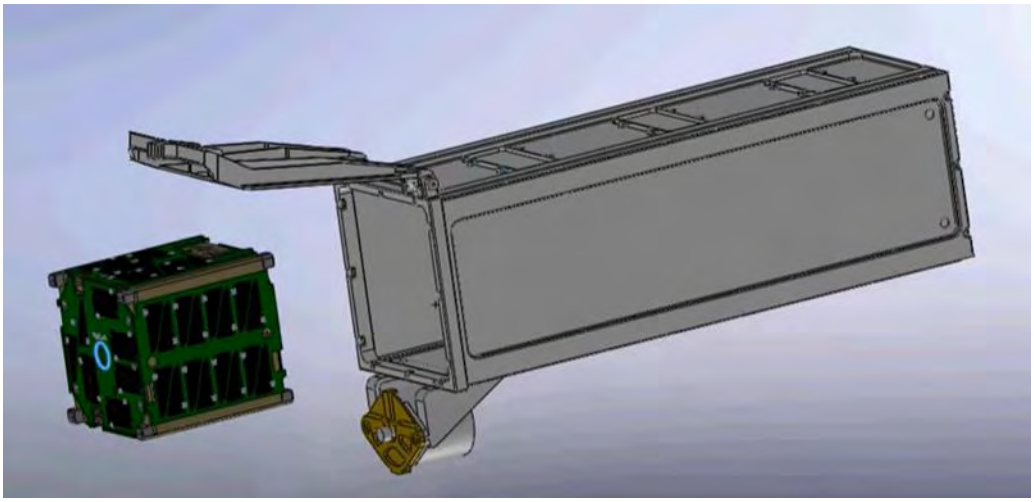


Figure 6: Poly Picosatellite Orbital Deployer [8]

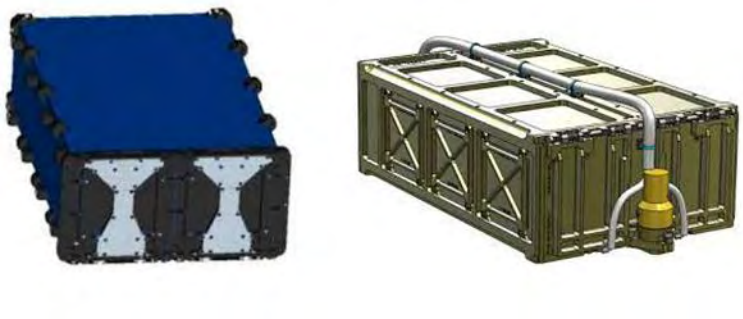


Figure 7: Isis (left) and Tyvak (right) 6U Dispensers [9]

1.3.3 General Design Specifications

Every CubeSat must be complied with strict design specifications in order to ensure its compatibility with the separation module (POD). These specifications are mainly related to the geometrical as well as the physical characteristics of the satellite. Some of the most important specifications, taking a 6U CubeSat as an example are mentioned below[1]. It is easily understood that similar specifications must also be followed by any other CubeSat type, with the main difference appearing in the mass limit.

- All parts shall remain attached to the CubeSats during launch, ejection, and operation. No additional space debris will be created.
- Rails shall have a minimum width of 8.5mm
- At least 75% of the rail will be in contact with the 6U Dispenser rails. 25% of the rails may be recessed, and no part of the rails will exceed the specification
- The maximum mass of a 6U CubeSat shall be 12.00 kg
- Typically, Aluminum 7075, 6061, 6082, 5005, and/or 5052 are used for both the main CubeSat structure and the rails.

[1] For the full list of requirements see [9].

1.3.4 Structure

As it is commonly obvious, the CubeSat structure is the most important and crucial part of the satellite. Generally, the purpose of the structure is to provide a simple and stiff frame that can withstand the launch loads and create a safe operational environment for all the subsystems as well as the payload.

The frame, also known as 'chassis', of the CubeSat usually consists of 4 rails that support the entire structure of the satellite and also connect it to the deployment system (better known as POD), that was analyzed on a previous subchapter. Besides them, there are also some crossmembers, that are intended to connect the rails together and transfer the loads to the frame. They are often known as 'decks' and generally are made of aluminum in order to increase the stiffness of the structure. Sometimes, crossmembers are used as connectors for the placement of electronic boards, that are represented with green color on Figure 3. For better understanding, Figure 8 is also included, where rails can be seen with black whereas decks, that are screwed to them, with grey color.



Figure 8: Rails and Decks of a 2U Chassis

Although, rails and decks play a major part for any CubeSat, there should be some extra components that surround the structure, so that they will offer protection to the inside of the satellite, while it is either in the POD or in space. These are known as panels, and one of them is shown characteristically in the left side of Figure 9. Panels are also connected to the rails and as understood, there are 4 of them on a typical structure, thus formed the chassis wall of a CubeSat. Additionally, there are also a bottom and a top panel (base) that enclose the entire structure. It is a common fact, that many designers take advantage of them for mounting antennas or other parts such as solar panels, that can be deployed after the launch.

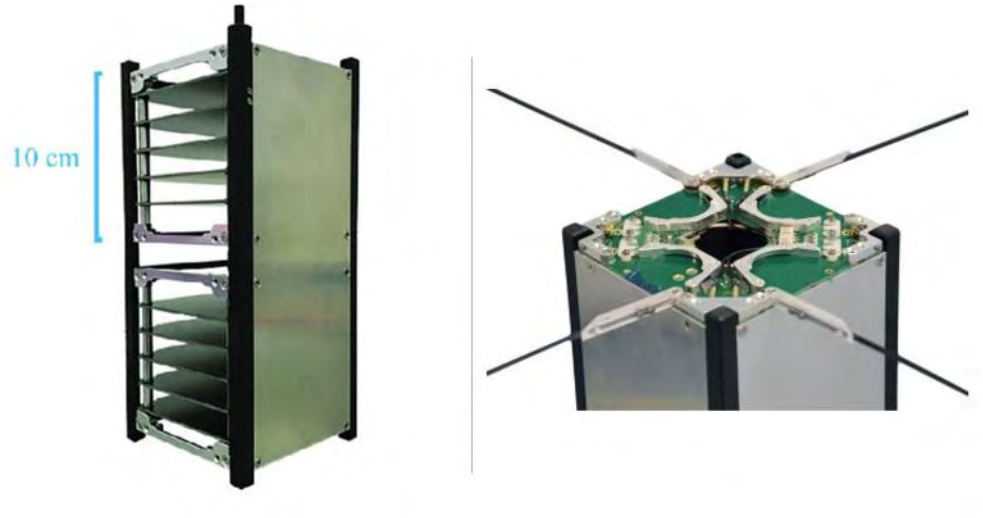


Figure 9: Full Structure of a 2U CubeSat and Antenna System (ISIS) [10]

At this point it is worth noting, that there may be multiple design philosophies according to the structure and its components, as long as the specifications of the POD are met. That's why it is quite common to have different number and formation of decks in relation to what is represented on Figure 3, even to have more than four rails, event that usually occurs in larger types of CubeSats. However, one of the most common differences between CubeSats of the same type, is the panel design approach. Multiple reasons, such as materials, shape, dimensions, mass, mission's purpose, and external loads can affect it, hence designers should make the most suitable "trade off" choice for achieving the most economic, easily manufacturing - assembling and at the same time best structural solution.

Furthermore, the use of COTS can also dramatically reduce the cost design. Several COTS are available for all Units, currying all the necessary cut outs and slots for every subsystem. In the end some of the most known or breakthrough panel design approaches are represented on the following images.

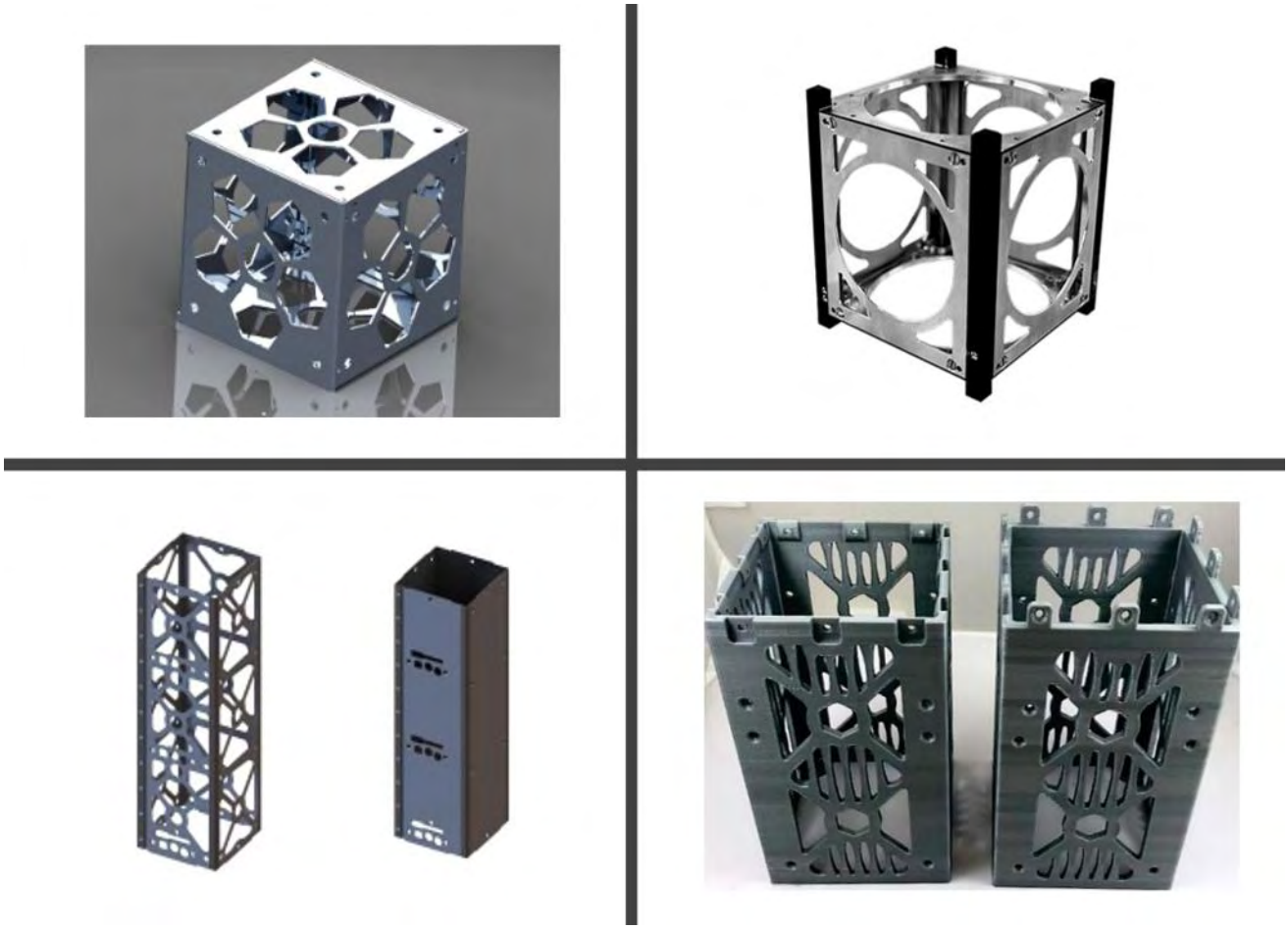


Figure 10: 1U CubeSat Frame by SatPy [46] (top left), ZAPHOD - 1U CubeSat Frame [47] (top right), Chassis Walls for a 3U CubeSat by PUMPKIN [48] (bottom left), 3D Printing Lattice Structures for CubeSat Bus [49] (bottom right)

1.3.5 Materials

It is an undoubted fact that the material selection becomes one of the most important concerns for an engineer during the design phase of any mechanical structure. A wrong choice can lead to many significant problems such as excessive costs, low strength, oversized parts, or incompatibility between components of an assembly, that can even change the entire design approach. That's why it is crucial to select the most suitable material depending on the structure's application region.

The materials used in space are the most advanced materials that scientists and engineers have developed, while currently, research groups work on the testing and manufacturing of new materials that have even more effective properties than ever before. As for the CubeSats, their structure should be made of lightweight materials to minimize total mass and gaining the opportunity for carrying heavier payloads, always below the limit set by each mission.

Space structures must be able to withstand a very harsh environment, as said before. They operated into a temperature environment with huge temperature changes between -120 ^{o}C and +125 ^{o}C due to their orbital motion around the Earth, that can cause it to expand and contract. As a result, scientist consider a material's ability to maintain its size and shape despite temperature changes, better known as material's environmental stability.

In addition to temperature variations, the launch can put a material under up to three times the force of gravity (3g), meaning that each component will be three times heavier as it was on Earth. In a few words, the forces that act on the CubeSat can tear apart the weaker structures, hence every material on it must maintain its integrity and not break under these extreme external loads. Apart from that, it is important to consider many other properties such us stiffness, density, fracture toughness, thermal, electrical as well as magnetic properties, availability, manufacturing, and cost.

Table 1: Material Requirements for Space Structures

Categories	Requirements
Lightweight Structure	• High Specific Strength • High Specific Stiffness • High Stability
Thermal Stability	• Low Thermal Expansion • Thermal Conductivity • Resistance on extreme Temperature Variations
Manufacturing	• Cost • Availability • Ease of Fabrication

1.3.5.1 Metal Alloys

Aluminum alloys are often strong and lightweight enough to be functional on space structures and satellites. The combination of high stiffness and strength to weight ratio, ease to fabricate into various and complex forms, effective cost, high ductility, availability, recyclability, and ease to be joinable with other parts or to different materials by all major methods such as welding, bolding or adhesive bonding makes it one of the best choices for most space and aeronautic structures. Two common types of aluminum alloys, that are widely used in space industry are Aluminum 6061-T6 and Aluminum 7075-T6. Majority of the commercial off the self-structures are made of either Al 6061 or Al 7075. More specifically, Al 7075 is harder and has much higher tensile strength, while 6061 is weldable, has slightly lower cost and is easier to be machined. If welding is out of the question, then Al 7075 is all around more desirable on this kind of structures.

Table 2: Comparison of Aluminum 6061-T6 and Aluminum 7075-T6 Properties

Properties	Aluminum 6061-T6	Aluminum 7075-T6
Density (g/cm^3)	2.7	2.81
Yield Tensile Strength (MPa)	276	503
Ultimate Tensile Strength (MPa)	310	572
Fatigue Strength (MPa)	96	160
Shear Strength (MPa)	210	330
Elastic Modulus (GPa)	68.9	71.7
Poisson's Ratio	0.33	0.33
Melting Onset (^oC)	582	477
Melting Completion (^oC)	652	635
Thermal Conductivity (W/m-K)	167	130
Elongation at Break (%)	17	7.9
Hardness (Brinell)	95	150
Machinability	Good	Fair

On the other hand, many space applications make use of titanium alloys due to their substantially greater yield strength comparing to aluminum. However, their high density and the fact that they are more difficult to be machined, are some considerable disadvantages. Most of the structural steels are avoided due to their magnetic properties, except of austenitic stainless steels, which are non-magnetic but have lower specific stiffness than aluminum alloys. Nonetheless these materials, can still be applied in instances where titanium is not necessary because of its machining or the temperature environment.

1.3.5.2 Composites

Composite Materials are quickly becoming the top choice for aerospace structures. A composite is essentially a physical or mechanical combination of two or more constituents or phases with purpose of creating a new material with unique and simultaneously intermediate properties of the raw materials. During the fabrication of a composite material, any chemical reactions between the component materials (constituents) should be of limited extent to ensure the chemical stability of the final product. Scope of using composites is mainly to achieve high specific properties, fact that make them superior in comparison with the metal alloys. In case that composite consists only of two components (phases), one can discern a continuum phase, that's commonly known as matrix and a dispersed phase, also known as reinforcement. During the design process, it is necessary to consider that the composite has also been into a mechanical stability, in order to assume continuity of stresses and strains throughout its extent.

Depending on the type of matrix, they are divided into the following categories:

1. Polymer Matrix Composites (PMCs)
2. Metallic Matrix Composites (MMCs)
3. Ceramic Matrix Composites (CMCs)

The basic goals of the continuous phase (matrix) are to:

- Hold the reinforcements together.
- Protect the reinforcements from external factors.
- Transfer the load to the reinforcements.
- Develop bonds with the reinforcements.
- Solidify in a short time and at a relatively low temperature.
- Not damage the surfaces of the reinforcements.
- Not develop any other chemical reactions apart from the bonding.

Despite the importance of the matrix, the most significant phase is that of the reinforcement. In most of the cases, it has better mechanical properties from those of matrix and affects in a much greater scale the final behavior of the composite. The topologically direction of the reinforcement should agree in general with that of the external loads that act on the composite, in order to provide it with the appropriate strength and stiffness to be able to withstand them. Regarding the geometry of the reinforcement, composites can be divided into the following categories:

1. Fiber Reinforced Composites (short fiber composites, long fiber composites, aligned or random)
2. Particulates

Through a macroscopic overview, a composite can also be categorized as:

- **Laminate**

This group of composites consists of multiple laminas (layers or plies), where long fibers are arranged parallelly and usually in different directions per layer. It is noteworthy that the diameter of every fiber is around 10μm, while the thickness of every lamina ranges from 0.1mm to 0.25mm. The use of different fiber orientations allows the creation of a lay-up (laminate), which can effectively absorb the effect of random loads.

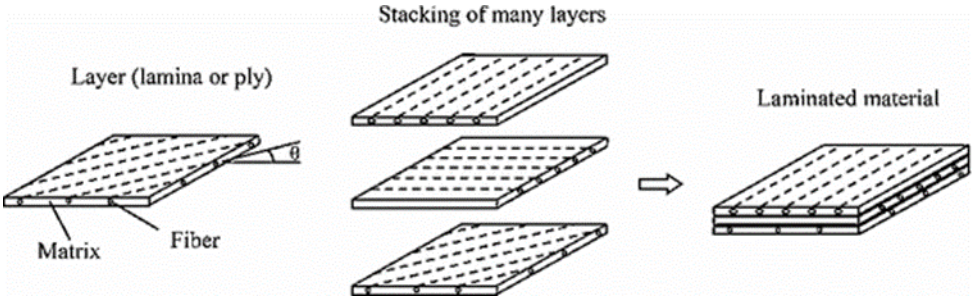


Figure 11: Transition from a single Lamina to a Laminated Material

- **Sandwich**

Sandwiches are usually composed of two skins (facings) that are made of either aluminum, titanium alloys, or laminated FRPs and carry essentially all the in-plane load. Between them, there is a third lightweight low-density material, which receives mainly transverse shear loads and removes the facings from the middle plane of the plate. This component is known as core and is often made of polymeric foams or honeycomb structures from aluminum, polymer or FRP. In addition to them, there are also some structural adhesive films that connect skins and core together.

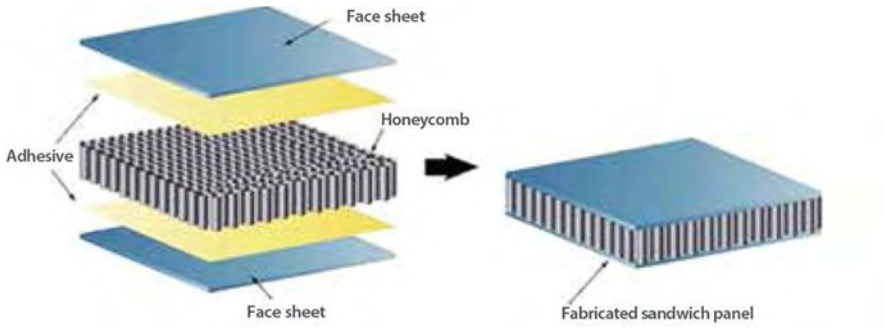


Figure 12: Example of a Composite Sandwich

- **Hybrid**

Composites of this group include two or more types of reinforcement, which differ from each other either in physical properties, geometry, or both. The most common hybrid composites are carbon-aramid reinforced epoxy (which combines strength and impact resistance) and glass-carbon reinforced epoxy (which gives a strong material at a reasonable price). Generally, hybrid composites are used when a combination of properties of different fibers wats to be achieved or when longitudinal as well as lateral mechanical performances are required.

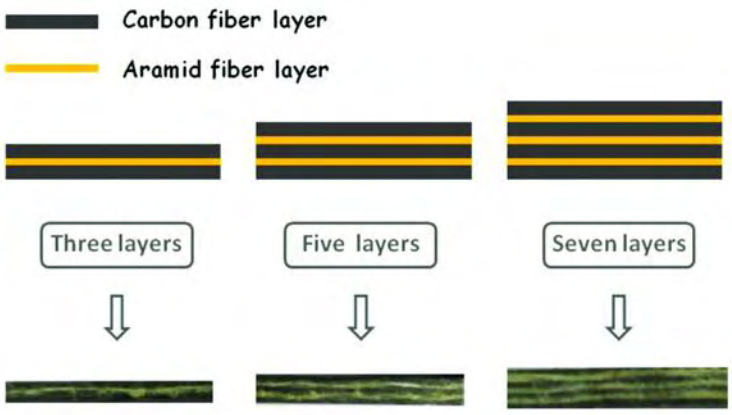


Figure 13: Example of a Carbon-Aramid Reinforced Epoxy

- **Woven**

Woven fabrics are produced by the interlacing of warp (0 degrees) and weft (90 degrees) fibers in a regular pattern or weave style. There can be multiple weave styles and each of them directly affects the ability of a fabric to conform to a complex structure, its surface smoothness and stability. In highly engineered applications, fibers can also be placed through the thickness direction (z-yarn) of the fabric, offering it the ability to withstand out of plane loads. In these cases, fabrics can have thickness up to 10 mm.

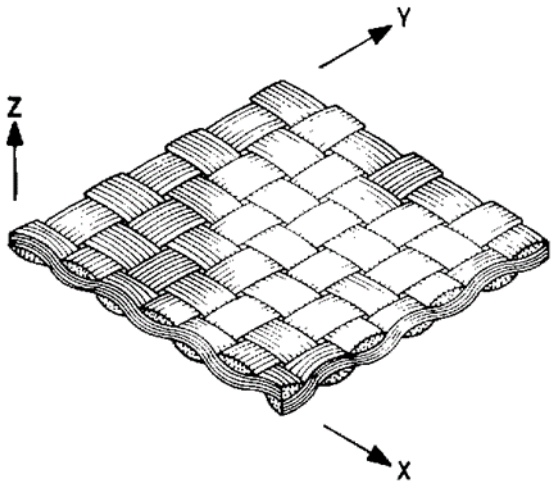


Figure 14: Representation of a typical Woven Composite

In general, the high specific stiffness and strength properties that composites materials offer, make them superior choice for space applications and their use continues to grow. Characteristically, the specific tensile strength of a typical carbon fiber is 3.8 times, while the specific stiffness of it is around 1.7 times that of aluminum. Carbon fiber laminates are used extensively on satellites and payload support structures such as telescopes, antennas, and reflectors. Typical bus structures are built from aluminum honeycomb sandwich panels with either carbon fiber or aluminum face sheets. Metal matrix, Carbon-Carbon, and Ceramic-Matrix composites are best for high temperature applications, such as re-entry vehicle skins, since they can withstand temperatures more than 2300 F. Typical examples are the Space Shuttle, that used carbon-carbon panels on the nose and the wing, and the Apollo capsule, which made use of carbon fiber reinforced phenolic for its heat shield.

Despite their many advantages, composite materials have also some serious disadvantages that must be taken into consideration. Firstly, they require very high precision in their production, so that they can acquire the best possible properties close to the ideal ones, which in other words means high manufacturing cost. For instance, a fiber placement error of the order of 5^{o}, is able to reduce the young modulus of a carbon fiber composite (T300/N5208) up to 16%. Additionally, one need to be very careful when connecting them, via bolts or screws with other parts. Moreover, holes and gaps destroy the continuation of fibers thus forming starting points of cracks which may lead later to failure. When talking about laminates, it is crucial for an engineer to choose the most effective lay-up, according to the loads of each application, so that the majority of them will be received from the fibers and not the matrix, which is usually made of resin and has significantly reduced properties. Other problems, such us high creep levels, low resistance to mechanical wear and the sensitive behavior mainly of the resin in extreme environments should be noted. Nevertheless, nowadays many of these disadvantages are being addressed through the continuous technological development in the production of new and more suitable fibers and resins.

Fibres @ 0° (UD), 0/90° (fabric) to loading axis, Dry, Room Temperature, Vf = 60% (UD), 50% (fabric)

	Symbol	Units	Std CF Fabric	HMCF Fabric	E glass Fabric	Kevlar Fabric	Std CF UD	HMCF UD	M55** UD	E glass UD	Kevlar UD	Boron UD
Young's Modulus 0°	E1	GPa	70	85	25	30	135	175	300	40	75	200
Young's Modulus 90°	E2	GPa	70	85	25	30	10	8	12	8	6	15
In-plane Shear Modulus	G12	GPa	5	5	4	5	5	5	5	4	2	5
Major Poisson's Ratio	v12		0.10	0.10	0.20	0.20	0.30	0.30	0.30	0.25	0.34	0.23
Ult. Tensile Strength 0°	Xt	MPa	600	350	440	480	1500	1000	1600	1000	1300	1400
Ult. Comp. Strength 0°	Xc	MPa	570	150	425	190	1200	850	1300	600	280	2800
Ult. Tensile Strength 90°	Yt	MPa	600	350	440	480	50	40	50	30	30	90
Ult. Comp. Strength 90°	Yc	MPa	570	150	425	190	250	200	250	110	140	280
Ult. In-plane Shear Stren.	S	MPa	90	35	40	50	70	60	75	40	60	140
Ult. Tensile Strain 0°	ext	%	0.85	0.40	1.75	1.60	1.05	0.55		2.50	1.70	0.70
Ult. Comp. Strain 0°	exc	%	0.80	0.15	1.70	0.60	0.85	0.45		1.50	0.35	1.40
Ult. Tensile Strain 90°	eyt	%	0.85	0.40	1.75	1.60	0.50	0.50		0.35	0.50	0.60
Ult. Comp. Strain 90°	eyc	%	0.80	0.15	1.70	0.60	2.50	2.50		1.35	2.30	1.85
Ult. In-plane shear strain	es	%	1.80	0.70	1.00	1.00	1.40	1.20		1.00	3.00	2.80
Thermal Exp. Co-ef. 0°	Alpha1	Strain/K	2.10	1.10	11.60	7.40	-0.30	-0.30	-0.30	6.00	4.00	18.00
Thermal Exp. Co-ef. 90°	Alpha2	Strain/K	2.10	1.10	11.60	7.40	28.00	25.00	28.00	35.00	40.00	40.00
Moisture Exp. Co-ef 0°	Beta1	Strain/K	0.03	0.03	0.07	0.07	0.01	0.01		0.01	0.04	0.01
Moisture Exp. Co-ef 90°	Beta2	Strain/K	0.03	0.03	0.07	0.07	0.30	0.30		0.30	0.30	0.30
Density		g/cc	1.60	1.60	1.90	1.40	1.60	1.60	1.65	1.90	1.40	2.00

Figure 15: Properties of Several Composite Materials

1.3.6 Mechanics of Composites

Constitutive equations such as the generalized Hooke's law characterize the material and state how it reacts to external loads. Concerning linear elastic behavior, it describes the relationship between stresses and strains, which is expressed through equations (1) and (2).

$$\sigma_{ij} = C_{ijkl}\varepsilon_{kl} \tag{1}$$

$$\varepsilon_{ij} = S_{ijkl}\sigma_{kl} \tag{2}$$

Where :

- i, j, k, l = 1, 2 , 3
- σ, ε : symmetric 2nd order tensors ($\sigma_{ij} = \sigma_{ji}$, $\varepsilon_{ij} = \varepsilon_{ji}$)
- $\varepsilon_{ij} = \frac{1}{2}(u_{i,j} + u_{j,i})$, u : displacement vector
- C_{ijkl} : 4th order stiffness tensor (3^4 independent components)
- S_{ijkl} : 4th order compliance tensor (3^4 independent components)

Due to the symmetry of the stress and strain tensors, it is proved that the 4th order elastic tensors are also symmetric and can be characterized by 21 independent constants, while the above relationships can be expressed via a matrix form.

$$\sigma_i = C_{ij}\varepsilon_j \tag{3}$$

$$\varepsilon_i = S_{ij}\sigma_j \tag{4}$$

Where :

- i, j = 1, … ,6
- $C_{ij} = C_{ji}$, $S_{ij} = S_{ji}$

According to the Voigt notation, the physical indexes can be related to those of the matrix form as :

$$\begin{Bmatrix}\sigma_1\\ \sigma_2\\ \sigma_3\\ \sigma_4\\ \sigma_5\\ \sigma_6\end{Bmatrix} = \begin{Bmatrix}\sigma_{11}\\ \sigma_{22}\\ \sigma_{33}\\ \sigma_{23}\\ \sigma_{13}\\ \sigma_{12}\end{Bmatrix} \quad \begin{Bmatrix}\varepsilon_1\\ \varepsilon_2\\ \varepsilon_3\\ \varepsilon_4\\ \varepsilon_5\\ \varepsilon_6\end{Bmatrix} = \begin{Bmatrix}\varepsilon_{11}\\ \varepsilon_{22}\\ \varepsilon_{33}\\ 2\varepsilon_{23}\\ 2\varepsilon_{13}\\ 2\varepsilon_{12}\end{Bmatrix} \tag{5}$$

It is important to note that shear strains are expressed through engineering constants, which are twice the corresponding tensor coefficients ($\varepsilon_4=\gamma_{23}=2\varepsilon_{23}$). Accordingly, for a linear elastic anisotropic material (triclinic system), the Hooke's law takes the form :

$$\begin{Bmatrix}\sigma_1\\ \sigma_2\\ \sigma_3\\ \sigma_4\\ \sigma_5\\ \sigma_6\end{Bmatrix} = \begin{Bmatrix}C_{11}\ C_{12}\ C_{13}\ C_{14}\ C_{15}\ C_{16}\\ C_{12}\ C_{22}\ C_{23}\ C_{24}\ C_{25}\ C_{26}\\ C_{13}\ C_{23}\ C_{33}\ C_{34}\ C_{35}\ C_{36}\\ C_{14}\ C_{24}\ C_{34}\ C_{44}\ C_{45}\ C_{46}\\ C_{15}\ C_{25}\ C_{35}\ C_{45}\ C_{55}\ C_{56}\\ C_{16}\ C_{26}\ C_{36}\ C_{46}\ C_{56}\ C_{66}\end{Bmatrix} \begin{Bmatrix}\varepsilon_1\\ \varepsilon_2\\ \varepsilon_3\\ \varepsilon_4\\ \varepsilon_5\\ \varepsilon_6\end{Bmatrix} \tag{6}$$

$$\begin{Bmatrix}\varepsilon_1\\ \varepsilon_2\\ \varepsilon_3\\ \varepsilon_4\\ \varepsilon_5\\ \varepsilon_6\end{Bmatrix} = \begin{Bmatrix}S_{11}\ S_{12}\ S_{13}\ S_{14}\ S_{15}\ S_{16}\\ S_{12}\ S_{22}\ S_{23}\ S_{24}\ S_{25}\ S_{26}\\ S_{13}\ S_{23}\ S_{33}\ S_{34}\ S_{35}\ S_{36}\\ S_{14}\ S_{24}\ S_{34}\ S_{44}\ S_{45}\ S_{46}\\ S_{15}\ S_{25}\ S_{35}\ S_{45}\ S_{55}\ S_{56}\\ S_{16}\ S_{26}\ S_{36}\ S_{46}\ S_{56}\ S_{66}\end{Bmatrix} \begin{Bmatrix}\sigma_1\\ \sigma_2\\ \sigma_3\\ \sigma_4\\ \sigma_5\\ \sigma_6\end{Bmatrix} \tag{7}$$

The stiffness (or the compliance) coefficients C_{ij} (or S_{ij}) are directly related to the material properties E_i (Young's modulus in the x_i – direction), G_{ij} (Shear modulus in the x_ix_j – plane) and v_{ij} (Poisson's ratio). It is worth noting that anisotropic materials do not present any symmetry in their structure thus having 21 independent coefficients. However, there are materials that are characterized by one or more plates of symmetry, which can reduce the number of independent coefficients. A well-known example are orthotropic materials, such as woven fabrics, which have three mutually orthogonal planes of symmetry that lead to the reduction of the independent elastic coefficients to 9. For an on-axis orthotropic material, the material coordinate system agrees with the structure's symmetry and the Hooke's law is given by the equation (8).

$$\begin{Bmatrix}\sigma_1\\ \sigma_2\\ \sigma_3\\ \sigma_4\\ \sigma_5\\ \sigma_6\end{Bmatrix} = \begin{Bmatrix} C_{11} & C_{12} & C_{13} & 0 & 0 & 0\\ C_{12} & C_{22} & C_{23} & 0 & 0 & 0\\ C_{13} & C_{23} & C_{33} & 0 & 0 & 0\\ 0 & 0 & 0 & C_{44} & 0 & 0\\ 0 & 0 & 0 & 0 & C_{55} & 0\\ 0 & 0 & 0 & 0 & 0 & C_{66}\end{Bmatrix} \begin{Bmatrix}\varepsilon_1\\ \varepsilon_2\\ \varepsilon_3\\ \varepsilon_4\\ \varepsilon_5\\ \varepsilon_6\end{Bmatrix} \quad (8)$$

According to (8) it is obvious that an on axis orthotropic material does not include any coupling between normal stresses and shear strains, thus normal strains cause only normal stresses and shear strains cause only shear stresses. Nonetheless, there are many cases where the material system does not agree with the main (global) coordinate system of the structure. Hence, it is essential to establish a transformation relation between those systems. Assuming that there will be an in-plane rotation of the on axis orthotropic material system by a «θ» angle, then the relation between the stresses of the two systems, will be expressed as :

$$\sigma^{(1)} = T_\sigma \sigma^{(x)} \quad (9)$$

Where :

- $\sigma^{(1)}$: Stresses referred to the material system (rotated by an angle θ)
- $\sigma^{(x)}$: Stresses referred to the global coordinate system
- T_σ : Transformation matrix which for an in plane rotation of an orthotropic material is

$$T_\sigma = \begin{bmatrix} cos^2\theta & sin^2\theta & 0 & 0 & 0 & 2cos\theta sin\theta\\ sin^2\theta & cos^2\theta & 0 & 0 & 0 & -2cos\theta sin\theta\\ 0 & 0 & 1 & 0 & 0 & 0\\ 0 & 0 & 0 & cos\theta & -sin\theta & 0\\ 0 & 0 & 0 & sin\theta & cos\theta & 0\\ -cos\theta sin\theta & cos\theta sin\theta & 0 & 0 & 0 & cos^2\theta - sin^2\theta\end{bmatrix} \quad (10)$$

Following the same philosophy, the relation between the strains of the 2 coordinate systems is expressed through (11) :

$$\varepsilon^{(1)} = T_\varepsilon \varepsilon^{(x)} \tag{11}$$

$$T_\varepsilon = \begin{bmatrix} cos^2\theta & sin^2\theta & 0 & 0 & 0 & cos\theta sin\theta \\ sin^2\theta & cos^2\theta & 0 & 0 & 0 & -cos\theta sin\theta \\ 0 & 0 & 1 & 0 & 0 & 0 \\ 0 & 0 & 0 & cos\theta & -sin\theta & 0 \\ 0 & 0 & 0 & sin\theta & cos\theta & 0 \\ -2cos\theta sin\theta & 2cos\theta sin\theta & 0 & 0 & 0 & cos^2\theta - sin^2\theta \end{bmatrix} \tag{12}$$

Hence stiffness and compliance matrix that are expressed on the global (physical) system are given by (13) and (14) :

$$C^{(x)} = T_\sigma^{-1} C^{(1)} T_\varepsilon \tag{13}$$

$$S^{(x)} = T_\varepsilon^{-1} S^{(1)} T_\sigma \tag{14}$$

Laminated composite materials usually have their planar dimensions much larger than their transverse one, hence they can be treated as plate elements which behave according to plate theories. Classical laminated plate theory (CLPT) is an extension of the Kirchhoff plate theory which generally applies to thin-walled structures. The Kirchhoff assumptions imply that the transverse displacement along z-axis is independent of the plate's thickness, following that the transverse normal strain ε_z and the shear strains ε_{xz} and ε_{yz} are zero. Moreover, the plate is considered to be in a state of plane stress ($\sigma_3=\sigma_4=\sigma_5=0$) which means that every ply of the laminate will have a mechanical behavior described by equation (15).

$$\begin{Bmatrix} \sigma_1 \\ \sigma_2 \\ \sigma_6 \end{Bmatrix} = \begin{bmatrix} Q_{11} & Q_{12} & 0 \\ Q_{12} & Q_{22} & 0 \\ 0 & 0 & Q_{66} \end{bmatrix} \begin{Bmatrix} \varepsilon_1 \\ \varepsilon_2 \\ \varepsilon_6 \end{Bmatrix} \tag{15}$$

- Q : reduced stiffness matrix
- $Q_{11} = E_1/(1 - v_{12}v_{21})$
- $Q_{22} = E_2/(1 - v_{12}v_{21})$
- $Q_{12} = v_{12}E_2/(1 - v_{12}v_{21}) = v_{21}E_1/(1 - v_{12}v_{21})$
- $Q_{66} = G_{12}$

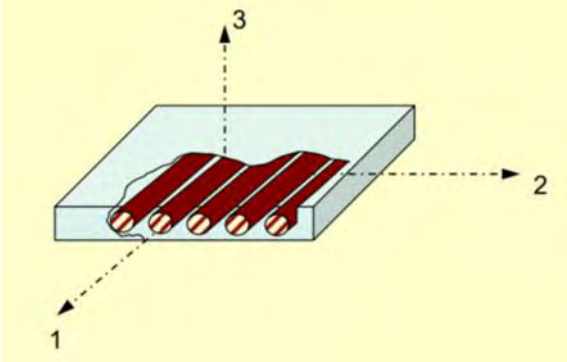


Figure 16: Representation of an On-Axis Orthotropic Ply [11]

It is important to mention that the above equation refers to the behavior of an on-axis orthotropic ply, hence through a proper simplification of the equations (10) and (12) given the state of plane stress, the behavior of an off-axis orthotropic ply can be extracted.

$$Q^{(x)} = T_{\sigma}^{-1} Q^{(1)} T_{\varepsilon} \tag{16}$$

$$\begin{Bmatrix} \sigma_x \\ \sigma_y \\ \sigma_s \end{Bmatrix} = \begin{bmatrix} Q_{xx} & Q_{xy} & Q_{xs} \\ Q_{xy} & Q_{yy} & Q_{ys} \\ Q_{xs} & Q_{ys} & Q_{ss} \end{bmatrix} \begin{Bmatrix} \varepsilon_x \\ \varepsilon_y \\ \varepsilon_s \end{Bmatrix} \tag{17}$$

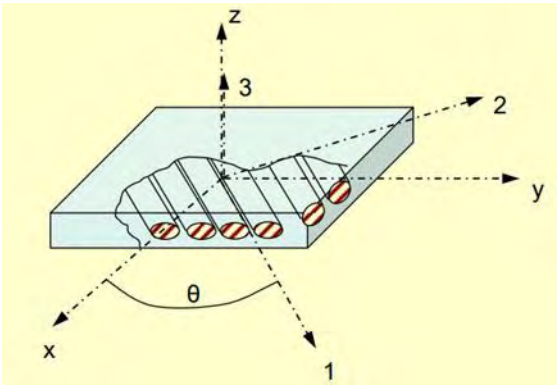


Figure 17: Representation of an Off-Axis Orthotropic Ply [11]

According to CLPT [12] the equations that relate the in-plane force resultants (N_x ,N_y ,N_s) and the moment resultants (M_x ,M_y ,M_s) with the strains of the entire laminate are respectively given by (18) and (19).

$$\begin{Bmatrix} N_x \\ N_y \\ N_s \end{Bmatrix} = \begin{bmatrix} A_{xx} & A_{xy} & A_{xs} \\ A_{xy} & A_{yy} & A_{ys} \\ A_{xs} & A_{ys} & A_{ss} \end{bmatrix} \begin{Bmatrix} \varepsilon_x^o \\ \varepsilon_y^o \\ \varepsilon_s^o \end{Bmatrix} + \begin{bmatrix} B_{xx} & B_{xy} & B_{xs} \\ B_{xy} & B_{yy} & B_{ys} \\ B_{xs} & B_{ys} & B_{ss} \end{bmatrix} \begin{Bmatrix} k_x \\ k_y \\ k_s \end{Bmatrix} \tag{18}$$

$$\begin{Bmatrix} M_x \\ M_y \\ M_s \end{Bmatrix} = \begin{bmatrix} B_{xx} & B_{xy} & B_{xs} \\ B_{xy} & B_{yy} & B_{ys} \\ B_{xs} & B_{ys} & B_{ss} \end{bmatrix} \begin{Bmatrix} \varepsilon_x^o \\ \varepsilon_y^o \\ \varepsilon_s^o \end{Bmatrix} + \begin{bmatrix} D_{xx} & D_{xy} & D_{xs} \\ D_{xy} & D_{yy} & D_{ys} \\ D_{xs} & D_{ys} & D_{ss} \end{bmatrix} \begin{Bmatrix} k_x \\ k_y \\ k_s \end{Bmatrix} \tag{19}$$

More specifically $\left(\varepsilon_x^o , \varepsilon_y^o , \varepsilon_s^o\right)$ are the membrane strains and $\left(k_x , k_y , k_s\right)$ are the bending strains of the entire laminate plate. As for the A, B and D matrixes, they are expressed in terms of the k^{th} ply reduced stiffness matrix Q^k, as shown below.

$$A_{ij} = \sum_{k=1}^{n} Q_{ij}^{(k)} (z_k - z_{k-1})$$

$$B_{ij} = \frac{1}{2} \sum_{k=1}^{n} Q_{ij}^{(k)} \left(z_k^2 - z_{k-1}^2\right) \tag{20}$$

$$D_{ij} = \frac{1}{3} \sum_{k=1}^{n} Q_{ij}^{(k)} \left(z_k^3 - z_{k-1}^3\right)$$

The (i , j) indexes correspond to the (x , y , s) ones while the z_k variable expresses the distance of the top surface of the k^{th} ply from the geometric center (midplane) of the entire laminate. A more in-depth examination revealed that the ABD matrix essential defines the elastic properties of the entire laminate. The matrix A, also known as extensional stiffness matrix, relates the in-plane force resultants with the membrane strains, while the D matrix associates the moment resultants with the bending strains and is usually referred as flexural stiffness matrix. As for the matrix B, it connects the forces with the bending strains and the moments with the membrane strains, thus it is often mentioned as coupling stiffness matrix. In closing, it is worth mentioning that A, B and D matrixes are symmetric, due to the symmetry of the reduced stiffness matrix Q^k, meaning that $A_{ij}=A_{ji}$, $B_{ij}=B_{ji}$ and $D_{ij}=D_{ji}$

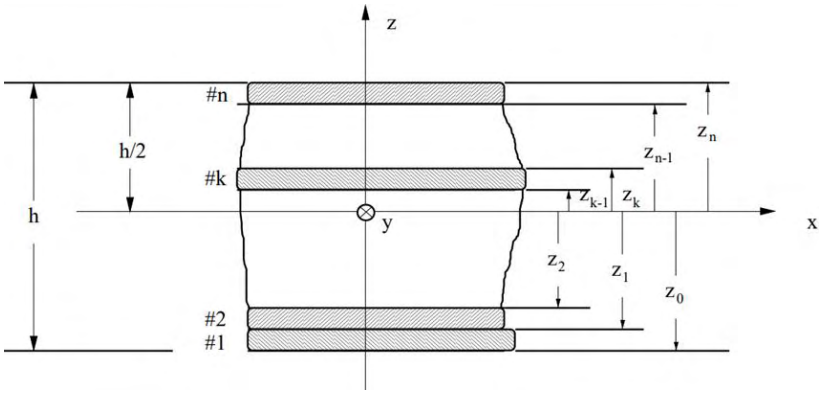


Figure 18: Transverse Cross Section of a Laminate with n- Plies [11]

When designing a laminate, it is important to consider the stacking sequence of plies and to be aware of the symmetry and the balance of the stack. A laminate in which plies locate symmetrically with respect to the midplane and have exactly the same orientation, thickness, and material, is considered symmetric. Mathematically, this type of stacking is characterized by a matrix B with zero elements B_{ij} and helps not only to eliminate any tendency to bend or warp, but also to avoid thermal twisting of parts as they cool down after curing . Additionally, when a laminate has an equal number of $+45^o$ and -45^o plies, is considered balanced [13] and reduces shear coupling [14]. Based on the previous ones, a symmetric laminate with no stretching-shearing coupling ($A_{xs}=A_{ys}=0$) is called specially orthotropic.

One of the most widely used stacking sequence is the quasi-isotropic laminate. This type of lamination provides in plane isotropic behavior, meaning that the strength and stiffness are equal in all directions within the plane of the part. In a typical quasi-isotropic laminate, the stacking sequence must be balanced and symmetrical, while it should contain layers with identical materials and thicknesses so that $A_{xx} = A_{yy}$, $A_{xs} = A_{ys} = 0$ and $A_{ss} = ½(A_{xx} – A_{yy})$ which correspond to the extensional stiffness matrix of a common isotropic material. The main difference is that quasi-isotropic materials cannot eliminate the D_{xs} and D_{ys} elements of the flexural stiffness matrix, in contrast to isotropic ones where $D_{xs} = D_{ys} = 0$. Generally, quasi-isotropic laminates contain ν (>3) plies with fibers arranged by π/ν rad in the (-π/2 , π/2] range. In addition to working together to provide quasi-isotropic properties, the fibers at different directions also provide specific strengths [15] :

- **0º layers** : Provide axial strength and stiffness that is ideal for structures that must resist axial loads.
- **+/- 45º layers** : Provide shear strength and stiffness, making them a necessary choice for applications with high shear loads.
- **90º layers** : Provide transverse strength and stiffness that is ideal for creating a consolidating layer that keeps everything together.

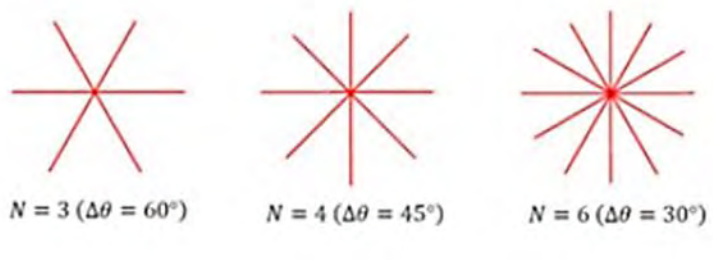


Figure 19: Fiber Orientations in π/3 , π/4 and π/6 Quasi-Isotropic Laminates [16]

It is a fact that quasi-isotropic laminates create stiff materials with appropriate strength in all directions, making them a top choice when unknown or multiple direction loads are applied. A unique advantage of quasi-isotropic materials is that they are ideal for composite plates with holes or slots, as due to their morphology they encircle the discontinuity , thus providing sufficient transport of loads through the fibers without greatly straining the resin. Furthermore, they can directly replace metal components by greatly reducing the total weight and offering similar or even better elastic properties. However, it should be taken into consideration that in most cases, the design of a composite structure must not be based on the automatic selection of quasi-isotropic laminates, as it may not be the best possible solution. On the contrary, every designer should find the most suitable stacking sequence depending on the requirements of the design problem by trying to take the maximum advantage of each layer's properties. For example, a quasi-isotropic layup [0/45/90/-45]S is able to support adequately axial, transverse and shear loading. However, it is up to 40% as stiff as a single 0^0 layer, made of the same fiber-resin type, in the axial direction and about 60% as stiff as a +/- 45^0 layup such us [45/-45/45/-45]S in shear.

1.3.7 The UPSAT Project

The University of Patras Satellite (UPSAT) was a project that started by University of Patras in collaboration with many other departments and carried out during the period from 2007 to 2017. UPSAT is a 2U CubeSat type satellite, manufactured in Greece and was a part of the QB50 mission, coordinated by the von Karman Institute at Belgium. In April 2017, the satellite was launched in space on board the Cygnus CRS OA-7 mission to International Space Station (ISS), from which it was deployed successfully on the 17th of May 2017. The main goals of UPSAT project are listed below:

- Integration of Composite Materials into the CubeSat main structural frame.
- Minimize the usage of COTS components to the absolute minimum by designing all the subsystems from scratch in an open-source software.
- Keep the mass below the maximum allowable limit defined by the mission (2.3 kilos).
- Integration of a camera with scope of taking the first photo of Greece ever taken by a student's satellite.

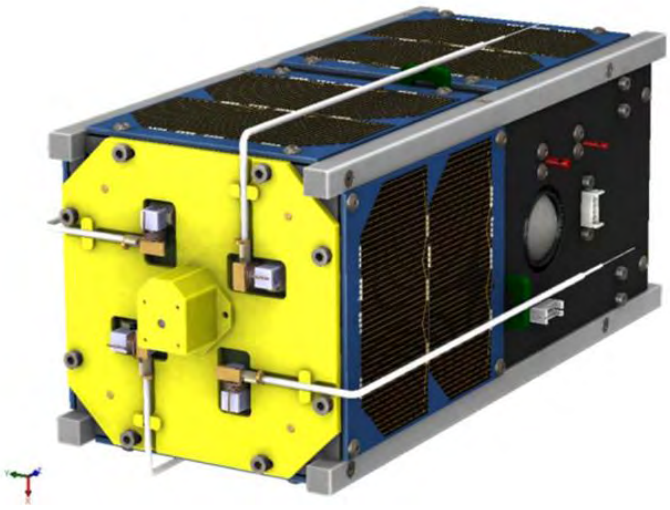


Figure 20: Fully Assembled View of UPSAT

The design philosophy aimed at the creation of a “hybrid” structure consisting of both Composite Materials and Aluminum Alloy, based however at the commercially available CubeSat structures. Moreover, the chassis consisted of four rails and four crossmembers, all of them made of Aluminum (7075-T6 Alloy), surrounded by four CFRP faces (panels). It is worth noting that the idea of a full composite structure was abandoned due to accessibility and compatibility with the internal of the POD issues. The material of every CFRP-lamina was a Cyanate-Ester/Carbon unidirectional pre-preg [HTM143/M55J (6K)], while the final lay-up consisted of 8 layers with total thickness of 1mm. Concerning the lamination, previous works [17] had revealed that the lay-up of [0/45/90/-45]S gives the best combination of mass and stiffness for such applications and thus it was used. The chosen lay-up offered quasi-isotropic properties and on top of that, its small thickness created extra available area for any exceeded components, such as solar panels. Regarding the local coordinate system for the CFRP faces, the 0^o fiber direction was considered along the length (Z-Axis) of the side faces (±X and ±Y) while for +Z CFRP face (base), the 0^0 direction is along the Y-Axis (Global Reference System).

As for the mounting of the CFRP sides on the Aluminum frame, Stainless Steel-Hex Socket Button Head Bolts were considered. On the other hand, all the bolts that used for connecting the rails to the four aluminum crossmembers (decks) were Countersunk type so that the bolt heads did not exceed from the rail surface. Lastly, all PCBs (Printed Circuit Boards) were considered stacked along the Z-direction using both COTS and brass spacers (Φ3), which connected them both with each other and with the decks (square aluminum parts).

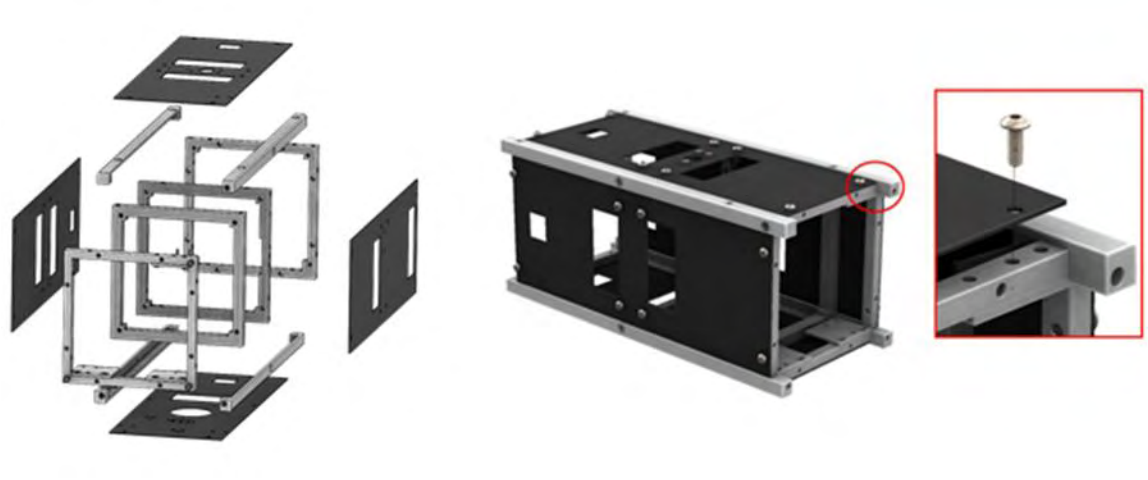


Figure 21: UPSAT completed Structural System

The detailed FE Model was created in the MSC PATRAN preprocessor, and all the necessary results were extracted through the NASTRAN solver. For all the aluminum parts (rails and decks), solid 3D elements were used, while for the CFRP side faces and the PCBS, shell 2D elements (QUAD4) were considered due to their low thickness to length and thickness to width ratio (thin-walled components). All the bolts and the spacers were modeled using 1-D beam elements and were connected to the other parts through RBE2 Interpolation Elements, that offer Multi Point Constraints (MPCs), which allow the modeling of the motion of one or more grid points as a function of the motion of the other parts.

Concerning the boundary conditions, the outer surfaces of the rails, that connect the entire CubeSat structure with the POD, restrained at all 6 DOFS (Rx,Ry,Rz,Tx,Ty,Tz==0). Additionally, all the loading scenarios according to QB50 [18] requirements were considered, and the prescribed inputs were applied at all three major axis of the CubeSat. More specifically, for the Quasi-Static analysis, 13g Inertial load was taken into account, whereas for the modal analysis, every natural frequency should be above the natural frequency of the POD (f= 90 Hz), in order to avoid a possible resonance.

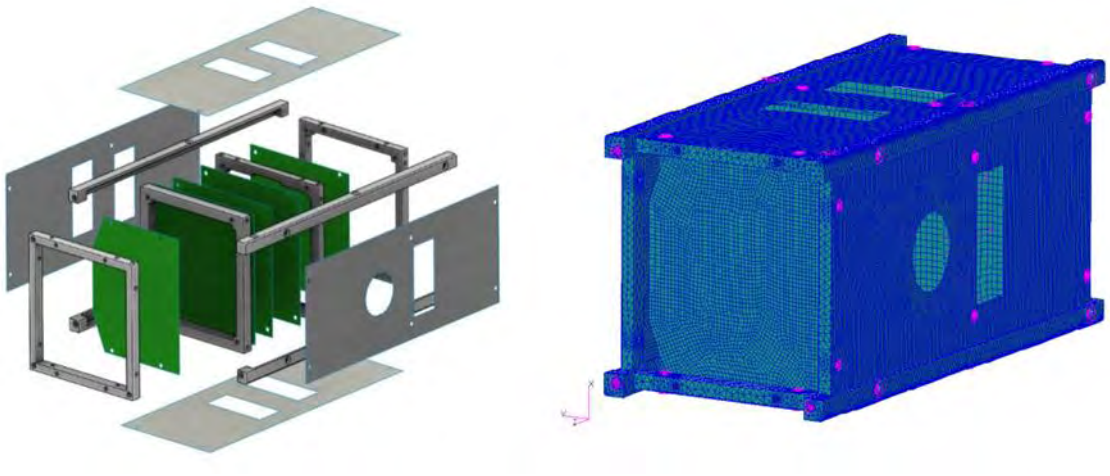


Figure 22: Simplified Model with Solid and Surface Parts (left), Finite Element Model (right)

In conclusion, UPSAT [19] was the first open-source satellite ever launched and the first satellite, designed, built, and tested entirely in Greece. The impact of this CubeSat was massive and had straight effect on the University of Patras community, leading many students not only to express their interest but also to apply their skills in the space engineering area. As Andreas Ampatzoglou, who took part in UPSAT project, mentioned in his PhD dissertation [20]: “The next route for micro-satellite applications is the development of a complete Six-Unit (6U) platform”. Being highly motivated by this phrase and the entire UPSAT project, in combination with my passion for space, decided that the present thesis will deal with both the design and the analysis of 6U CubeSat, using composite materials.

2.0 COMPUTER AIDED DESIGN (CAD) PHASE

On this chapter, there will be an analytic report on the Computer Aided Design (CAD) followed for the final 6U CubeSat structure design. Firstly, some COTS and custom-made 6U structures, that became source of inspiration for our final design, will be mentioned. In the next place, there will be a reference to the design specifications and requirements that the present 6U meets. Undoubtedly, components cannot be designed independently from each other in a highly integrated miniaturized satellite platform. Therefore, each component will be described after all the design iterations were completed. Lastly, the final assembly that includes all the connected components, will be presented, and discussed. It is important to mention that the effectiveness of the entire structure will be confirmed by a Finite Element Analysis, that follows on the next chapter.

2.1 6U CubeSat Structures

Before starting the development of the current's thesis 6U, several structures that have already been built and are available for purchase were considered. Some of the most popular companies that have structure kits available are Pumpkin, ISIS and Gomspace. They have quite similar design approaches and all of them focus on the discretization of the entire chassis into such a way as to create six separate inner spaces, every one of which corresponds to the 1U dimensions (100 x 100 x 100 mm3). It is worth noting, that most of the structures presented in the following table, contain the appropriate crossmembers, on which the placement of the electronic boards will be taken place. Especially, 6Us both by spacemind and ISIS, have a unique crossmembers setting, allowing batteries and other electronics to be placed not only vertically

but also horizontally. Additionally, some of the most innovative ones, are that of Clyde Space, known as ZAPHOD 6U, which has a pioneering panel design approach and also that of Cervos, which consists of six rails. It is a fact that, the majority of them uses rails as the connector between CubeSat and POD, with the exception of the pumpkin's 6U than contains tabs. Obviously, all of them meet the appropriate design specifications.

Examples of typical 6Us chassis

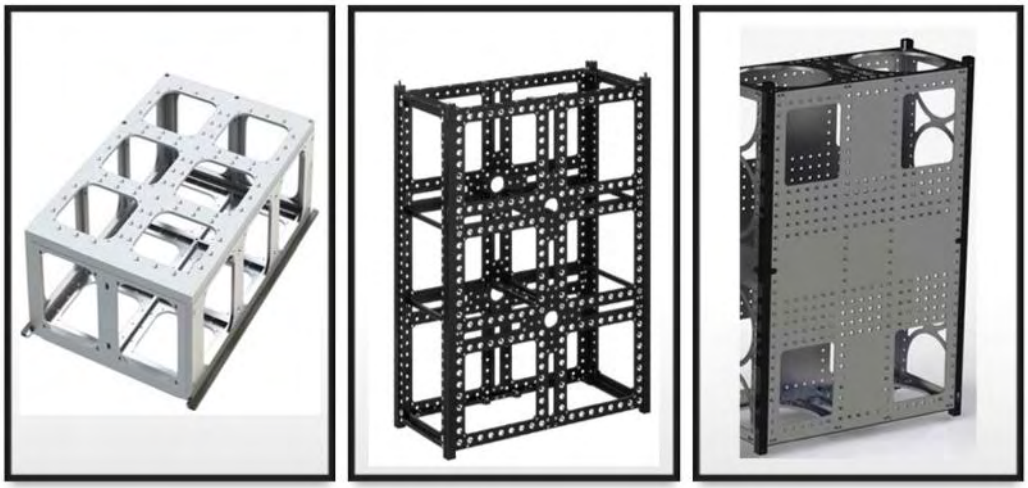


Figure 23: Pumpkin [21] (left), Nanoavionics [22] (middle), Zaphod [23](right)



Figure 24: EnduroSat [24] (left), Cervos [25] (middle), SM06 by spacemind [26] (right)

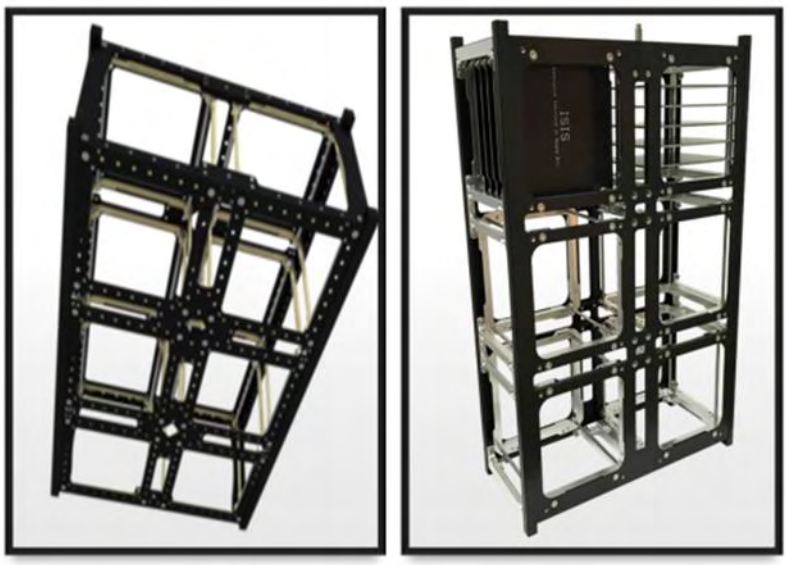


Figure 25: Gomspace [27] (left), ISIS [10] (right)

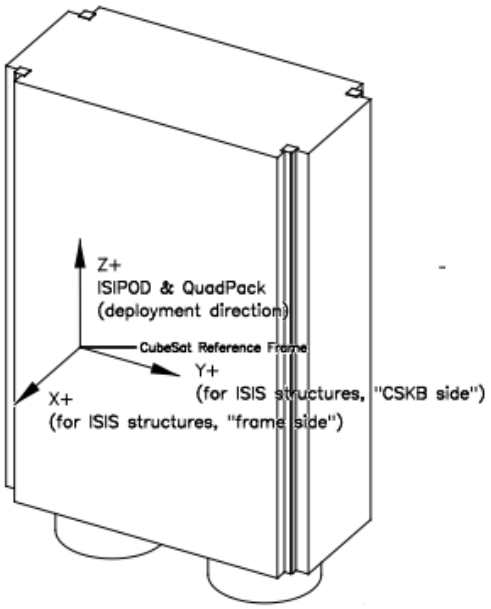
Table 3: Examples of typical 6Us chassis

2.2 Design Specifications and Operational Requirements For a 6U-XL CubeSat

As referred on a previous chapter, every CubeSat must meet strict specifications, according to its size in order to be connected with the POD. The satellite of the current thesis is a 6U-XL that corresponds to the Design Specifications provided by ISIS company. The POD that ISIS produces for this type of CubeSats is known as QuadPack Type 2-XL, which allows more volume at all its lateral sides. Although, most of the general specifications discussed before are still applied, there should be considered some extra notes, that refer to the QuadPack dispenser[2].

[2] For more information see Appendix

- CubeSat Feet's cross section must be 8.5 x 8.5 mm^2 with edges rounded to a radius of 1 mm.
- The Centre of Gravity shall be located within a sphere with radius of 20 mm from its geometric center.
- The mass of a 6U-XL can be reached up to 12.00 kg.
- The maximum height (Z-direction) for a 6U-XL is 366 mm whereas the other dimensions should not be above 246.3 mm (Y-direction) and 120 mm (X-direction).
- Faces both on X and Y direction should not exceed more than 10 mm distance from the rails.
- QuadPack allows additional volume, known as "tuna cans" on the bottom (-Z direction) of the CubeSat.



In addition to these specifications, there must also be made a reference to the purpose of the CubeSat's mission so as to determine the appropriate operational requirements. More specifically, the goal of the current 6U-XL is to carry a robotic arm, which will be deployed in space. This mechanism will fill a space of 105 x 120 x 200 mm^3, however due to confidential reasons, it cannot be included in CAD. For that reason, only the occupied location, which directly affects the overall CubeSat design, will be presented. It is important to note that the robotic arm requires the creation of a deployable panel, that will allow its development, however an extensive reference will be made in a next subsection.

2.3 6U-XL Structure Components

The main design philosophy of the present structure is to promote the use of composite materials on the chassis wall[3] of the CubeSat. In general, the current satellite follows the ISIS specifications referred to 6U-XLs, with the only exception being that it does not include any tuna cans. More accurately it consists of :

- **6 rails** made of Al 7075-T6, of which the 4 function as connecting links between the satellite and the POD, whereas the other 2 hold the decks together, offering the appropriate mechanical stability to the whole structure.
- **8 decks** made of Al 7075-T6, that mainly increase the stiffness of the structure and also carry batteries and other electronics.
- **6 + 1 panels**, all made of CFRP, where 2 of them cover the side faces, the other 2 form the bottom and top base and the remaining set up the main “frame” sides. It is worth noting, that one of the main panels, consists of 2 sub-panels, from which one is deployable, in order to allow the movement of the robotic arm.
- **16 aluminum threaded rods**, which connect the decks together and carry all the brass standoffs that will be used to mount the electronics.
- **A deployment mechanism**, that will deploy the sub-panel mentioned before.
- **Bolts, nuts, and standoffs**, that make the necessary connections between the components for the synthesis of the final assembly.

[3] All panels and bases included.

The initial design approach based on the combination of six “imaginary” 1Us than directly dealing with an entire 6U platform. This treatment led us to divide the interior of the satellite into two main regions. The first one takes up a little less than half of the total available space and has the ability to contain a volume corresponding to almost three 1Us. Each sub-area of the first region consists of two decks and four rods, thus forming an “imaginary” 1U, that can be both assembled and placed independently of the rest inside the CubeSat. This region is responsible for containing the batteries and all the electronic systems that are necessary for the proper operation of the satellite. The second region includes the remaining space of the CubeSat and as it is obvious, it will contain the appropriate volume for the payload mounting. Besides that, there is also some free space, at the top of the payload, for creating another “1U system”, which however is slightly bigger than of those mentioned on the first region.

As a general rule, it is proposed that the structure should be as symmetrical as possible. During the design process, many attempts, such as the creation of equal panel thicknesses, symmetrically mounted bolts, and uniformly distributed decks, were made in order to tend to create a balanced CubeSat. However, the dimensions of the volume occupied by the payload (robotic arm) did not allow a design of a fully symmetrical structure.

It is important to point out that many components share identical connections, with the most representative example being that of the deck – panel – rail connection. In this case, the bolt starts from a deck, passes through the panel, and ends in a blind hole on the rail. This connection method reduces the total number of bolts, which implies directly with total mass reduction and making the final assembly much easier.

All the CAD parts were designed in CATIA and after many design iterations, the ultimate structure of the CubeSat emerged. A first view of the final assembly can be seen on Figure 26.

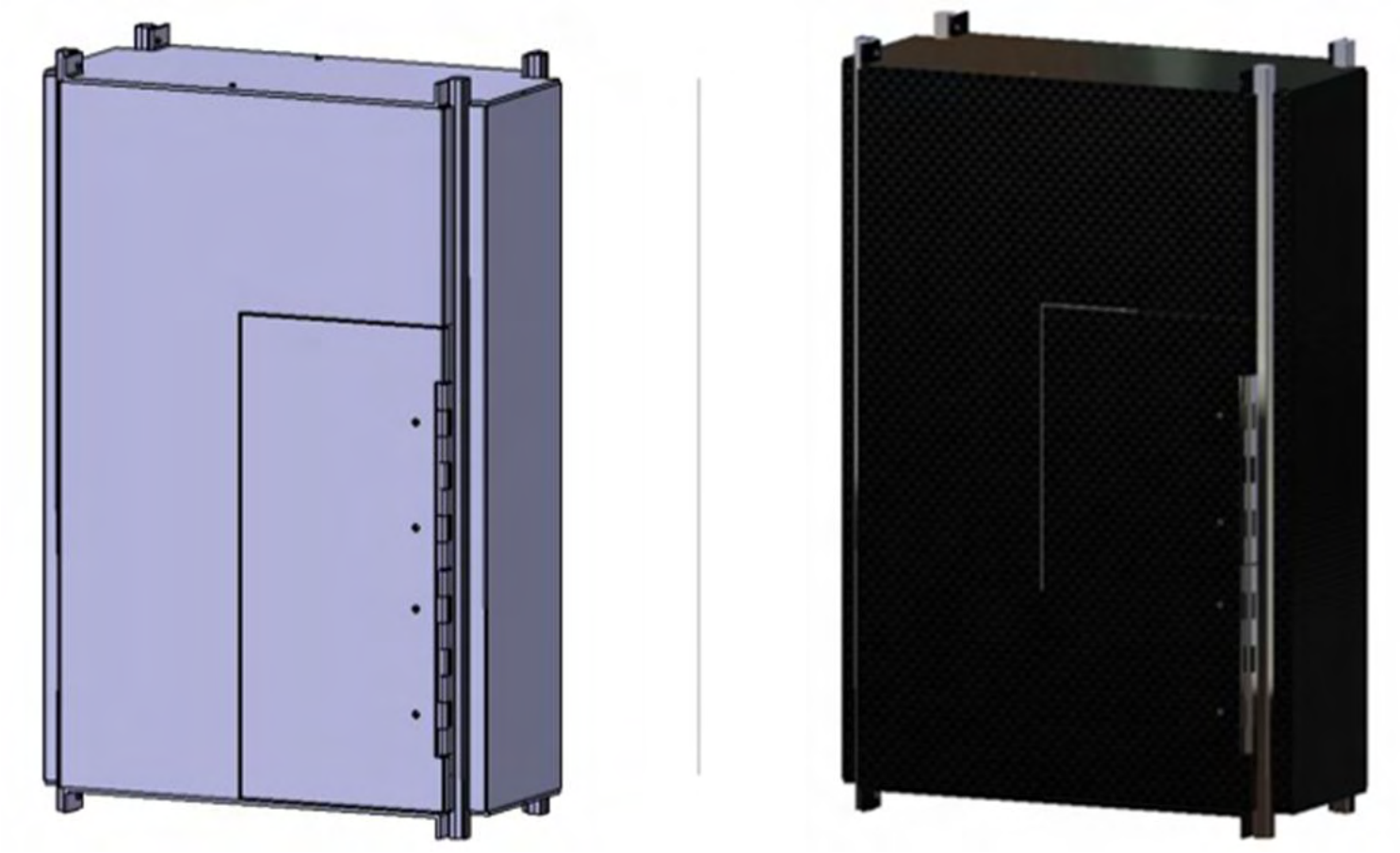


Figure 26: Fully Assembled View of the Present 6U-XL (left: Shading with Edges, right: Shading with Materials)

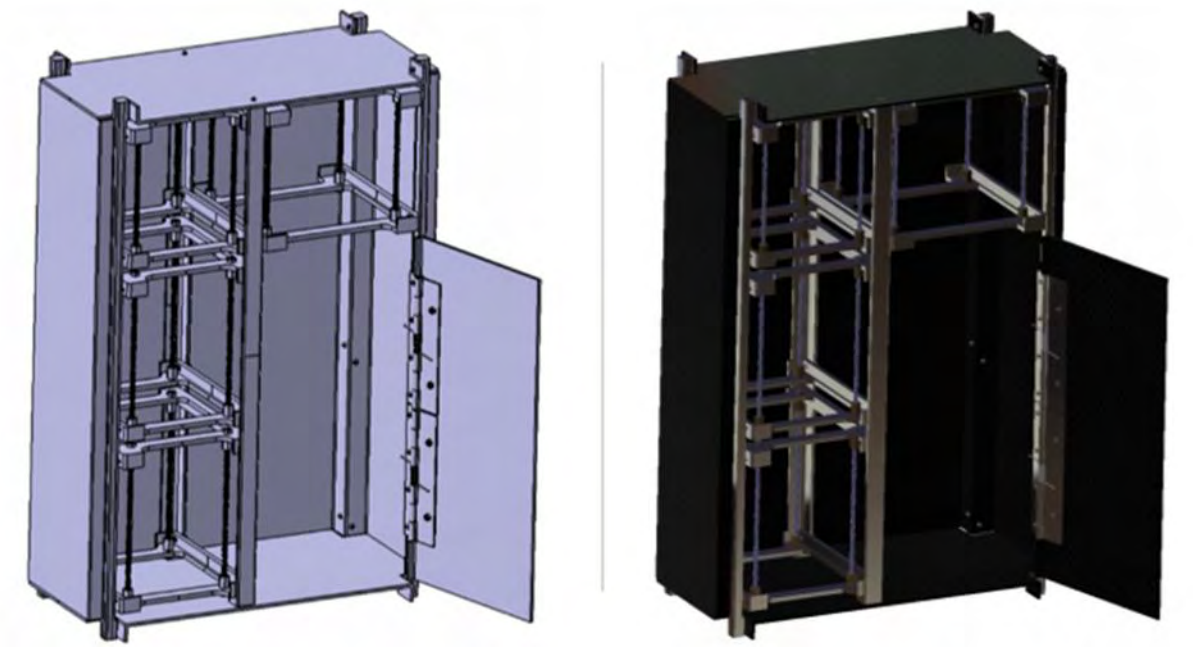


Figure 27: Fully Assembled View of the CubeSat's Interior

The total mass of the CubeSat is **1.727 kg**, without containing the electronic boards or any other secondary component and the transportable cargo. The location of the Center of Gravity is presented in Figure 28 and also captured in 3D-space in Figure 29.

Result
Calculation mode : Exact
Type : Volume

Characteristics		Center Of Gravity (G)	
Volume	8,536e-004m3	Gx	-46,841mm
Area	0,853m2	Gy	114,536mm
Mass	1,727kg	Gz	178,306mm
Density	Not uniform		

Inertia / G | Inertia / O | Inertia / P | Inertia / Axis | Inertia / Axis System

Inertia Matrix / G

IoxG	0,034kgxm2	IoyG	0,026kgxm2	IozG	0,017kgxm2
IxyG	-7,291e-006kgxm2	IxzG	2,981e-004kgxm2	IyzG	-3,639e-004kgxm2

Principal Moments / G

M1	0,017kgxm2	M2	0,026kgxm2	M3	0,034kgxm2

Figure 28: Geometrical Characteristics of the CAD's model

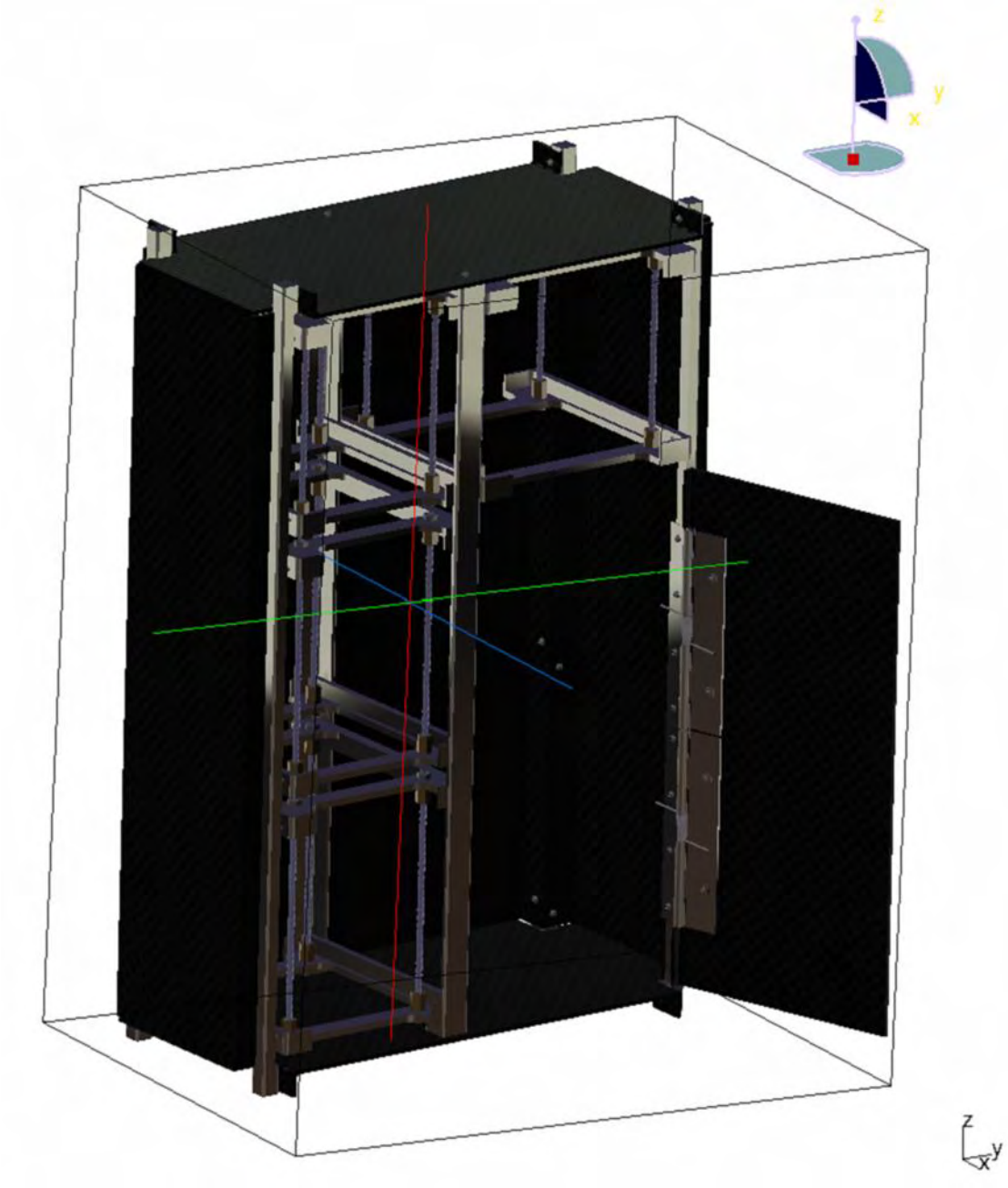


Figure 29: Center of Gravity (CAD Model – Internal View)

2.3.1 Rails

Most of the 6U structures presented on Table 3, make use of rails as the connector between the deployable system and the CubeSat. Because of that and considering the ease of assembly which they offer, we ended up integrating them also in the present 6U-XL. It is a fact that they constitute the most critical components of the entire structure, as they take part in almost all the inner connections. Besides the four main rails that will be connected to the POD, there are also two intermediate ones that hold decks together, offering thus the appropriate stability in our satellite.

It is worth noting that the existence of these two intermediate rails, give us the opportunity to integrate composite panels in the chassis. Moreover, in case they didn't exist, there should be a proper panel formation, such as an intermediate flange, that would carry the bolts, and the transferred loads as well, in order to hold the decks in place. Apart from the difficulty of manufacturing a laminate that could fit in that shape, it is also considered dangerous to carry loads, that will come from the bolt's connections, on such a flange. Thus, we introduced the intermediate rails, that are made also of Al 7075-T6 and have suitable grooves to achieve larger contact surfaces with every deck. Their feets have a cross section of 13 x 13 mm2, which is slightly larger than that of the main rails, however they are not intended to be attached to the POD, so there is not any particular restriction coming from the specifications. Their height corresponds to the distance between the top and the bottom base of the CubeSat, offering the opportunity to connect them directly to every foot of the two intermediate rails, through four suitable M2 bolts. These connections make the movement of every base depended on the interior components, thus increasing the stiffness of the total structure, and preventing the bases, especially when the payload has been inserted, from obtaining large displacements.

Regarding the four main rails, they have a height of 366mm and their feets have a cross section of 8.5 x 8.5 mm^2, aiming to meet the design specifications discussed before. It is remarkable, that these rails have been properly designed so that they can carry the panel's flanges without affecting the advised dimensions. It is also noteworthy that the two left[4] main rails and also the intermediate ones are symmetrical but not identical, so they need to be treated as different components in both the manufacturing and the assembly process. As for the right main rail which locates on -X face of the CubeSat, it has two threaded holes less than the two mentioned before, in the connection area of the main panel due to the lack of decks. Lastly, the right main rail on +X face is unique and is designed with the appropriate configurations to carry the deployable mechanism, which will be analyzed in a next subsection. In conclusion, there should also be mentioned, that every rail contains not only the appropriate threaded holes, which mainly correspond to M2 Bolts, but also the suitable fillets (basically R1) that the specifications recommend.



Figure 30: Main Rail (left), Intermediate Rail (right)

[4] According to Figure 27.

2.3.2 Decks

Decks, also known as crossmembers are very important components that have to connect subsystems, carry the electronics and the batteries and also transfer loads to the chassis wall. Except of that, they increase the stiffness of the entire structure, offering the essential structural integrity and stability. Their general shape was inspired by [28], which however was appropriately modified, so that they will be able to fit into the present 6U-XL. All of them are made of lightweight aluminum so that they do not add significant weight and are arranged in such a way that each pair will form an imaginary 1U unit, as said before. Furthermore, they all have threaded holes for M2 Countersunk type bolts, that will connect them first with the main panels and later with the rails. This type of bolts allows their head to enter completely into the deck's flange without protruding, hence creating additional space for the electronics mounting without affecting them. The exact location of the threaded holes was chosen in such a way as to facilitate the fastening of the bolts during the assembly, considering that each time a complete system of "1U" will enter the interior of the CubeSat. The free space formed in each imaginary 1U system is 86.8 x 106 x 102 mm3 for the bottom and the intermediate system, 86.8 x 106 x 89 mm3 for the top left and 106.5 x 111 x 89 mm3 for the top right system. It is obvious that the top right system is slightly bigger in terms of length and width compared to the others, due to the asymmetry created by the payload's volume. Nevertheless, the fact that both top systems have the same height, allows them having mutual connections with the intermediate rails.

Every system consists of four threaded (M3) rods, every one of which carry the appropriate nuts and standoffs for the electronics mounting. It is important to note that the exact position of the electronic boards, can be adjusted through the brass standoffs, while in fact there will be needed more than just of those shown in CAD. One more thing to consider is that every electronic board should contain suitable holes, that will have a diameter slightly bigger than 3mm, in the appropriate positions, so that the rods will be able to penetrate them and at the same time the desired connection with the standoffs that have a diameter of around 6mm, will be made. As for the nuts, they tighten the rods on every deck, offering the necessary stability, while their position does not allow them to interact with other components. All bolts, nuts and standoffs were downloaded directly as 3D-step files from [29], which provides a wide variety of mechanical equipment. Last but not least, every deck has the appropriate fillets, allowing them not only to have excellent contact with other components, such as the intermediate rails, but also to smooth the stress field, that will be developed during the launch.

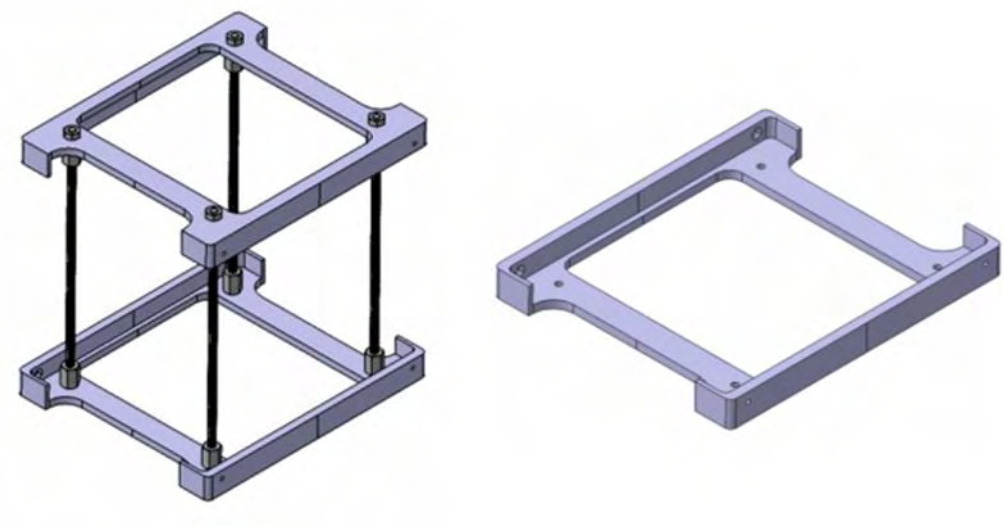


Figure 31: Imaginary 1U System (left), Deck - Crossmember (right)

2.3.3 Side Panels

Side panels have a thickness of 2mm and are some of those components that will be made entirely of composites. They have a shape of a shell which provides them with high stiffness and shear force resistance, however they play a secondary role aiming mainly to enclose the entire structure. They are connected directly to the rails of the CubeSat through four bolts in each case, avoiding the interaction with other components. Unlike decks, they do not carry bolts of countersunk type, because in that occasion it would be very difficult and risky to drill holes with a linear variable diameter in the laminate. For that reason, we use M2 Button Head Hex Drive Screw, with a head protruding by 1.3 mm, which has a minimum effect on the inner free space of the satellite, while the center of each hole locates 3.5mm away from the edge of their flange. The outer surfaces of their flanges are 88 mm apart from each other, whereas their main body locates 10 mm far from the rails, having a total height of 340 mm. Moreover, a length of 6mm, on the lateral face[5] of every side panel, is in full contact with the slots of the main rails, while their edges lean against the main panel's flange. At this point, it is important to mention again that both side and main panels have been designed according to the maximum dimensions that the ISIS specifications advise. For that reason, if any secondary components such as solar panels would like to be installed, there should be the appropriate modifications on the chassis wall's dimensions. The installation of solar panels will obviously require some extra bolts, fact that associates with the drilling of more holes in the chassis wall, however no further reference will be made as the present thesis is mainly focused on the primary structural components.

[5] (flange)

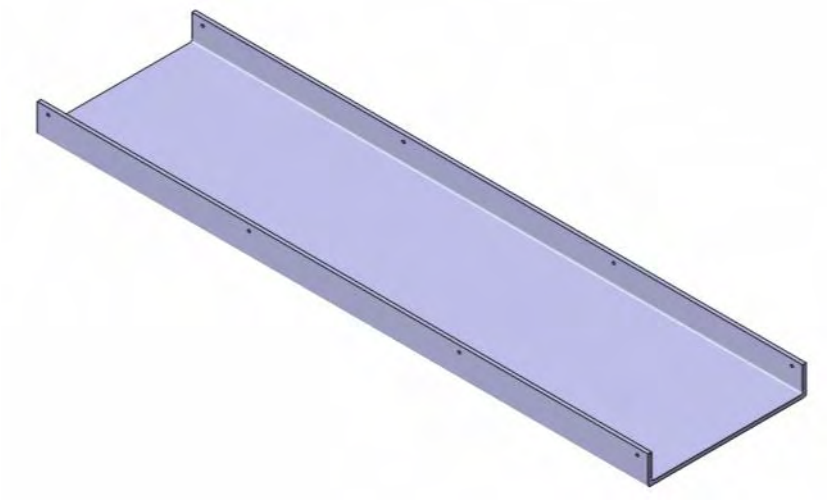


Figure 32: Isometric View of a Side Panel

2.3.4 Main Panels

It is a fact that main panels can be characterized as some of the most critical components of the structure, along with rails. They constitute the connecting ring between decks and rails and carry a very large amount of external loads. Main panels have also a shape of a shell and are made fully of composites with a total thickness of 2mm, however a detailed report on the selected material and its form, will be made in a next chapter. As mentioned previously, one main panel covers the entire back side (-X direction) of the CubeSat, while the other one consists of a primary part that surrounds all the decks and a secondary part that participates in the movement of the robotic arm, when the satellite is in orbit.

The back main panel and the primary part of the front one, have suitable threaded Φ2 holes which center locates 5.5 mm away from the edge of their flange and match up with the stable[6] diameter of the M2

[6] The linear change of the diameter of the holes that correlate with the Countersunk bolts takes place only inside the thickness of the decks. As a result, main panels and rails have threaded holes of constant diameter.

Countersunk bolts, that hold main panels, decks, and rails together. On this point there should also be mentioned, that the connections in which the main panels take part, were considered more critical than those of side panels. For that reason, the length of the main panel's flange is slightly bigger by 2mm, than the side panel one, so that the distance between the hole and the free edge of the flange, can be increased and consequently improving the safety of the connection in the possible event of a shear-out failure mode. It is important to note that on the +Y direction, there are only two top decks that are connected directly to the main panels and the rails. Consequently, two M2 bolts of the same type as the ones that joined side panels with rails, have been used, in order to connect the remaining part of the right flange. As for the dimensions, the total height is 340 mm, the outer surfaces of the flanges are 214.3mm away from each other and the main body locates 10mm far from the rails, hence fulfilling the ISIS specifications. Regarding the sizing of the front main panel, it has a gap that covers an area of 235x114 mm^2 and will allow the movement of the robotic arm, however in general it follows the same dimensions as the back main panel. Lastly, they don't come in contact with the outer surface of the intermediate rails, in order to prevent cold welding and also to allow their independent movement.

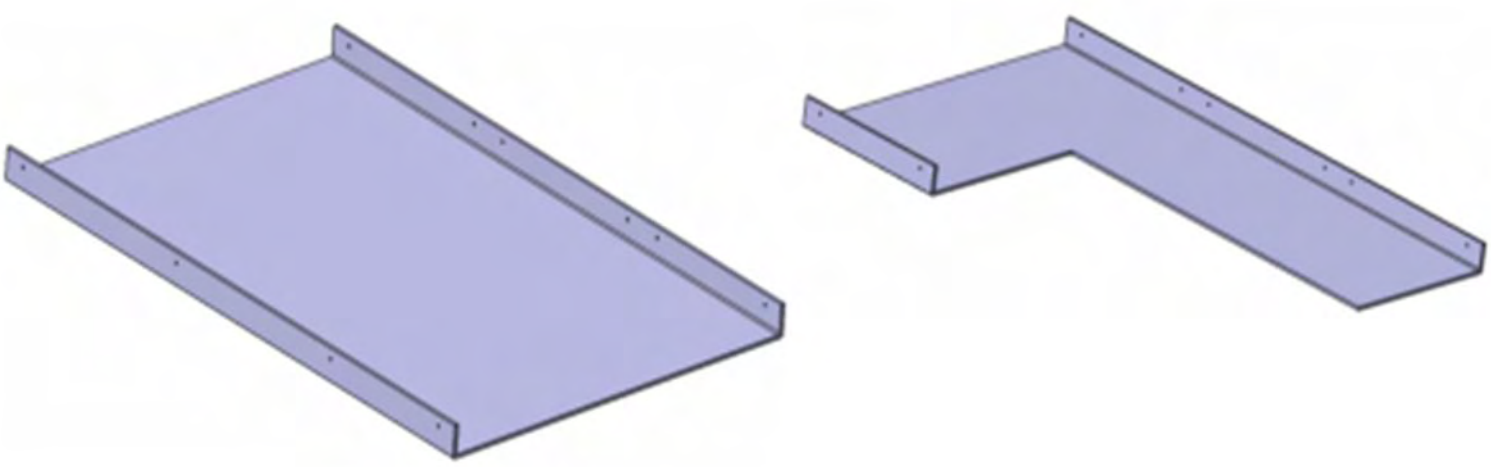


Figure 33: Isometric View of the Back Main Panel (left) and the Primary Part of the Front Main Panel (right)

2.3.5 Top and Bottom Base

Top and bottom base are two identical components, that were designed in such a way as to be, lastly and independently to other parts, inserted into the final assembly. They have a thickness of 2 mm, are also made of composites and their role is to enclose the structure from the ± Z faces. Moreover, they consist of four flanges that are screwed to the main rails through some M2 Bolts, thus ensuring their structural integrity. A remarkable fact is that on the first design iterations, every base was designed with eight flanges in total and every one of them would be screwed separately in the main rails. In that way the contact areas between bases and main rails would have been doubled, which implies greater mechanical stability. However, the increased complexity in the geometry due to those extra flanges, would not allow the smooth placement of the prepreg, which could lead to false orienting fibers, meaning the creation of critical failure areas, already from the manufacturing phase. For securing the stability of the entire structure, it was decided to join the bases with the intermediate rails through four M2 bolts. In this way, all the inner components and the bases can move dependently from each other, hence modelling a (non-existent) rigid body motion, whose movement is strictly limited both by the external connections of the bases and by the internal ones of the decks. All the above reduce the total displacements of the CubeSat's components, making it ready to carry not only the payload but also the additional loads that it will cause when being in a field of increased gravitational acceleration.

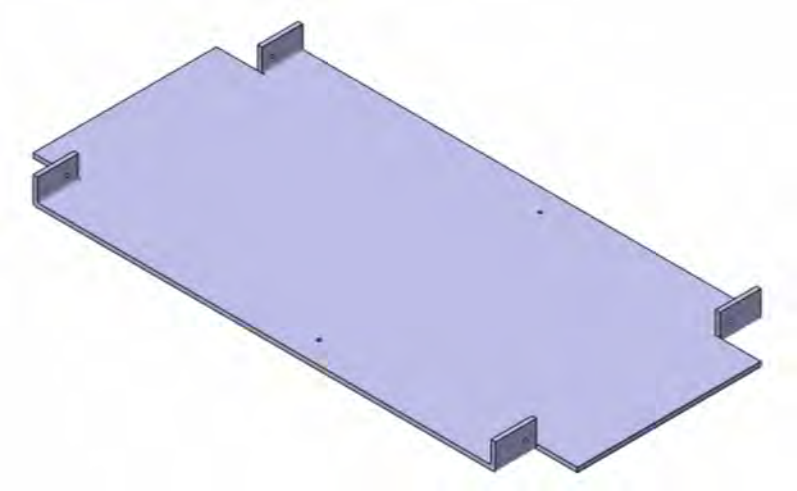


Figure 34: Isometric View of a Base

2.3.6 Deployment System

As referred previously, the main purpose of the present CubeSat's mission, is to deploy a robotic arm in space. It is obvious that a suitable deployment mechanism should be considered and designed with the intention that the appropriate movement of the payload would be allowed. Therefore, two piano hinges, which are widely used in aerospace applications, were considered. Every hinge system consists of a pin that allows the relative rotation between the two parts and a torsional spring that will be compressed during the assembly, in order to save the appropriate energy that will later carry out the movement of the deployable panel. After the deployment process, every spring will come back to its natural position also forcing the entire hinge system to do so, without affecting the free space intended for the robotic arm movement. It is important to note, that both piano hinges were placed in the inner surfaces of the front right rail, so that they will not have any impact on the outer surfaces of it, that take part on the connection between the CubeSat and the POD. At a first stage these hinges were directly downloaded from the Macmaster website [29],

however they were subsequently modified properly in the CATIA environment, so that they are able to fit into the present structure.

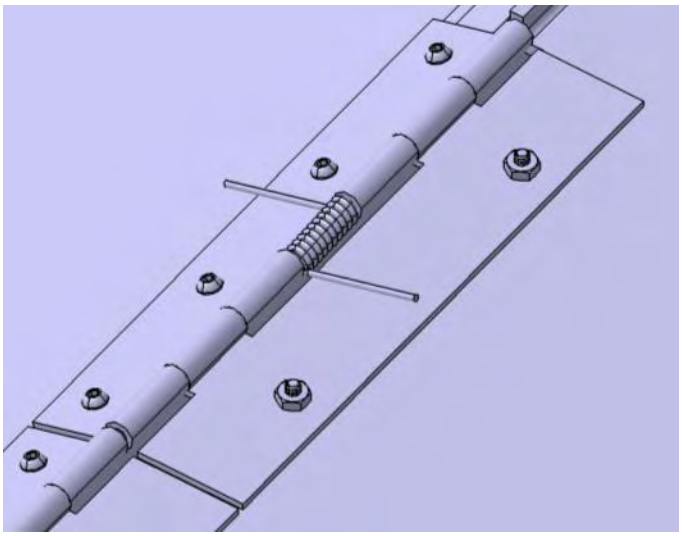


Figure 35: Isometric View of a Piano Hinge

2.3.7 Deployable Panel

This panel constitutes the main part of the deployment system and is made of the same composite material that has also been applied to the rest of the panels, having a total thickness of 2mm. The aforementioned one includes 4 M2 type holes, which contribute to its connection with the piano hinges. Beyond that, it has 2 flanges tending to follow the form of the main panels, which however do not come in contact with the rail so as to allow its movement (i.e. the rotation around the rail). Additionally, these configurations contribute to the maximum possible isolation of the CubeSat's interior from the external environment.

At this point it should be emphasized that for the total completion of the deployment mechanism, it is considered necessary to design and install both a "locking" system, that will secure the deployable panel during the launch and a suitable actuator (e.g. burning wires [30]), which will determine the motion's

onset. These secondary components are not presented as they escape from the initial design-concept, however the current thesis has already paved the way for a future re-engagement and a final integration of the CubeSat's structure.

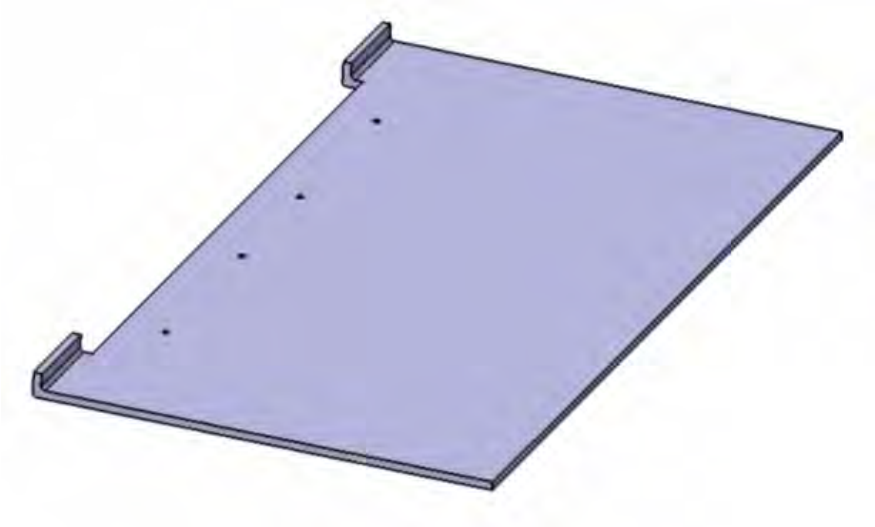


Figure 36: Isometric View of the Deployable Panel

2.4 Assembly

In this subsection, an indicative, but not a necessarily must-followed, way of a total assembly will be presented. It is noted that the following instructions, are mainly referred to the connections between the basic structural components analyzed before, while appropriate modifications will be required in case of installing additional elements.

Every "1U system" will be assembled separately and independently of the others. Firstly, the four rods will be screwed into one[7] deck and then electronic boards, or batteries will be placed on them through

[7] , top or bottom,

the suitable standoffs. In the next place, the second deck[8] will be screwed on the other free side of the rods, and both will be secured through nuts so that they can finally form the desired "1U system". At the end of this process, the four systems with all the electronics mounted on them, will be ready for installation.

In the next step, the intermediate rail which locates on the -X direction will be laid down and at the same every deck-system will be screwed through their back right hole into it. Once more, it is important to mention that the two top deck systems will be connected through the same bolt. Consequently, the second intermediate rail (+X direction) will be inserted, and all the decks will be screwed into it through their front right hole. After that the two side panels will be fastened to the two rails of each side, without affecting yet the assembly that was performed previously. It is worth to note, that on this phase there can also be made the connection between the hinges of the deployment system and the front right rail.

Next, the main panel of the -X face of the CubeSat will be laid down, and on top of that the intermediate rail, that carry all the decks, and the second intermediate rail of the +X face, will be placed. On this stage, the left side panel with the two rails attached, will be inserted and simultaneously all the back left holes of the decks will be screwed into the back left rail, using bolts that also penetrate the left side of the main panel of the -X face. It is true that from this time on, the making of the inner connections between decks, main panels, and rails, will have an extra difficulty due to the mounted electronics that lead to lack of free space. Nevertheless, the back left connections described before, could be made through the +X face, that is free for now or through the +Y face or even by taking advantage of the ± Z levels, as the bases have not been attached yet.

At this time the second main panel that corresponds to the +X face of the satellite can be inserted and screwed into the front left rail, by using bolts that begin from the front left side of every deck. These connections can mainly be made by using the free space of the +Y level. Having done all of that, there can

[8] , with the appropriate orientation as shown before,

now be inserted the right-side panel, with the other two rails attached. Both from the free space, to which the robotic arm will be later attached and the ± Z faces, all the bolts that fasten the top big decks and the back main panel to the back and front right rail, can easily be placed.

In the end, the two bases are inserted and all the bolts that tighten them either to the four main rails or to the two intermediate ones, can easily be screwed from the outside of the structure. Also, the deployable sub-panel can be connected to the deployment system of the front right rail and the robotic arm can now be placed on the inner of the CubeSat. It is noteworthy, that secondary components such as solar panels or antennas, are able to be connected to the outer sides of the chassis wall, however in case some extra element placement inside the satellite is desirable, it must be done before placing the payload.

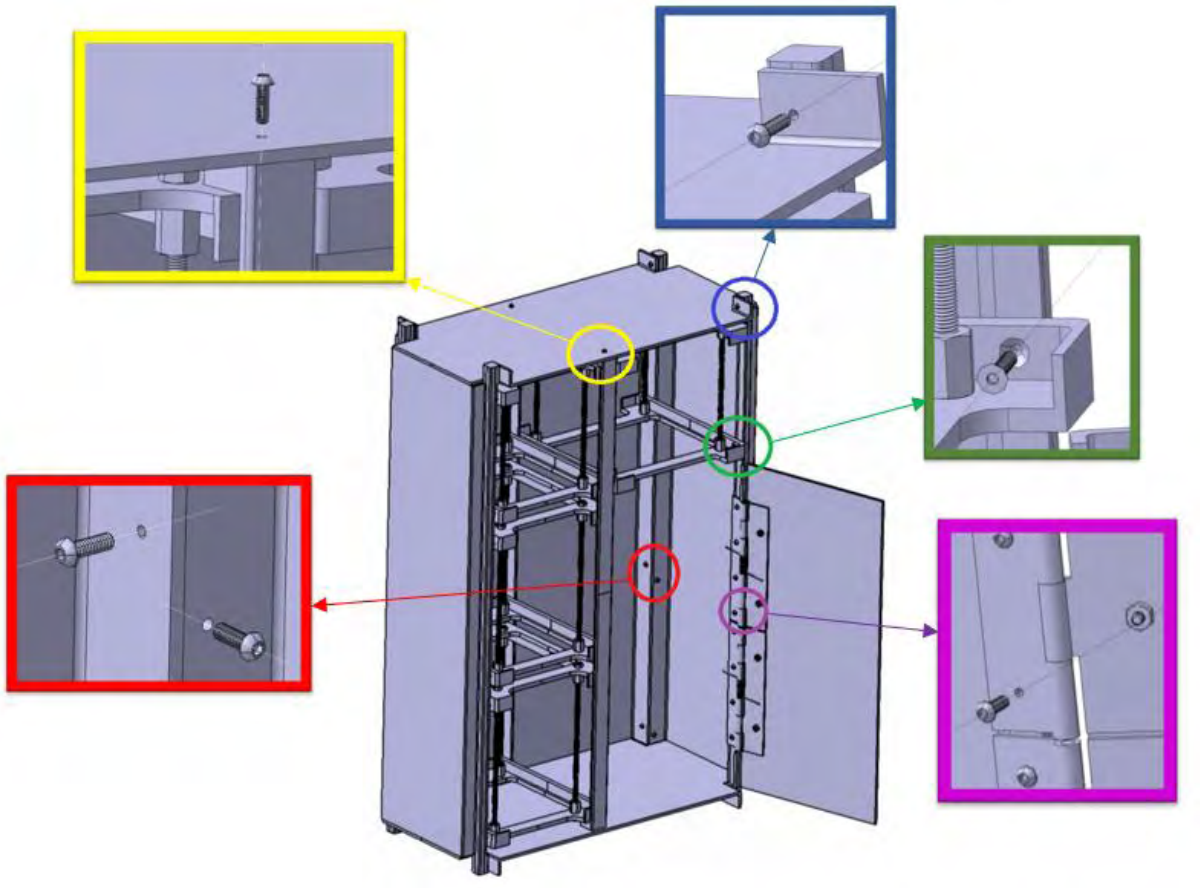


Figure 37: A closer Inspection of the Bolted Connections

3.0 FINITE ELEMENT ANALYSIS (FEA) PHASE

This chapter focuses on the computational analysis performed to study the behavior of the CubeSat's CAD model, that was presented previously. Firstly, a detailed report on the Finite Element Model and the mesh process will be made, while there will be a special discussion about the composite parts modelling. It is important to point out that the design of the CubeSat, which is an iterative process that correlates every type of analysis with the CAD model, is multi-parametric and requires the final structure to have the appropriate strength, stiffness, stability, and modal behavior, in order to be functional in the environmental loads that it will be exposed. Thus, every type of structural analysis will be performed, and the exported results will be discussed, while drawing the appropriate conclusions.

3.1 Simulation Approach

The computational model used to analyze the structural behavior of the CubeSat was in general based on the CAD model as presented in the previous Chapter (page 37). At this point, it should be noted that when performing analyses using the finite element method, it is important to achieve a balance between model's complexity and computational time. It is easily understood that as the model gets more complex and detailed, it is expected that for the same computational capability a much greater processing time will be required. Considering the processing power available, simplifications on the original CAD model were made so that reasonable computational times would be achieved for every simulation.

The most important simplification, that took place was the treatment both of the deployment system and the deployable panel. More specifically, these components were not imported into the finite element

model and as a result, the front main panel is treated exactly as the back one, meaning that it is considered to be screwed directly to the front right rail. Undoubtedly, this simplification may significantly change the behavior of the original structure, however as it was emphasized also in a previous paragraph, the present thesis focuses mainly on the primary components of the satellite and especially on the use of composite materials, with the result that the avoidance of modeling secondary parts like these, doesn't affect the design philosophy that we wanted to follow from the beginning of the design iterations. Nevertheless, the preliminary CAD designs of these secondary components that have already been presented, can pave the way for a future work that will be focused on their detailed design and analysis, which will aim at the full completion of the current CubeSat's model design, that we have developed so far.

Another simplification was to model all the rails and the threaded rods as 1D beam elements. This assumption has the advantage of remarkably decreasing the number of mesh elements and gives us the ability to avoid 3D solid elements, which would require not only the insertion of the quite complex rail's geometry but also a long processing time. Although, through that simplification the accuracy of the model will be decreased, the exported results will remain at reasonable levels as we shall see in a next paragraph. It is worth to mention that despite the fact that these components are modeled through lines in the preprocessor environment, the use of 1-D Beam Elements give us the ability to define both their cross section and orientation, thus giving the necessary accuracy to the FEA model, which in overall will not have any significant geometric difference compared to the original CAD.

An equally important assumption is the modelling of the bolts that join the various components of the structure. More specifically, they were modeled directly through the use of RBE2 Interpolation elements, which allow the user to model the motion of one component's node as a function of the motion of some other component's node, thus offering a Multi-Point Constraints (MPCs). In that way the direct modelling of these components is avoided, and it is noteworthy that in this case, even with the use of 1D Beam Elements, our model would be significantly complicated.

Due to the low thickness to length and thickness to width ratio, all the composite parts can be characterized as thin-walled components and as a result they can be modelled via surfaces. The same approach was followed also in the aluminum decks, which do not strictly follow the above rule, however through that type of modelling, solid elements are avoided[9]. Despite these simplifications, it is important to mention that in both cases, we had the ability to import the appropriate thicknesses into the QUAD4 shell elements, which discretize every surface, depending on their 3D original geometry. It that way, our FEA model approaches the original CAD structure to a great extent.

In closing, another assumption emerged from the previous ones, refers to the treatment of the threaded holes and fillets. As for the first one, it was considered that the modeling of bolts via RBE2 elements, does not require the creation of holes on the surfaces of every deck and panel, because as it is already mentioned these elements are connected directly to a node of each meshed component. It should be noted that every node to whom an RBE2 is connected, represents with great precision the center of each threaded hole as it appears in CAD. Obviously, such an approach reduces the accuracy of our results, especially in the areas near the holes, where there is a concentration of stresses, however to a wider range of results that we are concerned, it does not greatly affect the overall behavior of the FEA model. Regarding to the second one, it is a fact that fillets are significant features on the engineering model for design, manufacturing, and mechanical reasons. On the other hand, for a simulation model, they are usually neglected because the improvements on the results that they offer, do not compensate the amount of additional processing time demanded by them. Based on all the above simplifications, additional safety factors have been considered so as to counterbalance any defects of the FEA model in relation to the original CAD.

[9] , which undoubtedly have very long processing time given our currently available computing power

3.2 Computational Model

The computational model used to analyze the structural behavior of the 6U-XL CubeSat was based on the CAD structure and was satisfying all the appropriate simplifications mentioned previously. It is noteworthy that due to the geometric complexity of the four main rails, they were modeled through suitable CBAR (1D-BEAM) elements which were characterized by a symmetrical compact square cross section of 6x6 mm2, so as to model their weakest form, which in the actual CAD occupies the longest length of them. Following the same philosophy, the two intermediate rails were modeled through suitable CBEAM (1D-BEAM) elements that include the actual (unsymmetric-compact) CAD cross section. As for the rods, they were modeled through CBAR elements due to the symmetry of their circular (Φ3) cross section.

Regarding the discretization of the surfaces, shell QUAD4 elements were used following the IsoMesh mesher methodology. Each deck contained surfaces, which were placed on the middle planes of the actual 3D geometry and had different thicknesses (3.5 or 3 or 1.5 mm) that agreed with the CAD model, while the composite panels had a constant thickness of 2mm throughout their length. It is also important to note that the number of elements discretizing each component were based on an appropriate mesh convergence study. The total number of elements and points that were used for the discretization of the entire FE model is shown in Figure 38.

M O D E L S U M M A R Y

ENTRY NAME	NUMBER OF ENTRIES
CBAR	6336
CBEAM	1360
CORD2R	6
CQUAD4	542423
RBE2	110
GRID	571970

Figure 38: FE Model Summary

Concerning the boundary conditions, the entire CubeSat was considered as fully clamped both on the top and bottom face of every main rail. Admittedly, the best possible modeling was to restrain the 6 DOFs of the outer surfaces of these rails, such as *A. Ampatzoglou* [20] mentioned in his work, however such a treatment was not possible in the current thesis due to the avoidance of using 3D solid elements. Nevertheless, the present modelling is quite satisfactorily compatible with the actual placement of the CubeSat inside the POD.

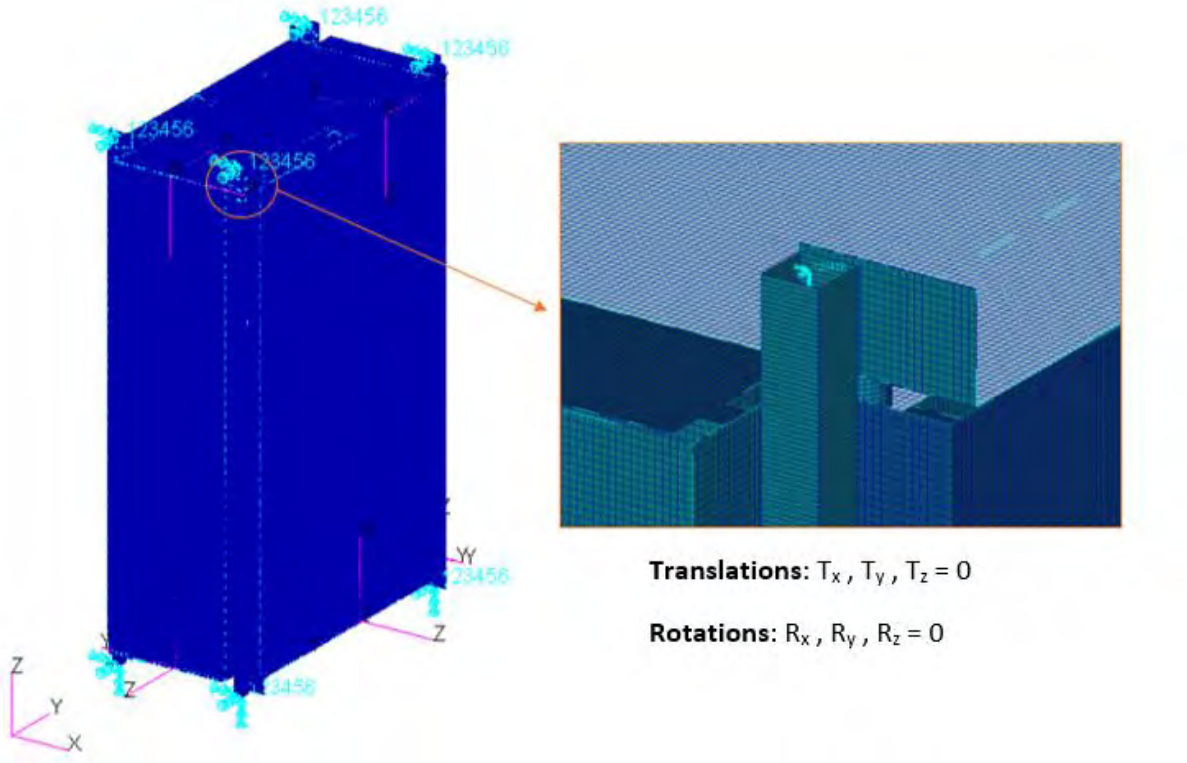


Figure 39: Boundary Conditions applied on the FE Model

In closing, it was calculated that the total mass of the FE Model is **1.893 kg**, which is very close to the CAD's, given the fact that in the present simulation the modeling of either bolts or nuts, along with the fillets and the holes of each component was avoided.

Additionally, in Figure 40 one can see the exact position of the CubeSat's Center of Gravity measured in mm and referred to the global XYZ coordinate system, which is also presented in the three-dimensional space in Figure 41[10] All simulations were performed using MSC Patran - Nastran 2018 software.

Summary Display of Center of Gravity, Principal Inertias, Radii of Gyration, Mass, and Volume

	CG(CID 0)	CG(CID 0)	I-Principal	Radii of Gyr.	Mass	Volume
1	5.000E+01	5.000E+01	3.563E+01	1.372E+02	1.893E-03	8.775E+05
2	1.037E+02	1.037E+02	2.749E+01	1.205E+02		
3	1.925E+02	1.925E+02	1.602E+01	9.201E+01		

Figure 40: Center of Gravity position (mm), Mass (tons) and Volume (mm^3)

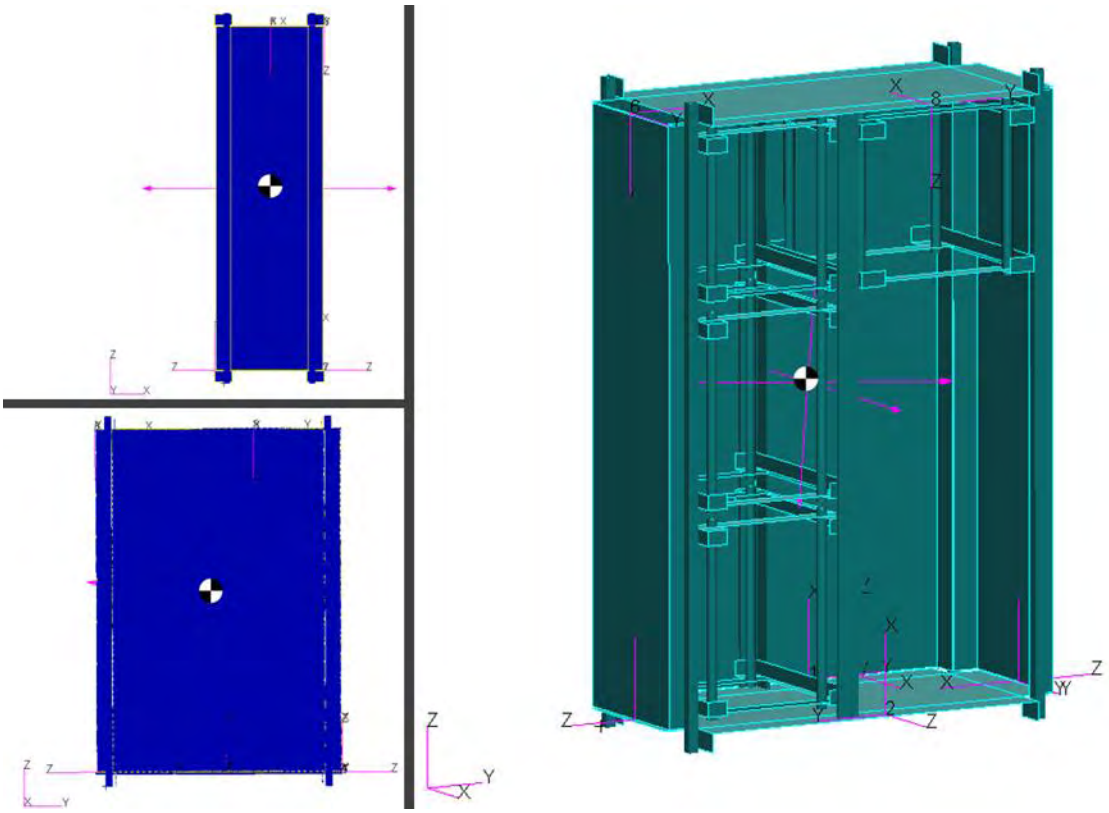


Figure 41: Representation of the CG in the 3D Space

[10] The global XYZ coordinate system, for the FEA model, is located on the center of the bottom face of the back left rail according to Figure 41, while for the CAD model, the global XYZ system locates on the bottom left edge of the front left rail, hence the x coordinate of the CG has opposite signs on each model.

3.3 Material Properties and Composites Modeling

As mentioned in the previous chapter (page 37), for decks, threaded rods and rails, **Aluminum 7075-T6** alloy properties were considered, while CFRP properties were assigned in all panels and bases of the structure. The chosen CFRP is a space approved unidirectional prepreg, according to the ECSS-E-HB-32-20 Part 1A handbook [31], called **T300/Fibredux 914** and its properties are presented in Table 4. Concerning the lamination of the composite parts, a **π/4 quasi-isotropic layup [0/45/90/-45]2S** with a total thickness of **2mm** was selected. It is necessary to note that due to the fact that the placing direction of the CubeSat inside the POD and consequently the exact directions of the external loads are unknown, the quasi-isotropic layup was a one-way choice. Based on the above uncertainty , it was considered that the π/4 form offers the necessary stiffness and strength in all of the directions of the structure, while simultaneously saves a considerable amount of weight compared to an all-aluminum chassis wall.

This stacking sequence was inspired by the UPSAT's [20] chosen layup [0/45/90/-45]S , which however could not be applied in the current application due to the fact that the total thickness of 1mm greatly reduced the eigenfrequencies of the structure, hence creating a high risk of a possible resonance. Thus, by imposing one more symmetry, the thicknesses of the composite parts were doubled, bringing the eigenfrequencies to an appropriate level, while maintaining the positives of a both symmetrical and quasi-isotropic lay-up. Although the acceptable behavior to modal analysis, the CubeSat must also meet certain criteria of strength and stability, which will be discussed in the next subchapter.

The composites modeling was performed through a tool that MSC PATRAN 2018 Preprocessor provides, called MSC Laminate Modeler. Regarding the local coordinate system for the CFRP faces, the 0^0 direction was considered along the length (Z-Axis) of the main (± X faces) and side (± Y faces) panels while for the bases (± Z faces) the 0^0 direction is along the Y-Axis (Global Reference XYZ coordinate system). As for the manufacturing phase, it is essential to consider that every ply is viewed from the inside

of every component looking toward to the tool surface, meaning that every +45° layer is located by moving counterclockwise from 0° to the 90° ply. Besides that, it should be underlined once again that identical parts such as the two main panels or the two side panels and the two bases, are manufactured in exactly the same way, and placed appropriately within the CubeSat's structure.

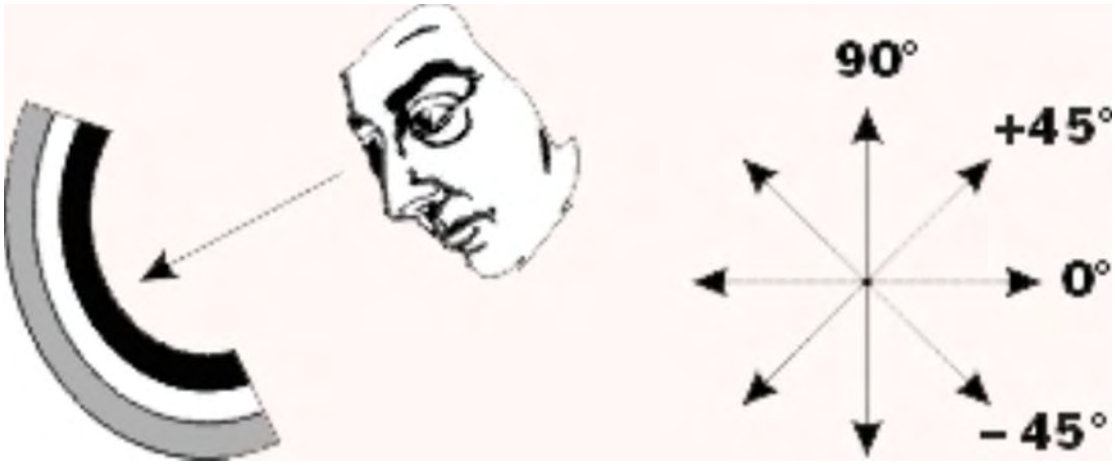


Figure 42: Manufacturing Standpoint of the Current Layup [32]

All the material properties used for the FE model are summarized in Table 4, and Figure 43 illustrates the properties assignment on the assembly (for the major structural components).

Table 4: Material Properties of the FE model

MATERIALS		
Aluminum 7075-T6		
Type	Isotropic	
Application Region	*Rails, Decks, Threaded Rods*	
Linear Elastic Properties	E_1 (GPa)	71.7
	Poisson Ratio v_{12}	0.33
	G_{12} (GPa)	26.96
	ρ (kg/m^3)	2810
Failure Properties	Yield Tensile Strength (MPa)	503
	Yield Compression Strength (MPa)	503
	Shear Strength (MPa)	330

CFRP T300/914		
Type	Laminate, 2D Orthotropic	
Fiber Volume (%)	61.5	
Ply Thickness (mm)	0.125	
Application Region	*Panels, Bases*	
Linear Elastic Properties	E_1 (GPa)	138.1
	E_2 (GPa)	8.92
	Poisson Ratio v_{12}	0.37
	G_{12} (GPa)	4.97
	G_{23} (GPa)	3.08
	G_{13} (GPa)	4.97
	ρ (kg/m^3)	1580
Failure Properties[11]	Tension Stress Limit X_t (or X_{11}) (MPa)	1573
	Tension Stress Limit Y_t (MPa)	36
	Compression Stress Limit X_c (MPa)	900
	Compression Stress Limit Y_c (MPa)	200
	Shear Stress Limit S (or S_6) (MPa)	87
	Bonding Shear Stress Limit (MPa)	80
	Tsai-Wu-EPFS Interaction Term F_{12}	-3.53E-07

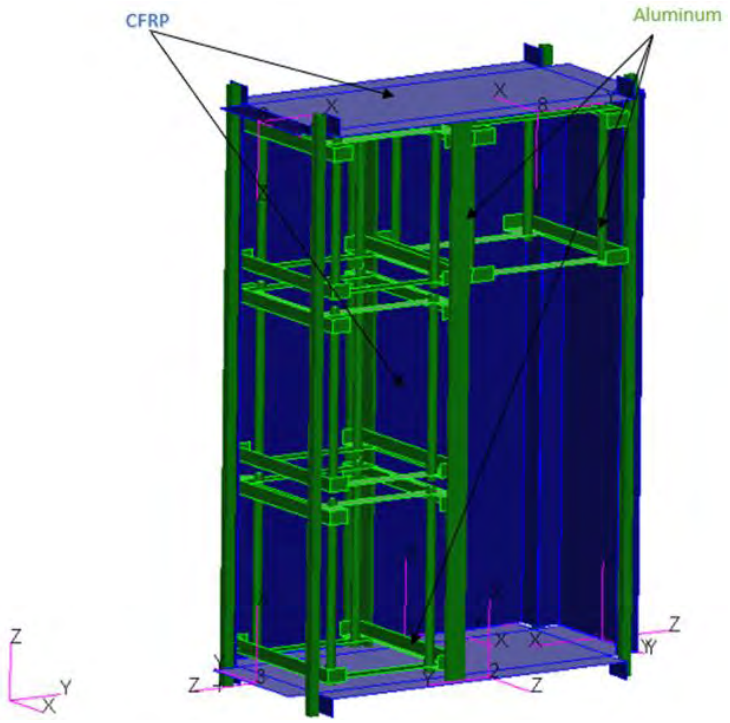


Figure 43: Material Properties Assignment on the Assembly

[11] The X stress limit refers to the longitudinal (fiber) direction whilst Y stress limit refers to the transverse direction.

3.4 Modal Analysis

Normal mode analysis also known as modal analysis, is the study of the dynamic properties of a system, which contains the computation of both the natural undamped frequencies and the natural undamped mode shapes. The motion equations for a normal modes analysis of a multi-degree freedom system can be represented in a matrix form as follows :

$$[M]\{\ddot{u}\} + [K]\{u\} = 0 \tag{21}$$

, where *[M]* is the mass matrix, *[K]* the stiffness matrix, *u* a vector that contains the displacement of every node and $\ddot{u}$ a vector which defines the acceleration of every node. Essentially, modal analysis describes a free–oscillation problem, in which by assuming a suitable solution one can end up in the Generalized Eigenvalue Problem described by the equation (22) :

$$(-\lambda_n[M] + [K])\{\varphi_n\} = 0 \tag{22}$$

, where $\lambda_n = \omega_n^2$ is the n-th eigenvalue, ω_n refers to the n-th natural frequency and φ_n is its corresponding eigenmode. It is important to note that *[K]* is symmetric, *[M]* is a both symmetrical and positive defined matrix, while φ_n are real numbers and $\lambda_n > 0$. Based on that and assuming concentrated mass sub-matrixes, it is possible to switch the Generalized Eigenvalue Problem into a Standard Eigenvalue Problem represented as :

$$(-{\omega_n}^2[I] + [M]^{-1}[K])\{\varphi_n\} = 0 \tag{23}$$

In general, modal analysis is one of the most important steps an engineer must follow during a design process. Basically, it testifies the (responding) behavior of a system during any external dynamic load. In that way, it enables the engineer to control and at the same time to drive the resulting oscillation of the structure at desired levels which correspond to a safe operating zone. Hence, any resonance condition which leads to failure can be avoided.

However, the greatest contribution of a normal modes analysis falls on the matter of the basis it provides for further dynamic analysis, seeing as the deflected shape of a structure subjected to free or forced vibrations may be considered as a linear combination of the various modes.

In this case, the Shifted Block Lanczos Method [33] will be used, according to which the first 10 natural frequencies of the CubeSat's model will be calculated. The first of those frequencies is called fundamental frequency and is listed along with the others in Table 5. Lanczos algorithm is recommended and used for a wide range of applications, mainly in those that require the extraction of a large number of eigenmodes (>40), while at the same time it is the «default» method in most Finite Element softwares as it does not create instability problems while solving. Also, it is usually applied to complex models, which combine various types of finite elements such as solids, shells and beams.

Table 5: The first 10 Natural Frequencies of the Structure

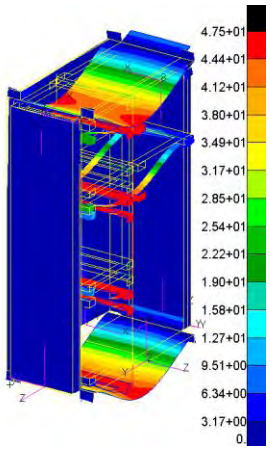
No	Natural Frequency [Hz]	Type
1	159.16	Bending
2	175.05	Bending
3	175.2	Bending
4	215.32	Bending
5	215.7	Bending
6	294.59	Bending
7	294.89	Bending
8	310.11	Torsional
9	322.84	Torsional
10	360.11	Torsional

Regarding the natural frequencies the only requirement needs to be satisfied is that the fundamental frequency must be above the separation module's 1st natural frequency in order to avoid any resonance conditions. According to the results of the Table 5, the lowest frequency sits comfortably above the 100 Hz minimum resonant frequency required in hard-mounted configuration, as per [34].

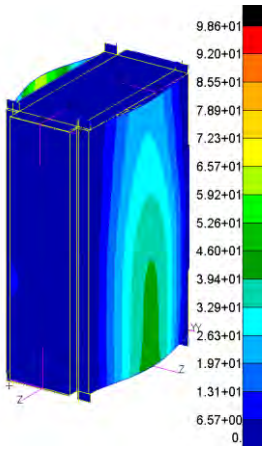
As for the mode shapes, they are intended to give information only about the shape of each eigenfrequency and not about the amplitude of that vibration, which depends both on the natural frequency and the applied loads. Hence, the results of Figure 44 correspond only to a relative displacement, giving an idea of shape that should be expected when the structure is vibrating in a specific frequency.

A deeper look at the first eigen-mode shows that the aluminum decks are the main characters, which is in line with the fact that they are the heaviest components of the structure and comparatively to the composite panels, have lower stiffness. This fact leads them to have the smallest stiffness to mass ratio and as expected they become the elements that will oscillate first in the frequency domain. Beyond this, due to the connections through RBE2 with the composite bases, they will also be led to take some shape at this specific frequency, regardless of whether they have a greater stiffness to mass ratio.

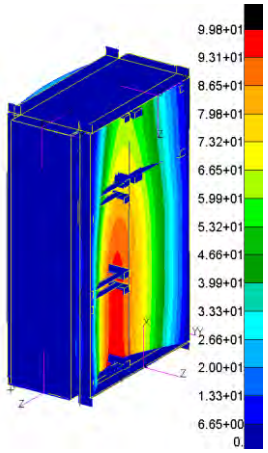
An equally important observation is that all the bending eigen-modes, with the exception of the first one, correspond approximately per two to a common natural frequency, fact that implies to the almost simultaneous oscillation of symmetrical components such as the main panels of the CubeSat. As one moves to higher frequencies, the mode shapes become more and more complicated, with the typical example of the 8^{th} eigen-mode, which has a torsional nature and seems to affect both panels and decks at the same time.



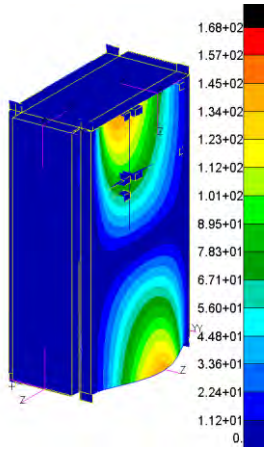
1st Eigen-Mode **[159.16 Hz]**



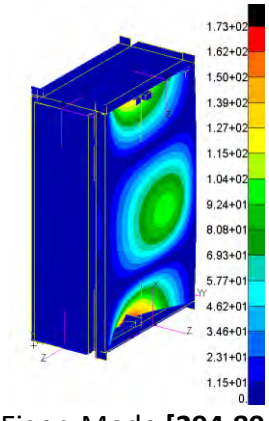
2nd Eigen-Mode **[175.05 Hz]**



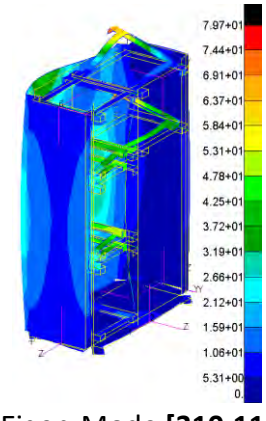
3rd Eigen-Mode **[175.2 Hz]**



4th Eigen-Mode **[215.32 Hz]**



7th Eigen-Mode **[294.89 Hz]**



8th Eigen-Mode **[310.11 Hz]**

Figure 44: Mode Shapes of the 6U-XL CubeSat

3.5 Quasi-Static Analysis

Quasi-static loads are normally calculated by combining both static and dynamic loads. According to [35] the applied quasi-static loads do not induce dynamic behavior due to their low variation with time. They are equivalent to static loads and commonly expressed as equivalent accelerations (Inertial Loads) at the C.o.G location. In general, this type of simulation follows all the assumptions of a linear static analysis, meaning that all the materials have a linear elastic behavior while the nodal displacements are considered to be small. The general equation to be solved in a linear elastic analysis, which describes the relationship between external loads and the internal response of a structure, is given by (24) :

$$[K]\{u\} = [F] \tag{24}$$

, where $[K]$ is the stiffness matrix of the entire structure, u are the nodal displacements and $[F]$ the applied forces vector. From (24) the displacements at each grid point of the overall discretized structure can be obtained and subsequently the stresses and strains of the finite elements are calculated.

For the current thesis, the equivalent acceleration is **30g** and has to be applied on the CubeSat's C.o.G in each major axis at a time. Based on the inertial load of 13g assumed in the UPSAT analysis, some additional safety factors were added, the product of which equals to 2.3 and leads approximately to the ultimate load of 30g. It should be noted that UPSAT's load (13g) includes already both a material factor, which covers the uncertainty of the mechanical properties and a load factor that ensures safety in the event of an increase in the maximum acceleration, according to the specifications of the rocket. In this case, the placement of an extra safety factor (2.3), on the already existing one, not only ensures the overlapping of the uncertainty of hydrothermal phenomena's effect that play a crucial role in a design with composite materials, but also it mainly covers the lack of accuracy of the FEA model.

It is a fact that other similar works receive smaller accelerations (or safety factors) with characteristic examples being *Andreas* [20] who receives a total safety factor of 1.25, *Giorgio* [36] who uses 13g with a safety factor of 1.8, *Maria* [37] with a use of 10.05g and *Miguel* [38] who adopts an inertial load of 19g.

Generally, a material is considered to be in an elastic state if it has the ability to return to its original shape and size, when the external forces that cause the deformations are removed. More specifically, in this state all processes are reversible if the elastic limit, which is represented as σ_y (also known as yield strength), is not exceeded. The maximum distortion energy criterion (also called von Mises yield criterion) is widely used to predict yielding of ductile materials, such as metals, under complex loadings from the results of uniaxial tensile tests.

$$\frac{1}{6}[(\sigma_{11}-\sigma_{22})^2+(\sigma_{22}-\sigma_{33})^2+(\sigma_{33}-\sigma_{11})^2+6({\sigma_{12}}^2+{\sigma_{23}}^2+{\sigma_{13}}^2)]=k^2 \quad (25)$$

, where σ_{ij} are the stress tensor's elements, while k is the material's yield stress. For uni-axial stress the equation (25) reduces to :

$$\frac{\sigma^2}{3}=k^2 \quad (26)$$

Thus, if σ reaches the elastic limit, σ_y , equation (26) takes the form :

$$\frac{{\sigma_y}^2}{3}=k^2 \quad (27)$$

Combining equations (25) and (27) and solving for the von Mises stress σ_v[12], which equals to ${\sigma_v}^2=3k^2$, the general von Mises equation is extracted :

$$\sigma_v=\sqrt{\frac{1}{2}[(\sigma_{11}-\sigma_{22})^2+(\sigma_{22}-\sigma_{33})^2+(\sigma_{33}-\sigma_{11})^2+3({\sigma_{12}}^2+{\sigma_{23}}^2+{\sigma_{13}}^2)]} \quad (28)$$

[12] The von Mises stress does not actually express a true stress, it is a theoretical value that allows the comparison between the general 3-D stress with a uniaxial yield stress limit.

To conclude, if the von Mises stress σ_v is greater than the yield strength σ_y, then the material is expected to yield, which directly results in the failure of the structure. This criterion will be applied to all the aluminum parts of the CubeSat and the appropriate conclusions will be drawn.

It is a fact that the anisotropic nature of composites does not allow them to follow common failure theories that apply to monolithic materials such as metals. For polymer matrix composites (PMCs), which are the most usual class of composite materials, the failure concept must be modified significantly. Hence, von mises criterion which refers to ductile materials such as aluminum, cannot be applied to the current PMC cause of the brittle nature of the carbon fibers. According to [39], concerning yielding as initiation of plastic flow, polymers along with fibers of glass or carbon, which are the ordinary constituents of PMCs, do not have shear-driven thresholds for inelastic behavior as in metals.

The Tsai-Wu failure criterion is a phenomenological material failure theory which is widely applied to anisotropic composite materials with unequal tensile and compressive strengths. This criterion is a specialization of the general quadradic failure criterion and can be expressed as :

$$F_{ij}\sigma_{ij} + F_{ijkl}\sigma_{ij}\sigma_{kl} \leq 1 \tag{29}$$

, where $i,j,k,l = 1,...,3$, σ is a 2nd order symmetric stress tensor, while F are commonly called failure tensors and are generally depended on the material properties. Some of the most important advantages of the tensor failure polynomial of the equation (29) is that it can consider the different tendency to failure due to tension or compression or shear loads, which is experimentally observed in anisotropic materials, whilst it has an unaltered form. In the case of an orthotropic lamina, described by a general state of plane stress in which stresses are expressed through the Voigt notation, the theory of strength proposed by Tsai-Wu takes the form :

$$F_1\sigma_1 + F_2\sigma_2 + F_{11}{\sigma_1}^2 + F_{22}{\sigma_2}^2 + F_{66}{\sigma_6}^2 + 2F_{12}\sigma_1\sigma_2 \leq 1 \tag{30}$$

$$F_1 = \frac{1}{X_t} - \frac{1}{X_c} \qquad F_2 = \frac{1}{Y_t} - \frac{1}{Y_c} \qquad F_{11} = \frac{1}{X_t X_c}$$

$$F_{22} = \frac{1}{Y_t Y_c} \qquad F_{66} = \frac{1}{S^2}$$

One of the most interesting points that deserves to be emphasized, is the determination of the F_{12} term. In accordance with Tsai-Wu [40], every F_{ij} stress interaction term ($i \neq j$) can be experimentally defined through biaxial tests. The magnitude of F_{12} is, however, constrained by the following inequality known as "stability criterion"[13] :

$$F_{11}F_{22} - F_{12}^2 > 0 \tag{31}$$

Because of the very low values that characterize the F_{ij} terms, Narayanaswami and Adelman [41] have suggested that $F_{12} = 0$, which is a preferred alternative to the experimental determination described previously. Although, this formulation of the criterion does not give bad predictions for un-axial problems, it is not recommended to be used for general plane stress or 3D- stress state.

In contrast with the previous one, Tsai-Hahn recommended a theoretical calculation of F_{12} term, which is described below. The predictions of this criterion are identical to those of von Mises for material properties that tend to the isotropic state.

[13] , which indicates that the failure surface is to be closed and convex.

$$F_{12} = -\frac{1}{2}\sqrt{F_{11}F_{22}} \tag{32}$$

Later, the generalization of the F. Stassi criterion, led to the Elliptic Paraboloid Failure Surface theory [42], which assumes that the hydrostatic axis in the principal stress field is a safe load path only in the direction of hydrostatic compression. According to EPFS, the term of F_{12} is calculated from equation (33), whilst it makes very satisfactory predictions in composites with brittle matrix (such us epoxy resins).

$$\boldsymbol{F_{12} = \frac{1}{2}(F_{33} - F_{11} - F_{22})} \tag{\boldsymbol{33}}$$

, where $F_{33} = \frac{1}{Z_t Z_c} = \frac{1}{Y_t Y_c} = F_{22}$ (for UD laminas).

Failure criteria are usually expressed as functions of the stress tensor components in the form of :

$$f(\sigma_{ij}) \leq 1 \tag{34}$$

In fact, the verification of the above inequality through the substitution of the stresses ensures the safety of this specific stress space, which is directly associated with the avoidance of the structure's failure. According to [43], NX Nastran names the value of the left-hand side of the above inequality (34) as failure index. More specifically, the failure indices represent a phenomenological failure criterion in which only an occurrence of a failure is indicated and not the mode of failure.

- If the failure index is <1, the ply stress is interior to the periphery of the failure surface and the lamina is considered to be safe.
- If the failure index is >1, the ply stress is exterior to the periphery of the failure surface and the lamina is considered to have failed.

In order to have an answer with quantitative characteristics (not just failed or safe), the concept of Strength Ratio[14] (SR) is introduced. Strength ratio is a more direct indicator of failure than the failure index, since it demonstrates the percentage of the applied load to the failure criteria. It is defined as :

$$Strength\ Ratio\ (SR) = \frac{\sigma^a}{\sigma} = \frac{Allowable\ Stress}{Calculated\ Stress} \tag{35}$$

For instance, a SR = 0.8 not only indicates that failure has occurred, but also implies that the applied load is 20% above the allowable, meaning that an increase by approximately (depending on the problem) 20% of the lamina's thickness is required so as to avoid failure. On the other hand, a failure index which equals to 1.2 does not represent a percentage of failure, only that a failure condition exists.

Replacing the allowable stress with (SR × Calculated Stress), the Tsai-Wu criteria can be rewritten in terms of strength ratio:

$$F_1 \mathrm{SR}\sigma_1 + F_2 \mathrm{SR}\sigma_2 + F_{11}\mathrm{SR}^2{\sigma_1}^2 + F_{22}\mathrm{SR}^2{\sigma_2}^2 + F_{66}\mathrm{SR}^2{\sigma_6}^2 + 2F_{12}\mathrm{SR}^2\sigma_1\sigma_2 = 1 \tag{36}$$

Rearranging into quadratic equation format:

$$[F_{11}{\sigma_1}^2 + F_{22}{\sigma_2}^2 + F_{66}{\sigma_6}^2 + 2F_{12}\sigma_1\sigma_2]\mathrm{SR}^2 + [F_1\sigma_1 + F_2\sigma_2]\mathrm{SR} - 1 = 0 \tag{37}$$

Using the general quadratic equation solution, the Tsai-Wu strength ratio can be calculated as[15]:

$$SR = \frac{-b + \sqrt{b^2 - 4ac}}{2a} \tag{38}$$

$$a = [F_{11}{\sigma_1}^2 + F_{22}{\sigma_2}^2 + F_{66}{\sigma_6}^2 + 2F_{12}\sigma_1\sigma_2]$$

$$b = [F_1\sigma_1 + F_2\sigma_2]$$

$$c = -1$$

Because of the direct relation of Strength Ratios and the calculated stresses, it is easily understood that in a FEA model these quantities should be computed on an element-by-element basis. It is noteworthy

[14] , which in many sources is also known as safety factor (SF) or reserve factor (RF).
[15] The strength ratio is obtained from the smallest positive root.

that for the indication of satisfying the strength requirement, the Margins of Safety term was used, which is totally related to the strength ratio of the respective finite element, according to equation (39) :

$$Margins\ of\ Safety\ (MOS) = SR - 1 \tag{39}$$

It is known that as soon as the stress field that acts on a finite element, coincides with the (allowable) stress limit, the structure will be led to failure. As seen from equation (35), failure leads to a strength ratio (SR==1), that subsequently results to a MOS==0, which reflects the absence of safety and essentially testifies the Limit State Failure. Therefore, to ensure the safety of the structure, MOS must be greater than zero (>0) or similarly strength ratio should be greater than one (>1), in each of the finite elements.

Remarkable is the fact that layers of a laminate, that have dissimilar fiber orientations, generally fail at different magnitudes of the external loads. By calculating the strength ratios of each layer, one can determine the ply that will fail first. The state in which the magnitude of the external loads is such that the layer with the smallest strength ratio fails, is called first ply failure and is commonly known as FPF. According to FPF state, the micro-mechanisms of the layer failure mainly consist of cracks in the matrix that propagate parallel to the fiber's direction, while the percentage of broken fibers becomes insignificant. Essentially, the FPF load of a laminate, corresponds to the initiation of the aforementioned failure mechanisms and the design concept, which is based on the non-exceeding FPF limit, aims at dimensioning in such a way as to avoid the development of micro-cracks, the evolution and propagation of which are difficult to forecast effectively [11].

In all the quasi-static cases, an FPF-design concept was followed, while for all the CFRP sides the Tsai-Wu criterion with an interaction term according to EPFS was applied. As for the aluminum parts the von Mises criterion was considered. Regarding the stiffness requirements, the entire field of nodal displacements is captured, the maximum magnitude value of which is extracted and commented appropriately for each case.

3.5.1 1st Quasi-static case with -30g inertial load on xx direction

At a first stage, it is possible to observe that during the 1st quasi-static case the structure has a maximum displacement of 0.349 mm, which is presented in the middle of the front (+X face) main panel. It is important to note that the displacement field of Figure 45 is illustrated on a model scale, aiming to become detectable enough, while the maximum value, which can be considered relatively small, ensures that there is no destructive interaction with other possibly existent CubeSats or the POD itself.

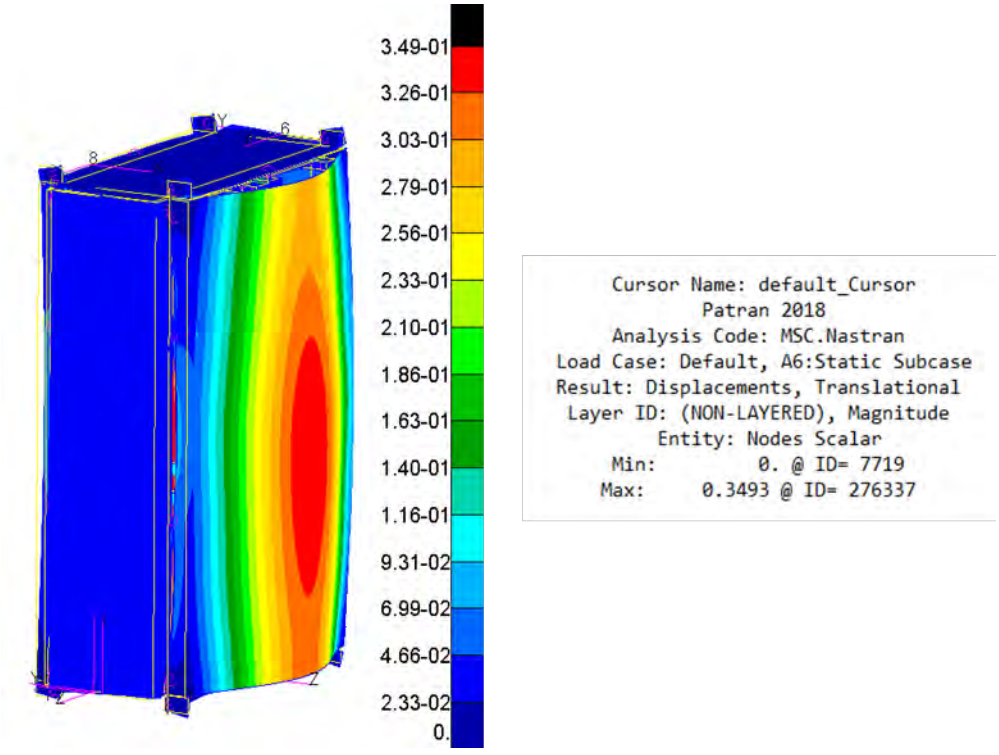


Figure 45: Displacement Distributions [mm] of the 1st Case

Followingly, Figure 46 captures the maximum principal stresses and strains distributions of the entire model. Unfortunately, PATRAN's post-processor illustrates, automatically, nodal stresses and strains fields, hence according to the FEA-theory, no reliable conclusions can be drawn from this phase. Despite that, Figure 46 provides a sense of the critical failure areas, while it is one of the most representative ways to simultaneously capture stress results for both aluminum and composite parts. As expected, the critical values are identified around the nodes that are connected with RBE2 elements, which correspond to the bolted connections.

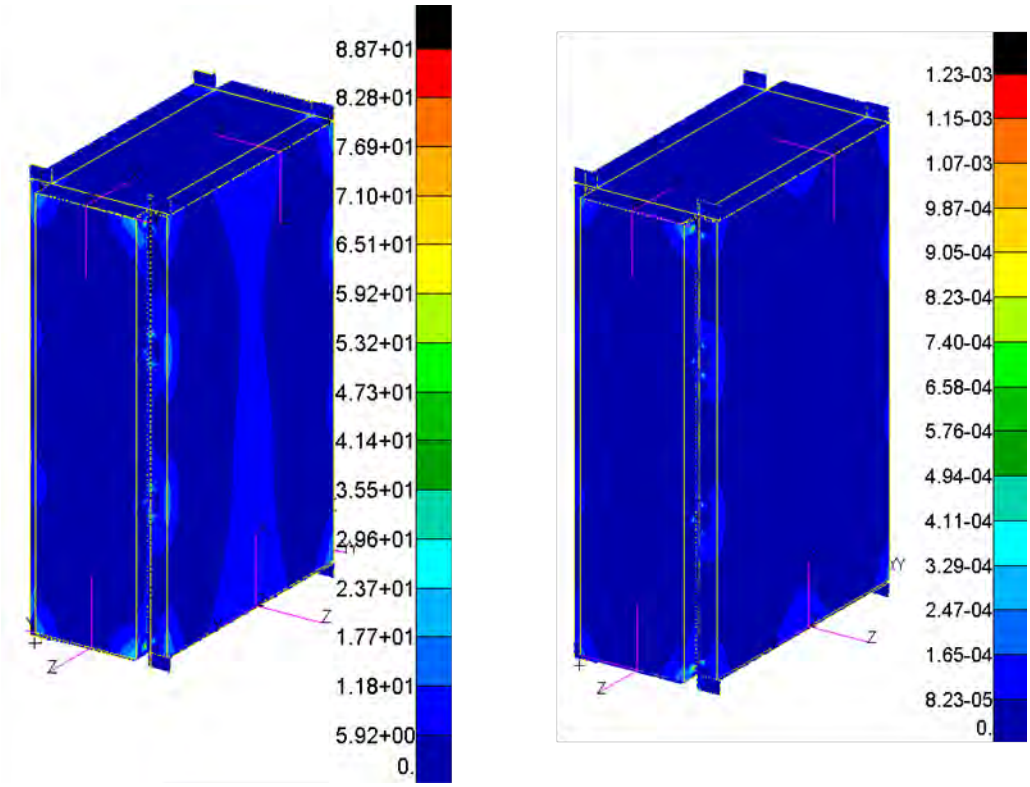


Figure 46: Max Principal Stresses [MPa] (left) and Max Principal Strains [-] Distributions (right) of the 1st Case

Afterwards, Figure 47 presents the von Mises stresses on all the aluminum decks. As seen, the maximum stress takes the value of 25.14 MPa, appears on the bottom big deck and more precisely on the front (+X direction) left RBE2 connection. Considering that the yield strength of the Al 7075-T6 equals to 503 MPa, the above stress value can be regarded as insignificant.

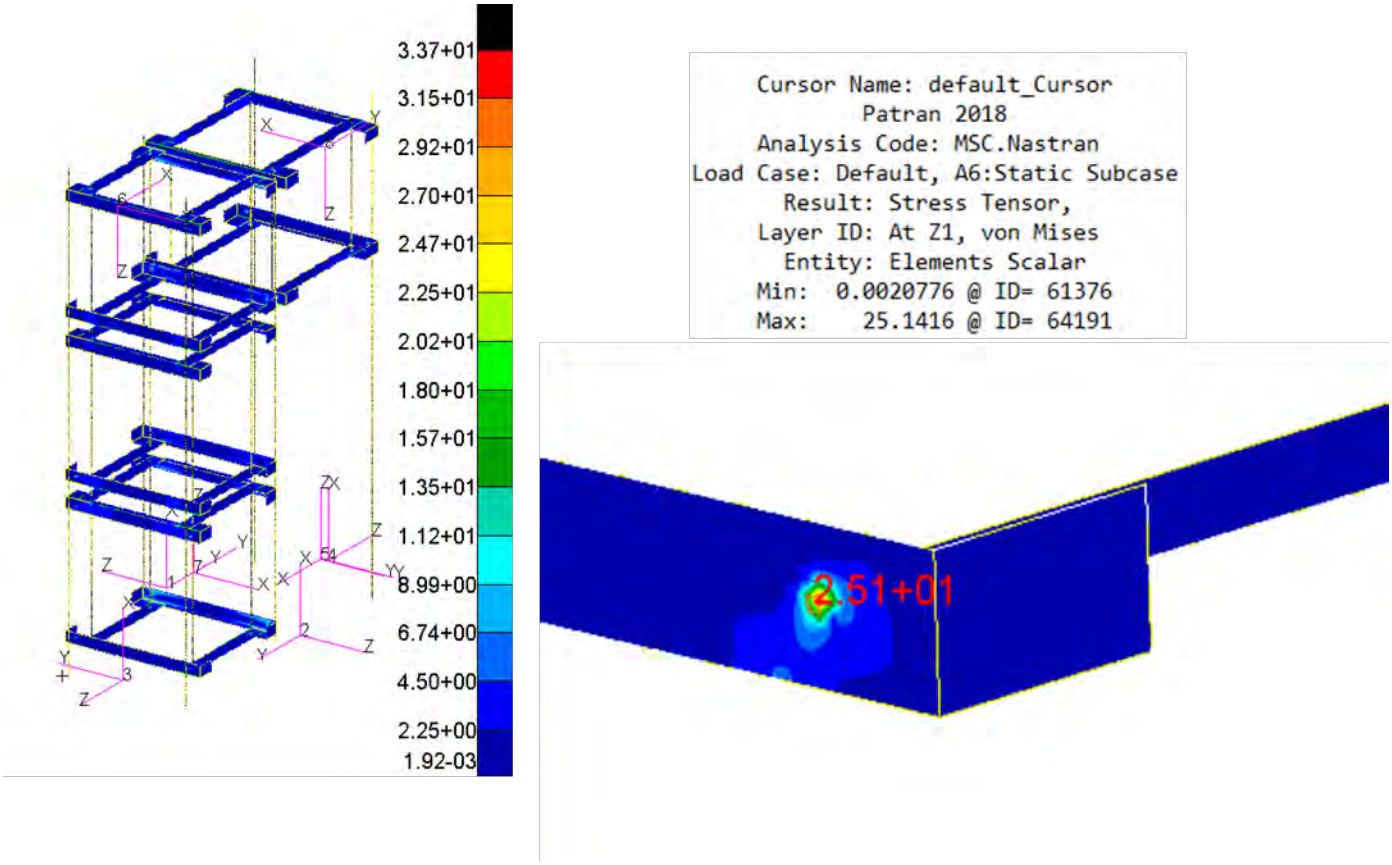


Figure 47: Von Mises Stresses [MPa] on Aluminum Decks (left) and Maximum von Mises Stress [MPa] Detail (right) of the 1st Case

The stresses in both the 1D Beam elements that discretize the intermediate rails and the 1D Bar elements that mesh threaded rods and main rails are also presented in Figure 48 and Figure 49 respectively. The maximum combined beam stress, which appears near the front-left RBE2 connection of the front intermediate rail and the left-second to top deck, equals to 7.40 MPa. Furthermore, the maximum combined bar stress is located in the bottom clamped corner of the back left main rail and has a magnitude of 35.34 MPa, which again can be considered small with regards to the Al 7075-T6 strength.

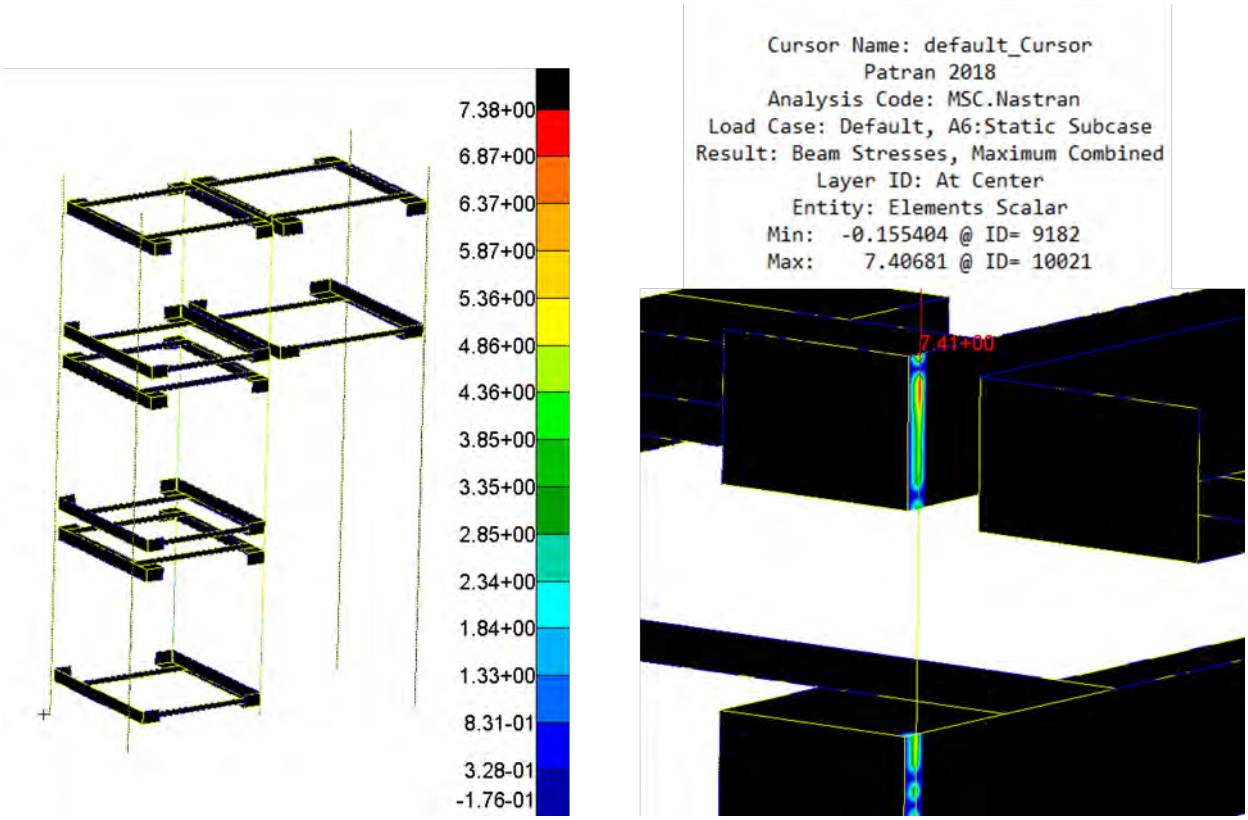


Figure 48: 1D Beam Elements (of intermediate rails) Stresses [MPa] (left) and Maximum Combined Beam Stress [MPa] Detail (right) of the 1st Case

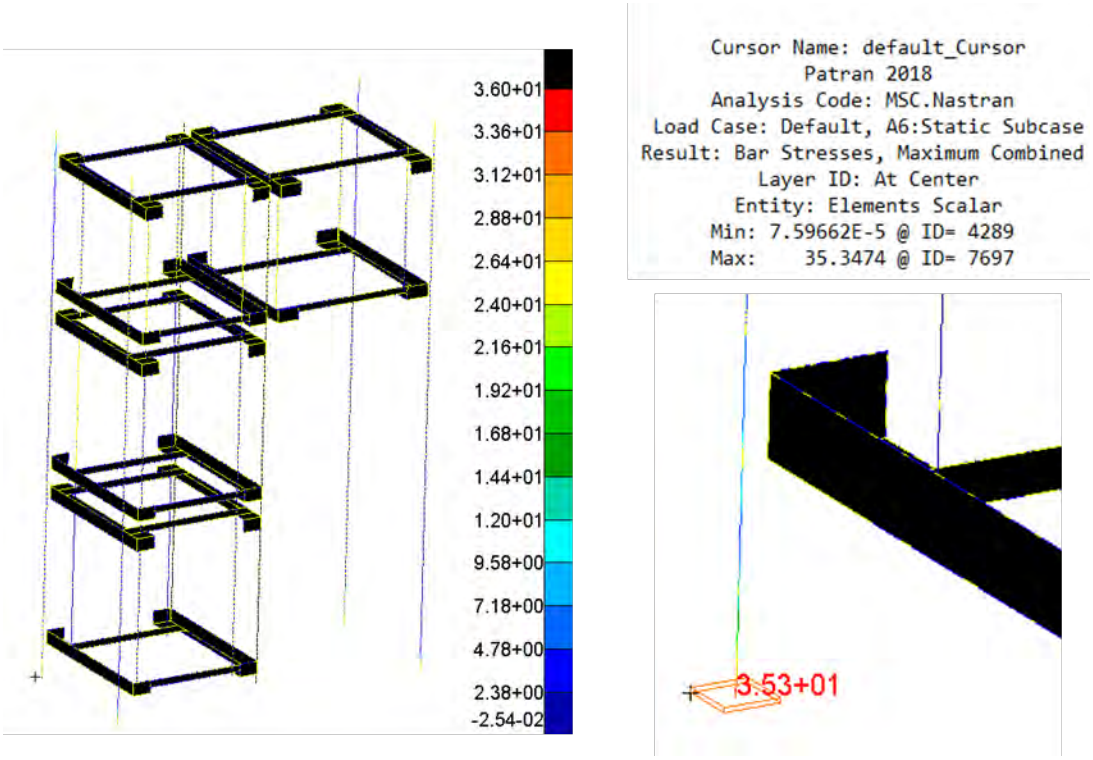
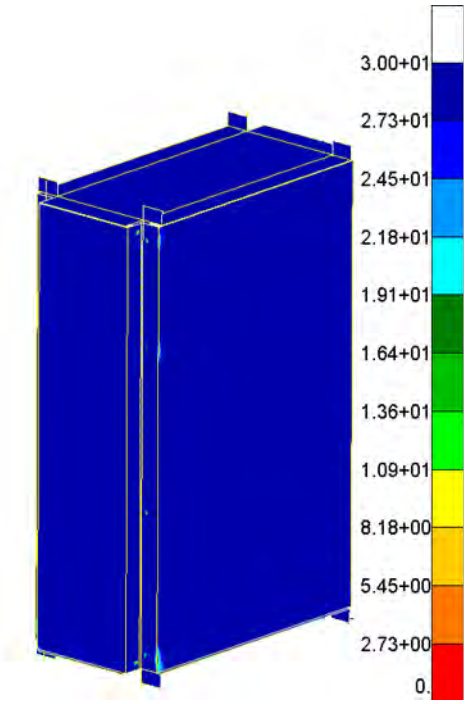


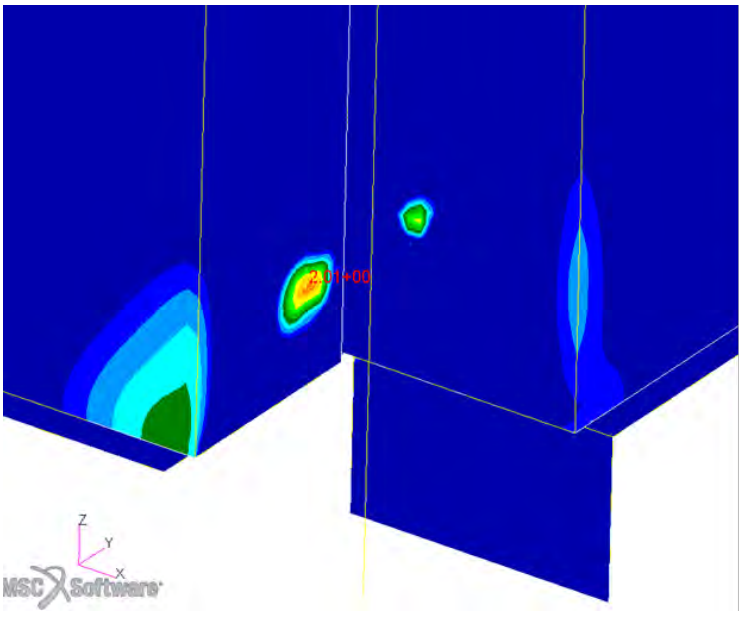
Figure 49: 1D Bar Elements (of main rails and threaded rods) Stresses [MPa] (left) and Maximum Combined Bar Stress [MPa] Detail (right) of the 1st Case

Undeniably, one of the most important pieces of information is gathered from the Figure 50 , which illustrates the worst MOS of the composite parts, according to the Tsai-WU-EPFS criterion. As initially expected, the worst MOS values are calculated near the bolted connections or closely to regions with abrupt changes in geometry. More specifically, as per Figure 51 the minimum margin of safety is presented on the 2nd layer, which tallies with a 45^0 orientated CFRP ply, and equals to a magnitude of 2.01. This value emerges from a finite element which locates in the nearby area of the first front RBE2 connection of the CubeSat's left side panel and is caused by the "curvature" along the X-axis that the 1D-BEAM elements of the front left rail have received.



Cursor Name: default_Cursor
Patran 2018
Analysis Code: MSC.Nastran
Load Case: Default, a6_Static Subcase
Result: Margins of Safety (Worst)*, TsaiWu Stress
Layer ID: (NON-LAYERED)
Entity: Elements Scalar
Min: 2.01031 @ ID= 132257
Max: 32181.8 @ ID= 118312

Figure 50: Worst Margins of Safety (MOS) of Composite Parts (Tsai-Wu-EPFS Criterion) of the 1st Case



Cursor Name: default_Cursor
Patran 2018
Analysis Code: MSC.Nastran
Load Case: Default, a6_Static Subcase
Result: Margins of Safety*, TsaiWu Stress
Layer ID: Layer 1002
Entity: Elements Scalar
Min: 2.01031 @ ID= 132257
Max: 105812. @ ID= 126765

Figure 51: Minimum Margin of Safety Detail of the 1st Case

3.5.2 2nd Quasi-static case with -30g inertial load on yy direction

Moving on to the 2nd quasi-static case, the 6U-XL CubeSat seems to have a maximum nodal displacement of 0.102 mm, which occurs on the bottom left area of the back (-X face) main panel. It is a fact that this value is 3 times smaller than the corresponding one of the 1st case and reveals that by means of stiffness, the satellite behaves better in this occasion.

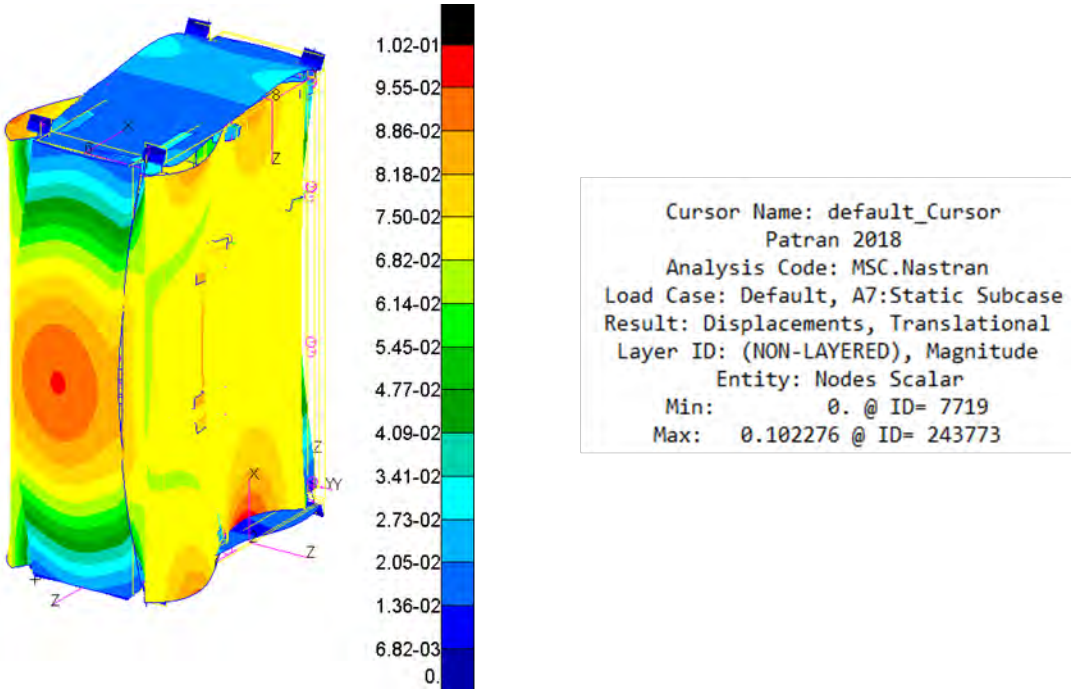


Figure 52: Displacement Distributions [mm] of the 2nd Case

At this point, it is important to note that Figure 52 presents a deformed shape of the structure in a modal scale using a scale factor of 0.1, fact that makes the resulting shape quite complex. Hence, Figure 53 is also included and shows the true scale of the deformed state, which confirms once again than the resulting displacement values are rather small and should not mislead the reader.

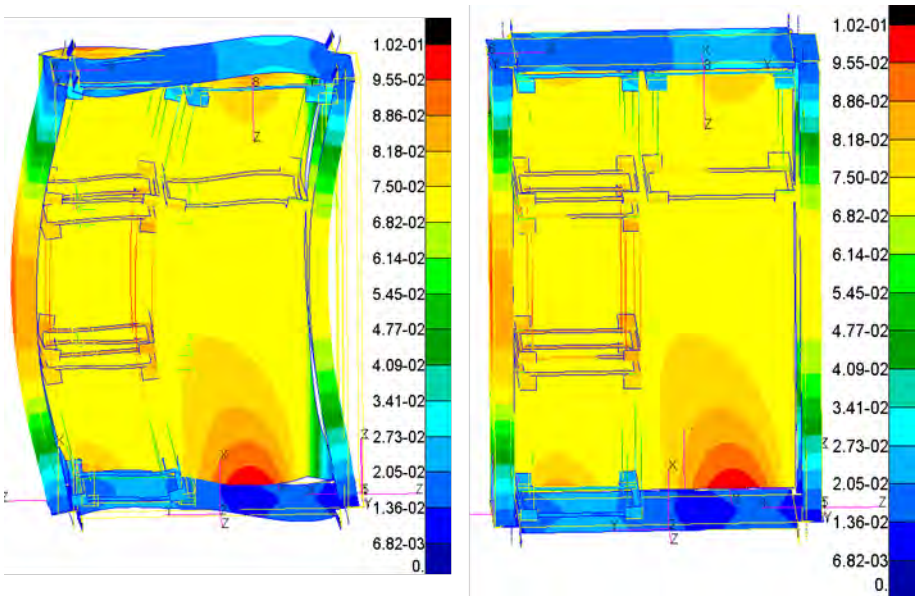


Figure 53: Side View of the Displacement Distributions [mm] of the 2nd Case – Model Scale with a Scale Factor of 0.1 (left) and True Scale (right)

In contrast to the 1st case and according to Figure 54, the maximum stresses and strains of the 2nd quasi-static loading seem to mainly occur near the connections between the main panels and the rails, which in fact are oriented along the direction of the present inertial load. However, as already mentioned, these nodal stresses are probably fictitious, hence some more reliable stress plots are required.

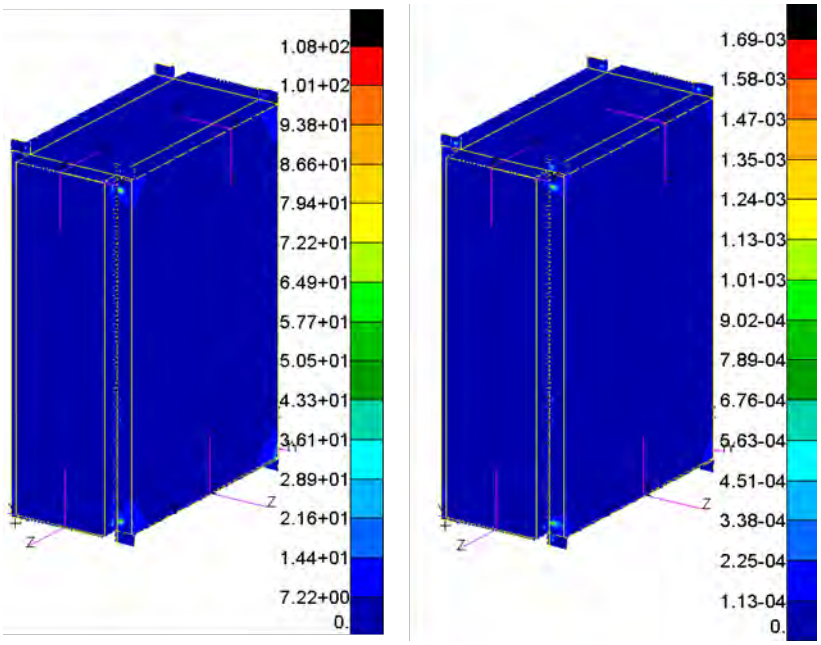


Figure 54: Max Principal Stresses [MPa] (left) and Max Principal Strains [-] Distributions (right) of the 2nd Case

Consequently, Figure 55, Figure 56 and Figure 57 show the element stresses of all the aluminum parts of the CubeSat arising during the 2nd quasi-static case. The maximum von Mises stress equals to 20.81 MPa and tends to occur in the close-up area of the back left RBE2 connection of the top left deck of the structure. As for the beam stresses, they are characterized by a maximum value of 4 MPa, which appears near the connection between the back-right surface of the second intermediate deck and the back intermediate rail. Moreover, the maximum bar stress approaches a value of 31.8 MPa and locates in the top clamped corner of the back right main rail. As it easy to observe, all the above stress values are smaller than the corresponding stresses of the 1st case, a fact that testifies a more acceptable behavior in terms of the aluminum parts strength for the 2nd quasi-static instance.

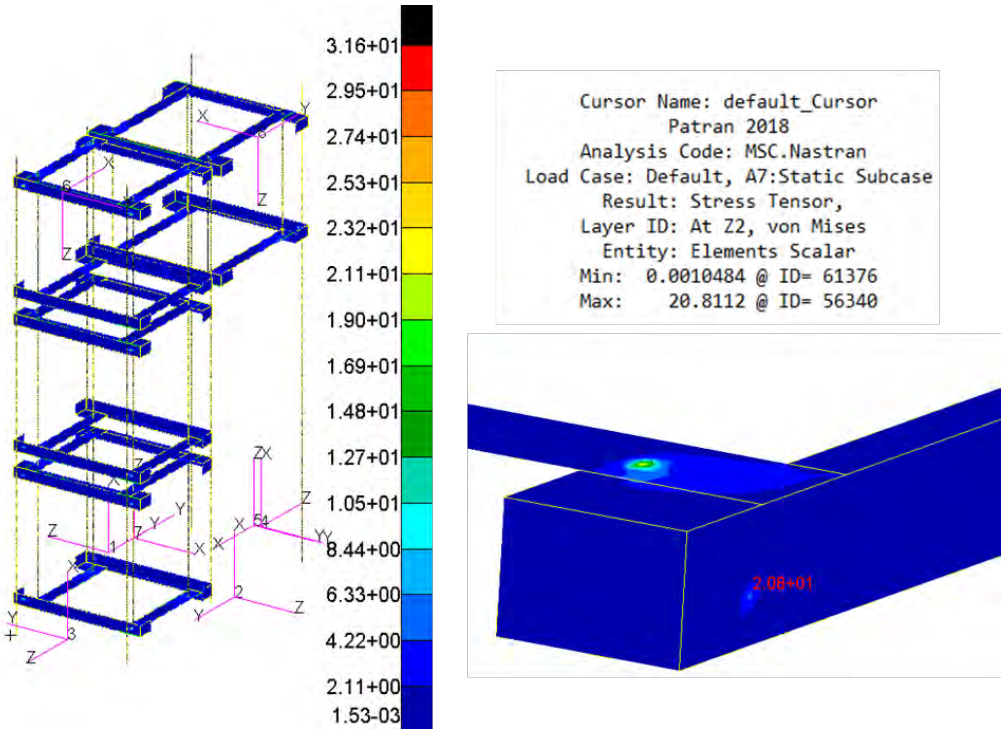


Figure 55: Von Mises Stresses [MPa] on Aluminum Decks (left) and Maximum von Mises Stress [MPa] Detail (right) of the 2nd Case

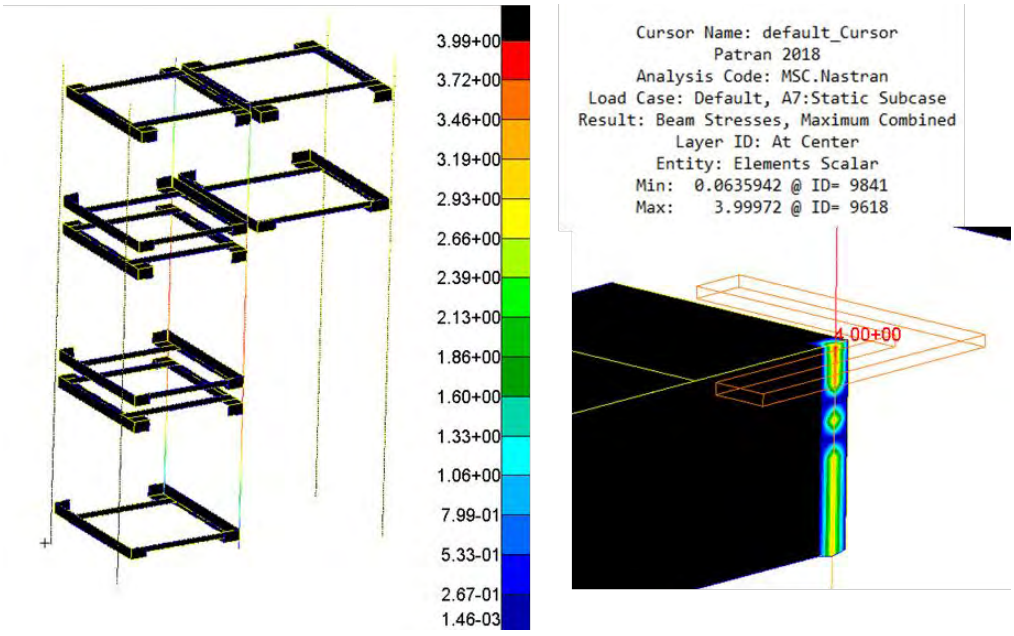


Figure 56: 1D Beam Elements (of intermediate rails) Stresses [MPa] (left) and Maximum Combined Beam Stress [MPa] Detail (right) of the 2nd Case

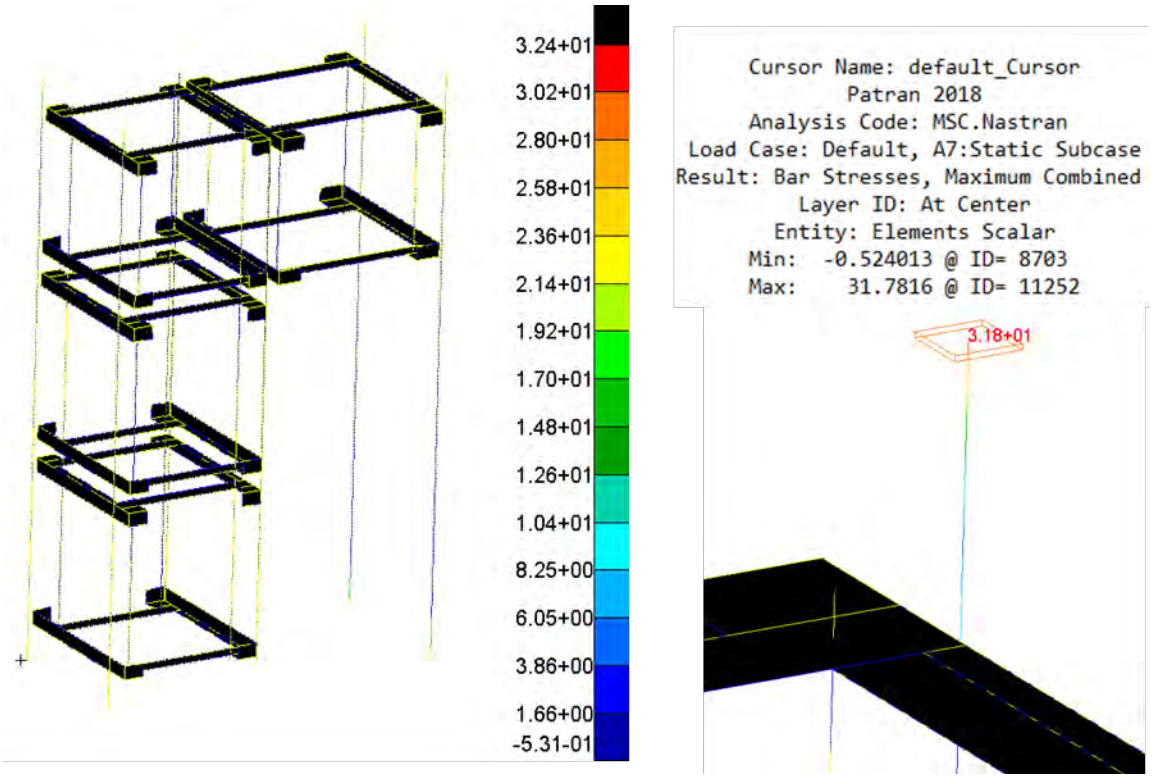


Figure 57: 1D Bar Elements (of main rails and threaded rods) Stresses [MPa] (left) and Maximum Combined Bar Stress [MPa] Detail (right) of the 2nd Case

Last but definitely not least are the MOS distributions that are illustrated in Figure 58, which shows that the most critical areas appear to be close to the connections between the main panels and the rails. More particularly, the minimum MOS is clearly displayed, as per Figure 59, in the bottom left RBE2 connection of the front main panel and more specifically in the penultimate layer, which agrees again with a 45^0 orientated CFRP ply. This MOS equals with 1.65, which on the one hand ensures the safety of the structure, while on the other hand indicates that during this loading, the composite parts present a more intense stress field, giving a significantly reduced safety factor, compared to the 1st quasi-static case.

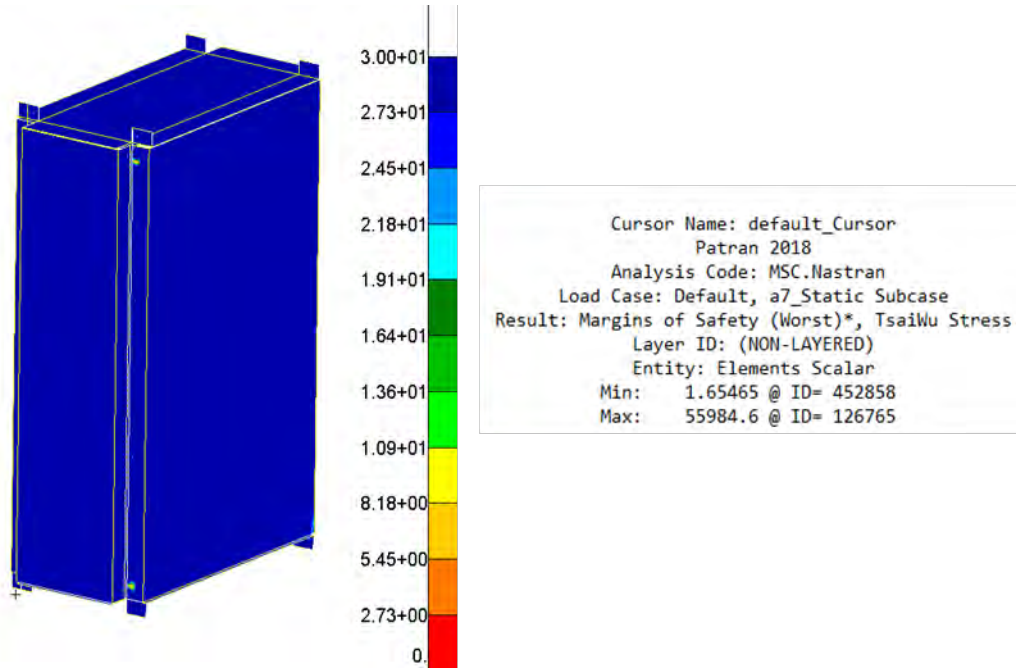


Figure 58: Worst Margins of Safety (MOS) of Composite Parts (Tsai-Wu-EPFS Criterion) of the 2nd Case



Figure 59: Minimum Margin of Safety Detail of the 2nd Case

3.5.3 3rd Quasi-static case with -30g inertial load on zz direction

Based on Figure 60, it becomes noticeable that the maximum displacement of the 3rd quasi-static case has a magnitude of 0.344 mm and is developed in the middle front face of the bottom base. As it is visible from the internal view, the main components that are displaced are the decks, whose connections drag both bases and as a result the maximum displacement was expected in one of them. Regarding the peak value, it approaches the corresponding max of the 1st case and can be rated as moderately small.

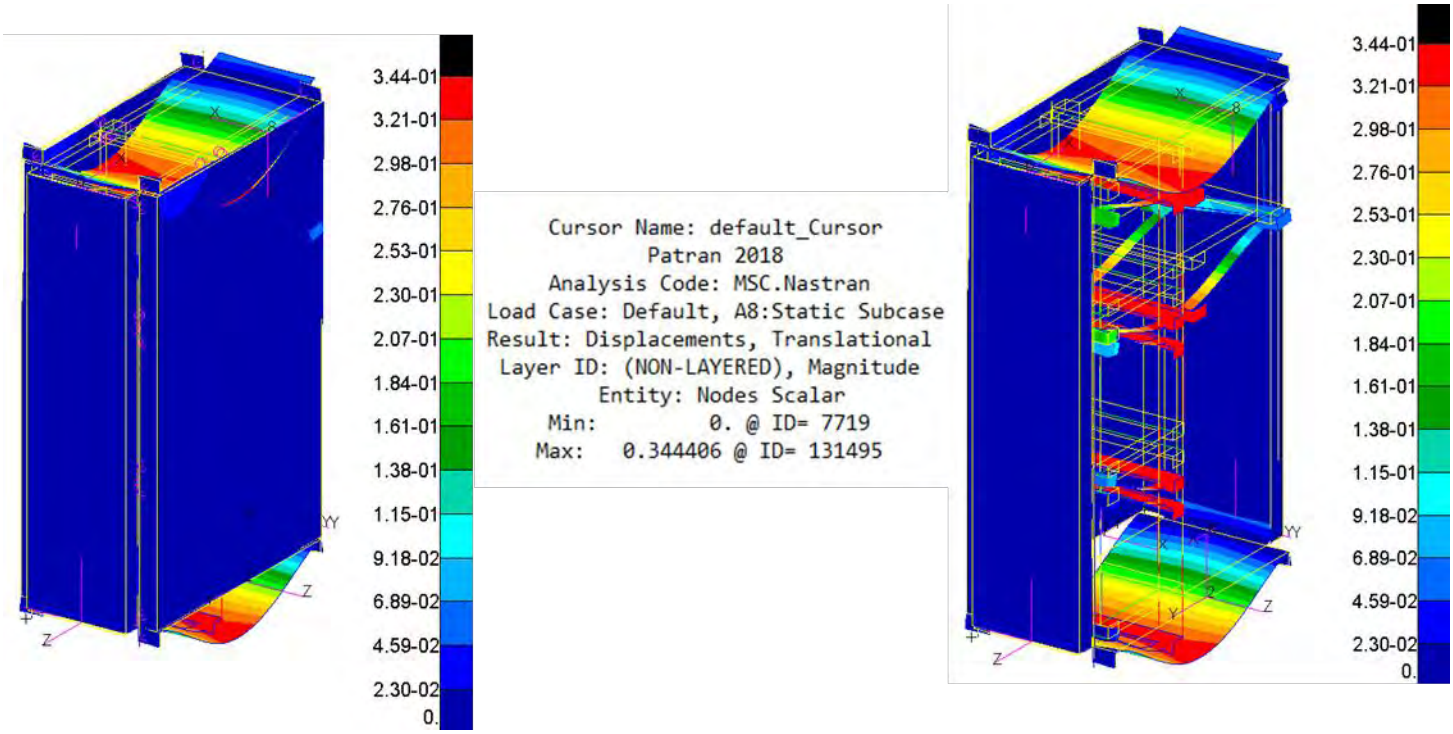


Figure 60: Displacement Distributions [mm] on the Entire Model (left) and Internal View (right) of the 3rd Case

Regarding the maximum principal stresses and strains, they are mainly located on the connections between both main panels and bases with the rails. Furthermore, as it can be observed from Figure 61, bases have a more intense stress field in comparison to the previous cases, due to their extensive interaction with the aluminum decks, which because of this specific loading condition, tend to move along their “weak” axis.

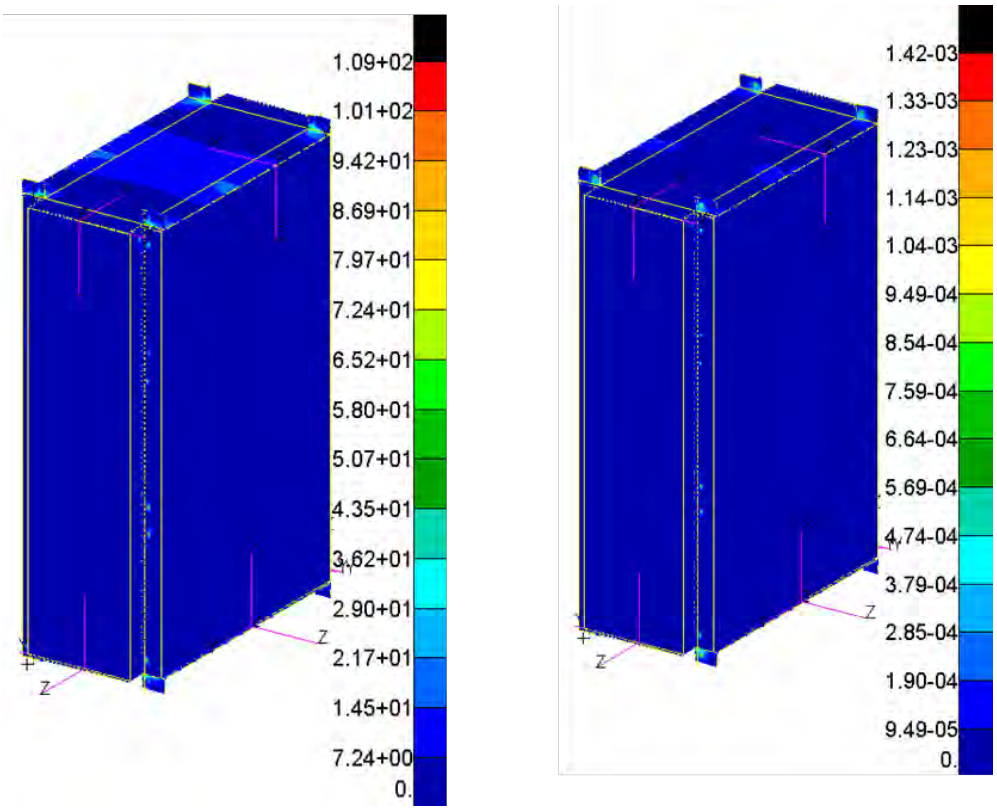


Figure 61: Max Principal Stresses [MPa] (left) and Max Principal Strains [-] Distributions (right) of the 3rd Case

Subsequently, Figure 62, Figure 63 and Figure 64 demonstrate the element stresses of all the aluminum parts emerging during the 3rd quasi-static case. Respecting aluminum decks, the maximum von Mises stress arises to 101.84 MPa and is displayed on the back left fastening between the top intermediate deck and the matching threaded rod. This stress reaches much higher levels in comparison with the other cases an constitutes the worst-case scenario for the aluminum decks. Despite its great increase, this stress value remains about 5 times below the yield limit of aluminum and can be considered as absolutely acceptable. As for the beam elements, they have a maximum stress value of 2.64 MPa which occurs in the same area as the corresponding one of the 2nd case. Moreover, the maximum bar stress reaches a value of 25.66 MPa, which is presented in the top clamped corner of the back left main rail and can also be reviewed as negligible.

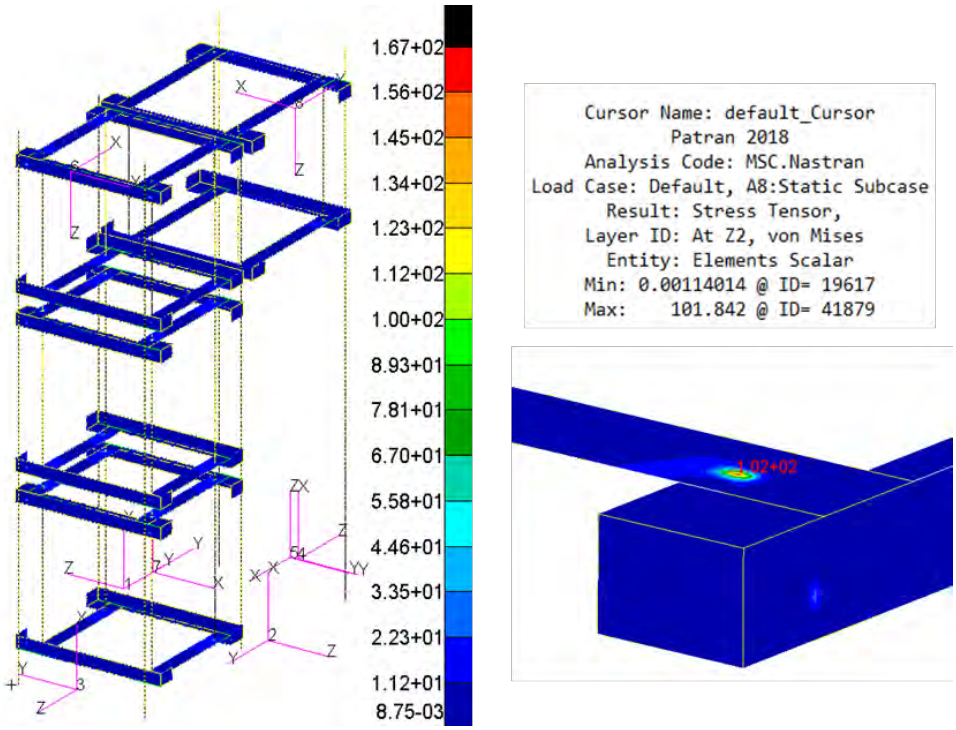


Figure 62: Von Mises Stresses [MPa] on Aluminum Decks (left) and Maximum von Mises Stress [MPa] Detail (right) of the 3rd Case

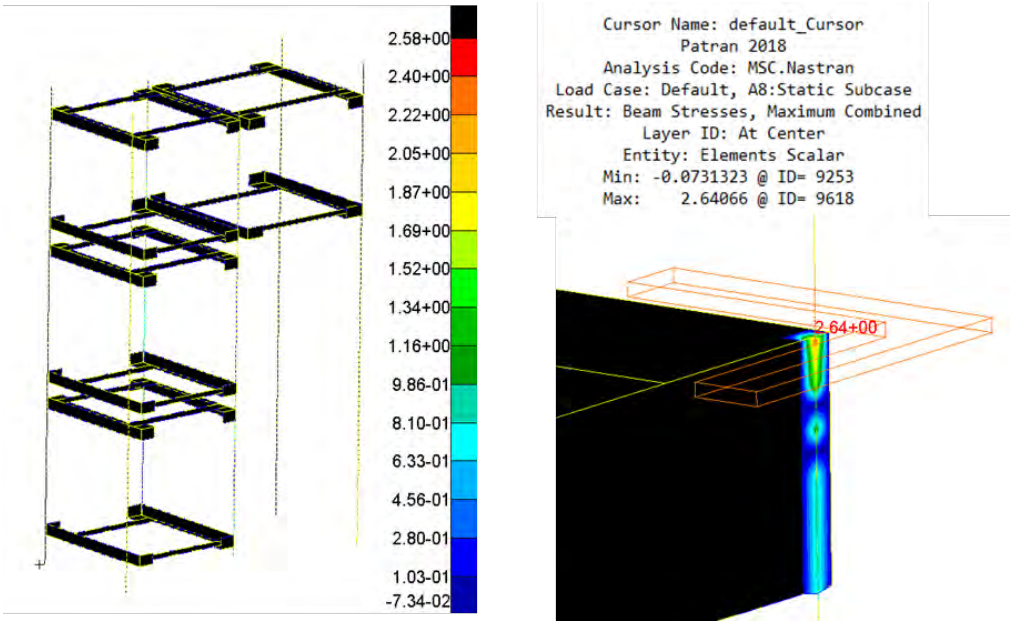


Figure 63: 1D Beam Elements (of intermediate rails) Stresses [MPa] (left) and Maximum Combined Beam Stress [MPa] Detail (right) of 3rd Case

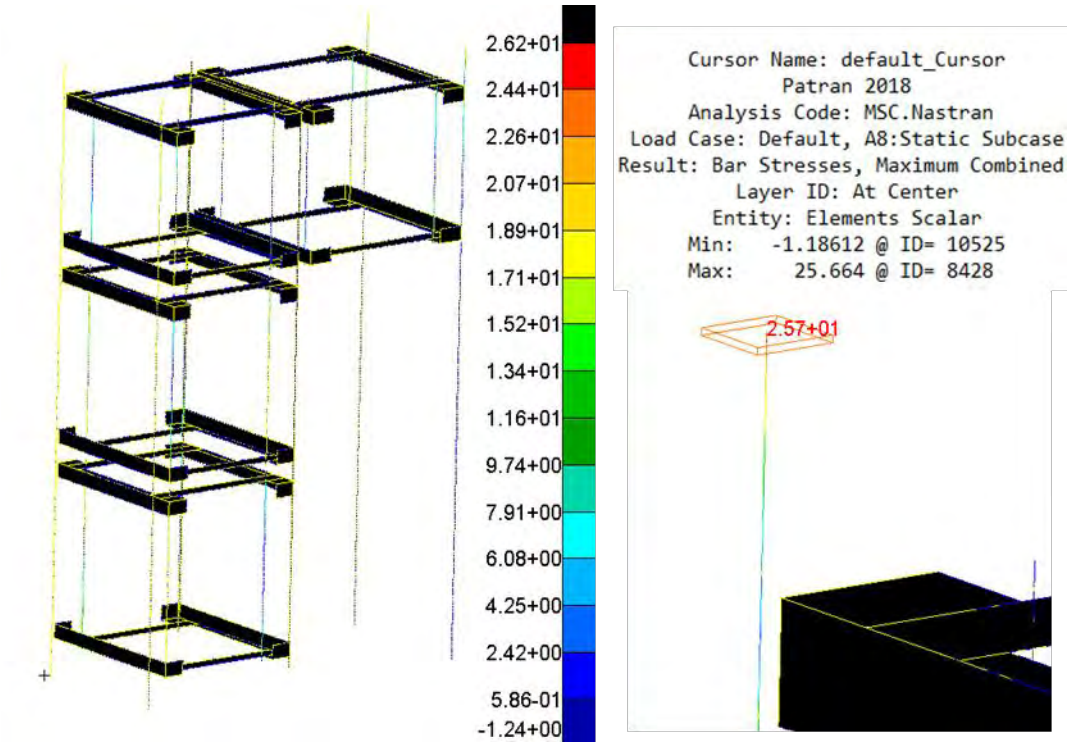


Figure 64: 1D Bar Elements (of main rails and threaded rods) Stresses [MPa] (left) and Maximum Combined Bar Stress [MPa] Detail (right) of the 3rd Case

Finally, the worst MOS distributions of this scenario are shown in Figure 65, which indicates that the critical areas of the composite parts appear to locate not only near the bolted connections of both main panels and bases, but also close to the base's flanges, that are characterized by an abrupt geometry change. According to Figure 66, the worst MOS equals to 2.28 and is presented on the penultimate layer of the lamination, which corresponds again to a 45^{o} oriented CFRP ply. More accurately, it is detected on the 3rd from the bottom RBE2 connection of the front main panel's left side. It is a fact that the above MOS reveals the best-case scenario for the composite parts and is owned to the fact that the external loads of this particular case are mainly received by the aluminum decks, hence allowing composite parts to reach higher safety zones.

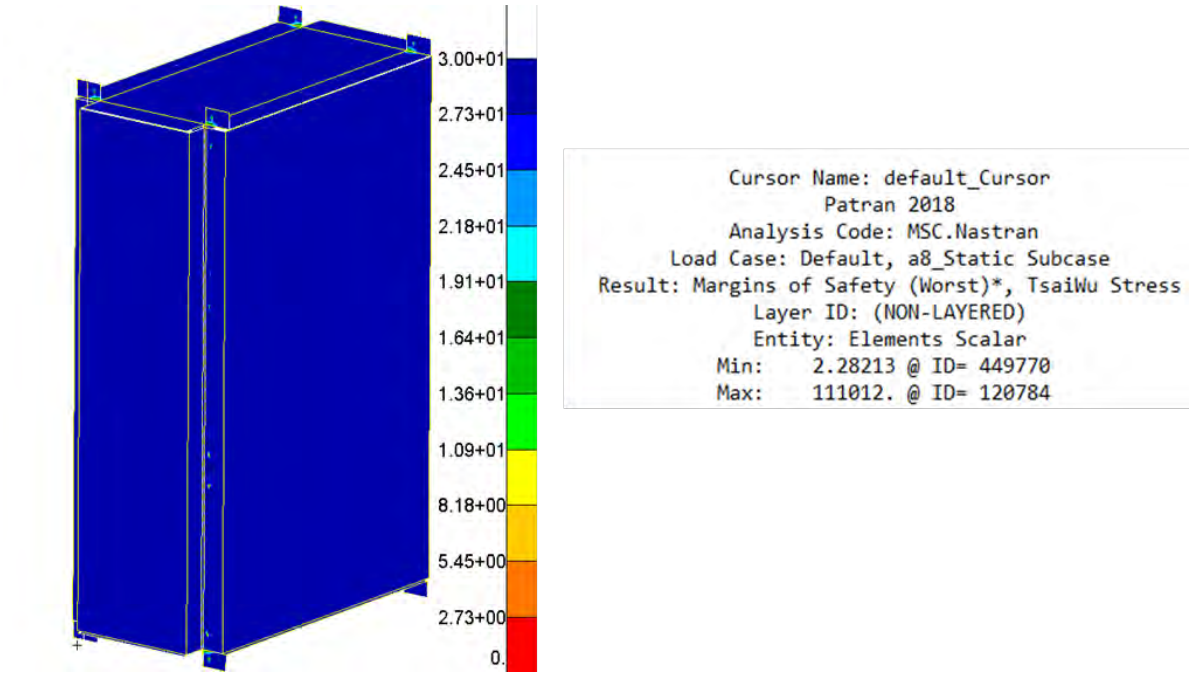


Figure 65: Worst Margins of Safety (MOS) of Composite Parts (Tsai-Wu-EPFS Criterion) of the 3rd Case

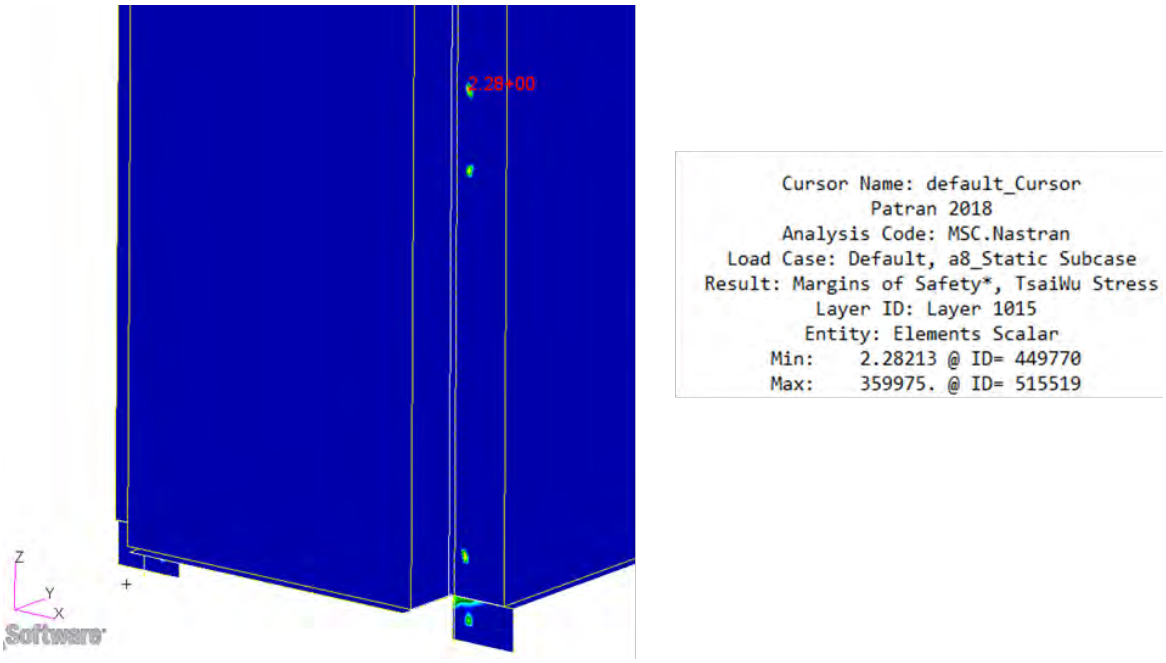


Figure 66: Minimum Margin of Safety Detail of the 3rd Case

3.5.4 Conclusions of the Quasi-static Analyses

Summarizing, despite the simplifications of the computational model and especially the lack of modelling threaded holes, which are areas of stress concentrations, the extracted results are reasonable and reflect reality to a significant extent. The substantially acceptable maximum stresses, comparing to the strength of all materials, and low displacements, as well as the considerably high values obtained for the MOS of the composite panels in all cases, bring a fair degree of confidence in the original structure's design. Hence, the CubeSat chassis and therefore the entire system, can be considered adequately robust.

According to Table 6, in all cases bar and beam stresses are very low, thus these elements have the highest safety margins. Also, all the MPC forces, that were calculated but not presented, arrive at very low levels, with the result that the stainless steel Φ3 bolts can easily carry and transfer the loads, without failing. As for the aluminum decks, besides the 3rd case that was appropriately commented in the previous subchapter, both the 1st and the 2nd case-scenarios, reach insignificant peaks of von Mises stress and no warnings are raised. Regarding the composite components, it is noticed that in every case an "outer", concerning the laminate's midplane, 45^{o} ply is closest to failure, in accordance with the FPF-approach. It is a fact that 45^{o} plies are found, in the literature [44], to be crucial in determining the joint bearing strength and the occurrence of the shear-out joint failure. The worst-case scenario referred to the composite parts is the 2nd quasi-static analysis, in which the composite panel develops a MOS = 1.655. By associating this value, with the corresponding strength ratio (SR = 2.655), one can easily conclude that the allowable strength is approximately 2.6 times above the maximum calculated one. Thus, even in the worst scenario, the safety of the structure is totally ensured, while it is also realized that the CubeSat could withstand much greater inertial loads, which could reach 78g.

After further investigation, one could claim that the 1st quasi-static analysis is the best possible scenario, as it combines great safety both in aluminum and composite components, comparing to the other cases. However, through a comparison between the worst safety margins of all parts, it is concluded that the most critical components, which will fail first, in every case, are the composite ones. Hence, the best-case scenario, that also reveals the most preferable placement of the CubeSat inside the POD, is the one at which the external loads are applied along the Z-axis, while the worst is along the Y-axis.

Table 6: Quasi-Static Analyses Results (All Cases)

Quasi-Static Analyses			
	X-Axis	Y-Axis	Z-Axis
Displacement [mm]	0.35	0.102	0.344
Stress – decks (von Mises) [MPa]	25.142	20.811	101.842
Stress – intermediate rails [MPa]	7.4068	4	2.640
Stress – rails and threaded rods [MPa]	35.347	31.78	25.664
MOS – CFRP (Tsai-Wu-EPFS)	2.01	1.655	2.282
Worst Safety Margins – aluminum parts	14.23	15.82	4.94
Worst Safety Margins - CFRP	3.01	2.655	3.282
Best case scenario Moderate case scenario Worst case scenario			

3.6 Buckling Analysis

In linear static analysis, a structure is normally assumed to be in a state of stable equilibrium. However, under certain loading conditions the mechanical system may become unstable, and the structure continues to deflect without an increase in the magnitude of the applied loads. This phenomenon is commonly known as buckling or structural instability and usually occurs when slender elements under high compression suddenly collapse. The instantaneous nature of this failure mode makes it very deceptive and dangerous.

Nevertheless, some design measures can be taken to avoid that loss of structural stability, which mainly depends on the element length, stiffness in geometry and elasticity of the materials. An important concept in the context is the critical buckling load, which shows the maximum compressive load in the axial direction that the structure can resist before collapsing due to buckling. In order to quantify the above limit, the idea of the buckling load factor (BLF or also represented as λ) is introduced and described in Table 7 [45]. In general, this coefficient indicates the number by which the reference load must be multiplied in order to reach the critical buckling load.

Table 7: Interpretation of the Buckling Load Factor (BLF)

BLF Value	Buckling Status	Remarks
> 1	Buckling not predicted	The applied loads are less than the estimated critical loads.
$= 1$	Buckling predicted	The applied loads are exactly equal to the critical loads.
< 1	Buckling predicted	The applied loads exceed the estimated critical loads.
$-1 < BLF < 0$	Buckling possible	Buckling is expected if the load directions are reversed.
$= -1$	Buckling possible	Buckling is expected if the load directions are reversed.
< -1	Buckling not predicted	The applied loads are less than the estimated critical loads, even if their directions are reversed.

It is noteworthy to mention that in this thesis, only linear buckling analysis is considered, which assumes that there is no yielding of the materials and the direction of the applied forces do not change. Hence, buckling can be expressed as a linear eigenvalue problem :

$$([K] - \lambda[G])\{\delta_b\} = \{0\} \quad (40)$$

, where *[K]* and *[G]* are the system stiffness and geometric matrices respectively, λ is the buckling load factor and $\{\delta_b\}$ is the eigenvector, which contains real numbers and expresses the buckling mode shapes. The above eigenvalue problem is solved using the Lanczos method and only the lowest eigenvalue (BLF) is extracted for every one of the three case loadings presented previously, which is directly associated with the buckling load as :

$$F_{cr} = \lambda_{cr} F_{ref} \quad (41)$$

In other words,

$$\lambda_{cr} = \frac{F_{cr}}{F_{ref}} \quad (42)$$

Firstly, the stability of the CubeSat will be checked during the 1st load case, which is characterized by a -30g inertial load along the X-axis. According to Figure 67, the structure leads to collapse when the BLF equals to λ = -29.375, meaning that it can withstand loads of the order of 881g without failing in buckling, while the first buckling eigen-mode of this case presents an extremum at the center of the rear main panel.

As for the 2nd load case, based on the Figure 68, a BLF = -74.661 is calculated, while the maximum eigen-mode value is located on the center of the left side panel of the satellite. In closing, during the 3rd load case a factor of BLF = 16.953 is calculated (Figure 69) and the eigen-mode shape displays a maximum on the bottom front-left threaded rod of the 1st "imaginary 1U system" (Figure 70).

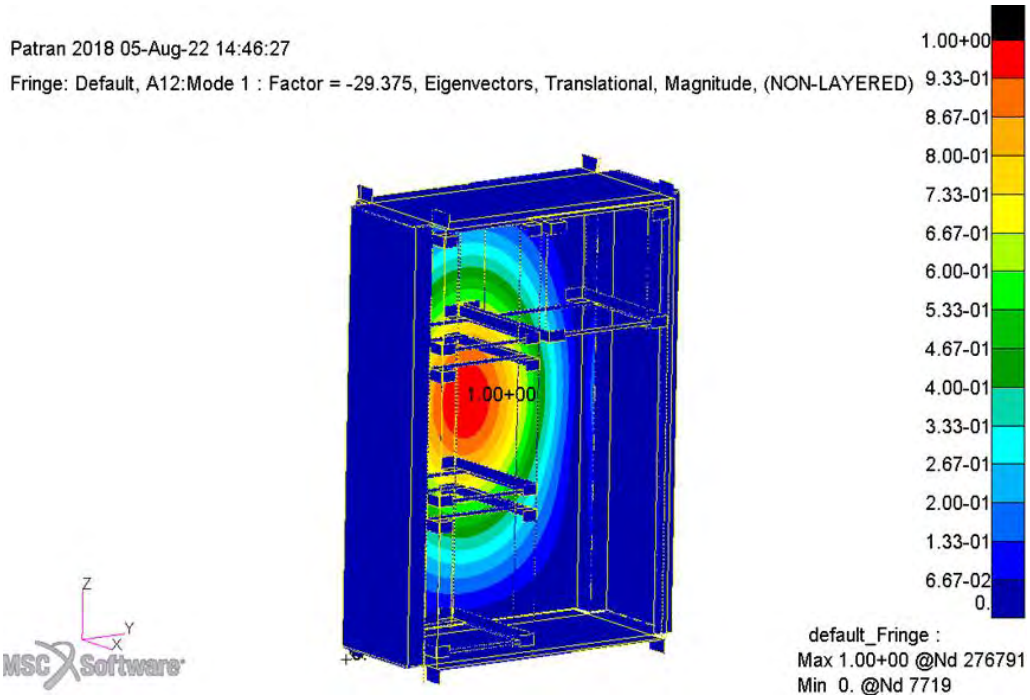


Figure 67: BLF and First Buckling Eigen-Mode Shape of the 1st Load Case

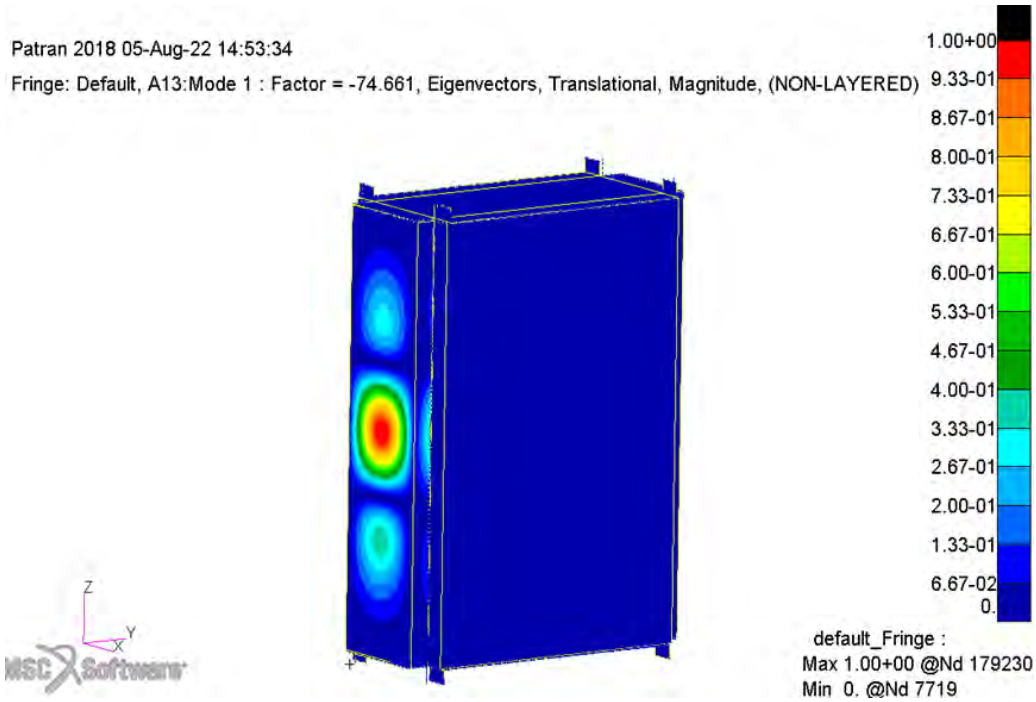


Figure 68: BLF and First Buckling Eigen-Mode Shape of the 2nd Load Case



Figure 69: BLF and First Buckling Eigen-Mode Shape of the 3rd Load Case

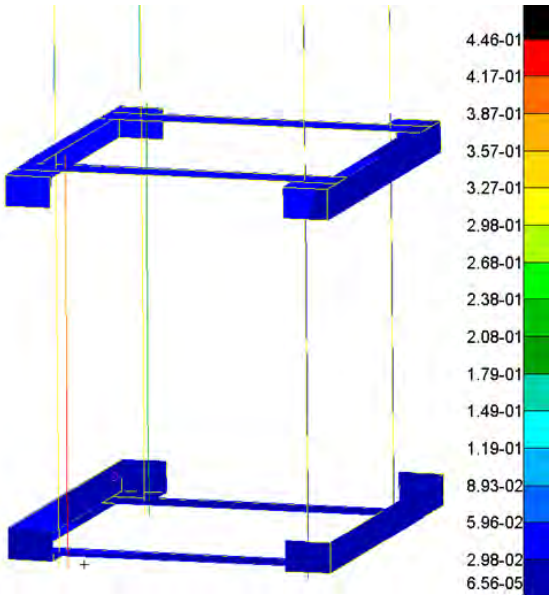


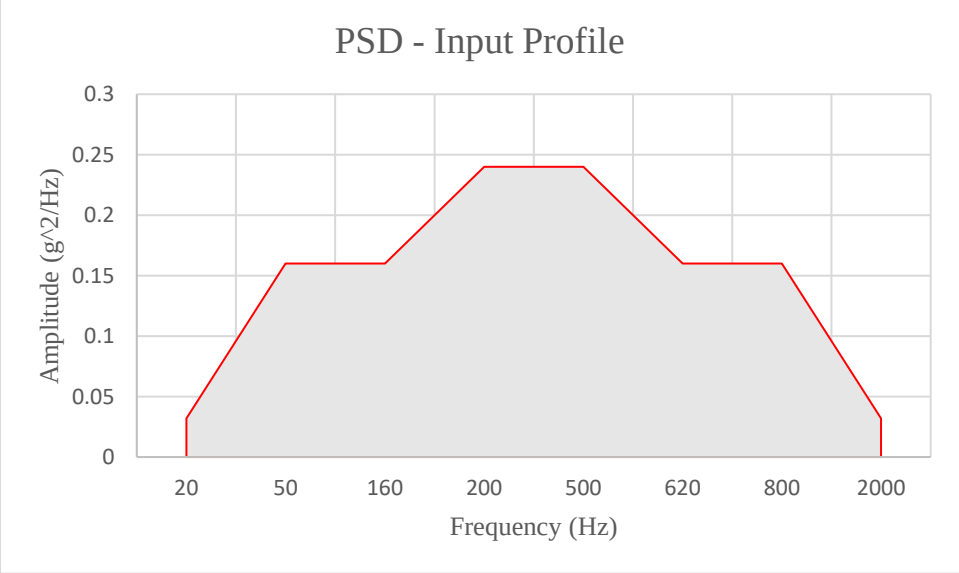
Figure 70: First Buckling Eigen-Mode Shape Detail of the 3rd Load Case

Undeniably, all the buckling analyses clearly indicate through their high values of BLFs that the present CubeSat will not be led to a possible loss of its stability. Worth noting is the fact that in the worst buckling's case scenario (3rd load case) the structure has the ability to withstand gravitational loads up to 507g while in the best scenario (2nd load case) this value tends to equal with 2220g. These unrealistically extreme inertial loads demonstrate very high safety margins in terms of buckling, fact that was expected also empirically due to the small size of the satellite. Hence, most theses, with similar topics, do not deal with buckling analyses at all.

Thus, one easily concludes that the structure will fail first due to either passing the strength limits of composite parts or reaching to a possible resonance condition with the POD. After a further investigation, it is perceived that the quasi-static results are more conservative than the modal ones, as they consider extra safety factors, which were discussed in a previous sub-chapter. Consequently, the modal behavior and more accurately the fundamental frequency define the critical failure mode of the present CubeSat.

3.7 Random Vibration (PSD)

In many applications, the external loading profile is not known in a deterministic sense, and instead it is quantified in a statistical sense with properties such as the mean load and the standard deviation of load [46]. Such loadings are known as random or stochastic loads. It should be expected that the response of a structure will also be random in nature, hence analysis methods that determine the statistical properties of its behavior are appropriate. The most common approach for random analysis uses the Power Spectral Density (PSD) functions, which describe how the variance of a time series is distributed with frequency. A launch of a spacecraft consists in a series of events, each of which has several independent sources of loads for the launch vehicle and payload. One of them is the high-frequency random vibration environment, which typically has significant energy in the frequency range from 20 Hz to 2000 Hz, transmitted from the launch vehicle to the payload. For the current mission the input of the PSD profile is shown in Figure 71.



Frequency (Hz)	PSD (g^2/Hz)
20	0.032
50 - 160	0.16
200 - 500	0.24
620 - 800	0.16
2000	0.032

Figure 71: Random Vibration Input

The square root of the area under the PSD curve gives the acceleration root mean square value (Grms), which is a qualitative measure of intensity of vibration. Random vibration limit loads are typically

taken as the "3-sigma load" (obtained by multiplying the rms load by 3) [47], while to avoid unrealistic deformations, a structural damping is applied to the entirety of the model, using a fairly typical 0.02 value [48]. As was the case with the Static analysis presented prior, the Random Vibration analysis is run in all three major directions, to ensure that the satellite can withstand the typical vibrations felt during launch, regardless of its position relative to the launcher vehicle itself. However, it is important to note that, in contrast to the quasi-static 30g load, an inertial load with the magnitude of 9.81 m/s^2 (= 1g) is applied in the negative axis direction, according to each simulation's main axis. This typical load serves as an orientation and an extra multiplicative factor, seeing as the PSD input is presented in g's (units of acceleration) [38].

The Random Vibration analysis requires a Frequency Response to be run beforehand, forcing a deck of excitation frequencies to be chosen. Due to limited capabilities of the available computer, the above deck consists of 30 desired roots (frequencies), which are calculated according to the Lanczos Method. Since the structure naturally deforms to larger degrees closer to the natural frequencies obtained from the normal modes analysis, the choice ends up falling on these, to an extent, with a couple of extra frequencies around each of them also applied to ensure that the behavior close to resonance is also taken into account.

In the Figures 72-74, the output response of the entire system, in terms of acceleration, is plotted for all the three loading scenarios. It is important to note that in the X- and Y-Axis loading cases, the response of the central node of each CFRP face was monitored. As for the Z-Axis case, the response of the central node of each composite base, as well as the response of every aluminum deck, that are intended to carry all the appropriate PCBs, are presented in Figure 74. Moreover, in the Z-Axis case, the displacement output for the aforementioned components is also illustrated in Figure 75. It should be underlined that for every loading case, the behavior of each node (in terms of acceleration or displacement) is checked in the direction of the corresponding inertial load, meaning that in the X-Axis case, for example , the X-component of the total acceleration output is plotted.

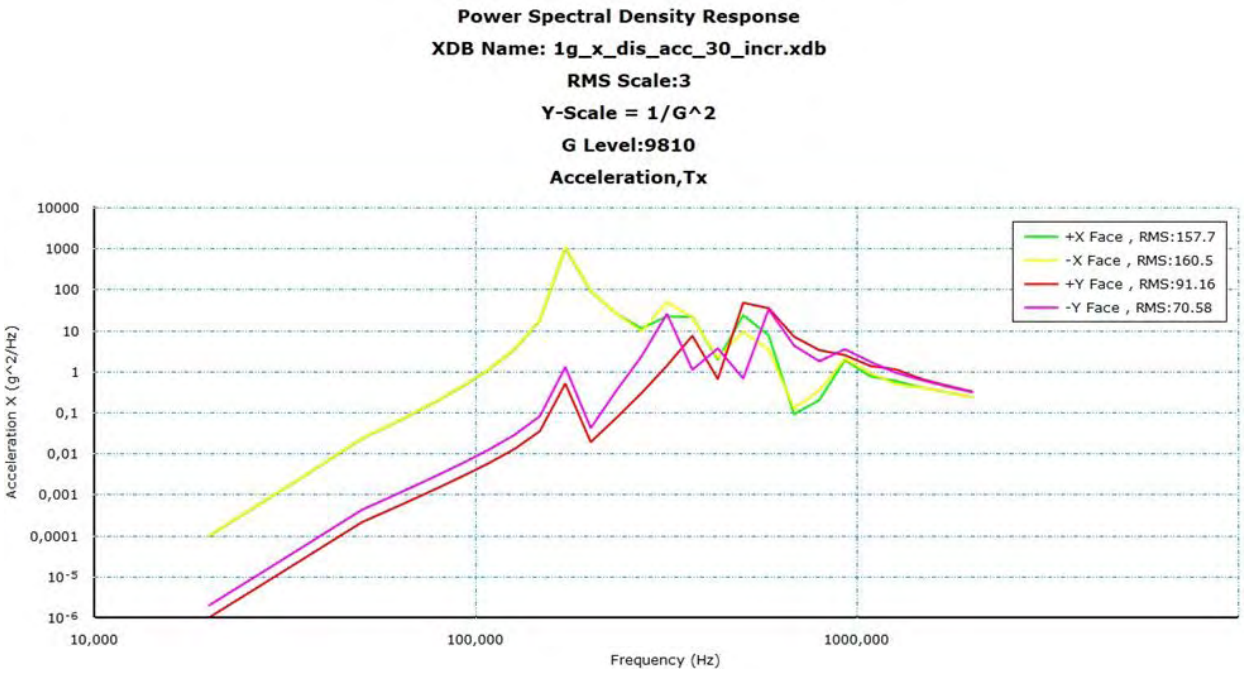


Figure 72: PSD (X-Axis) Results

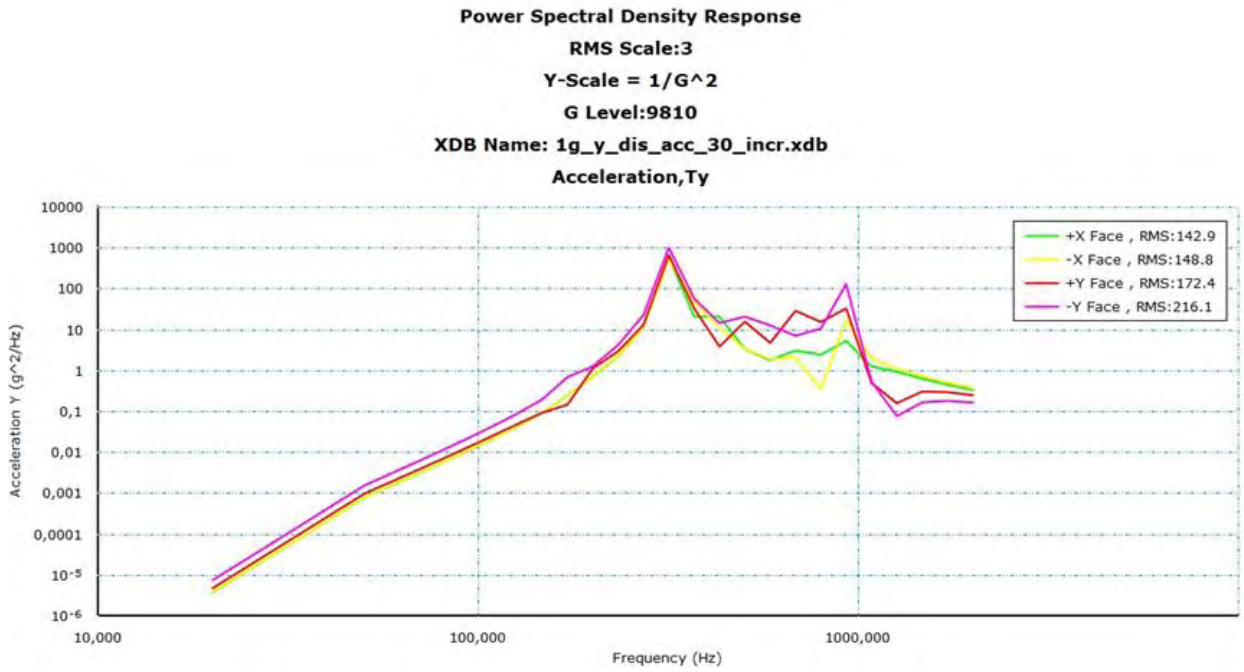


Figure 73: PSD (Y-Axis) Results

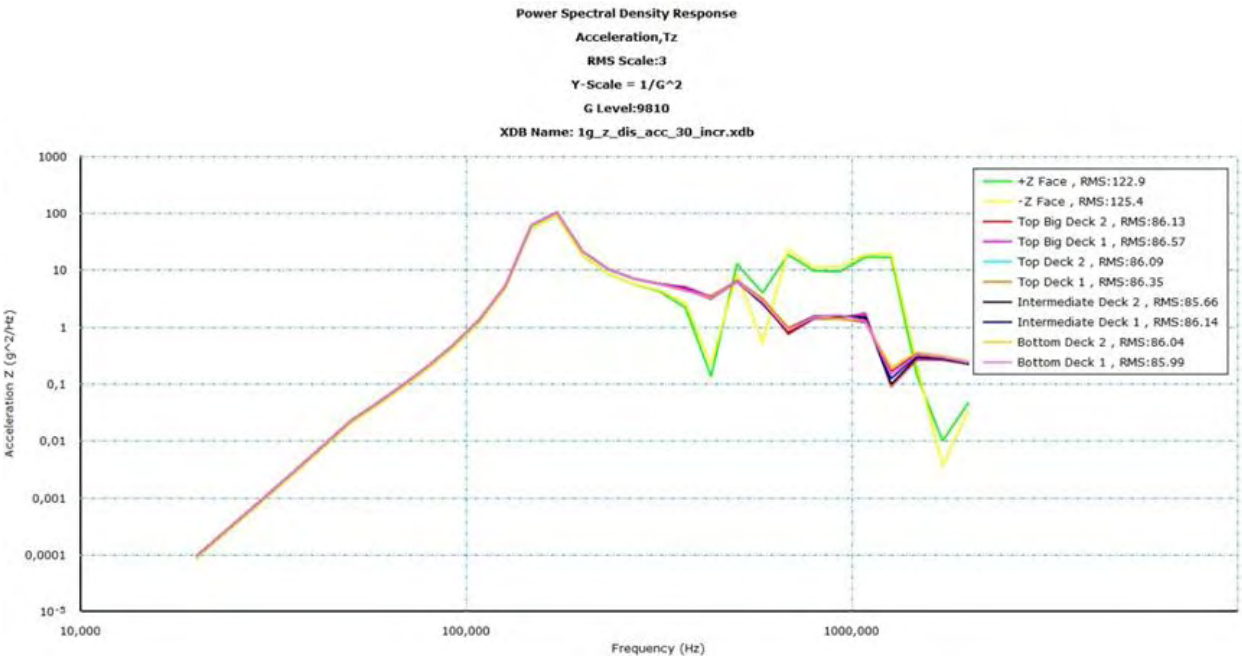


Figure 74: PSD (Z-Axis) Results



Figure 75: Displacement Output for the Z-Axis Loading Case

It is easily observed that in the X-Axis and the Z-Axis loading scenarios, there is a resonance close to 150 Hz (logarithmic scale), hence peaks are presented on the response of each component. This behavior was actually expected, as the normal modes analysis testified that the fundamental frequency of the system is 159.16 Hz and that the most crucial, in terms of vibrational behavior, components are the aluminum decks, the composite bases and the main panels. On the contrary, side panels seem to reach a state of resonance at higher frequencies, as observed from Figure 72 and mainly from Figure 73.

As far as the displacements are concerned, according to Figure 75, the resonance of all the internal components close to 150 Hz becomes, once again, apparent, however for a greater inspection of the displacement outputs, appropriate RMS analyses are carried out, the results of which are illustrated in the following images, for each of the loading cases.

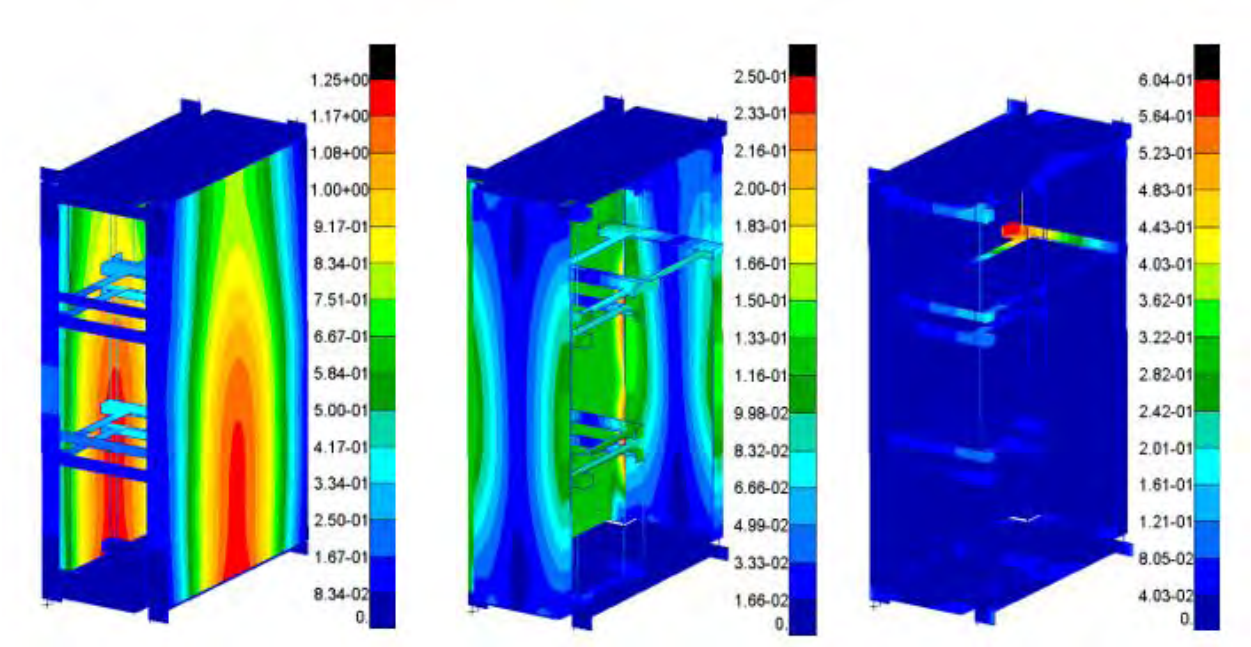


Figure 76: RMS Displacements [mm] for the X-Axis Loading Case (X-Component [left], Y-Component [middle], Z-Component [right])

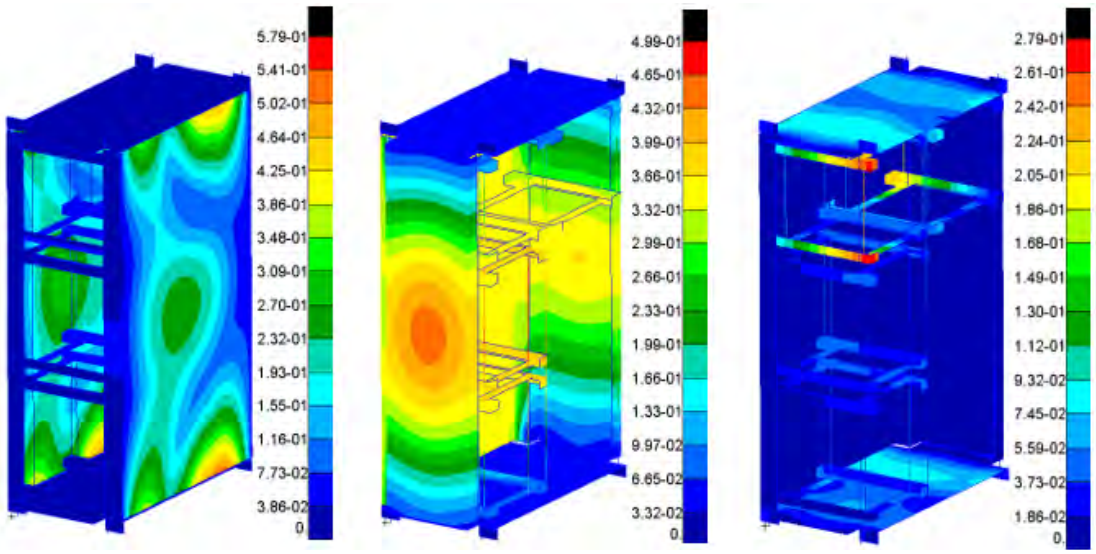


Figure 77: RMS Displacements [mm] for the Y-Axis Loading Case (X-Component [left], Y-Component [middle], Z-Component [right])

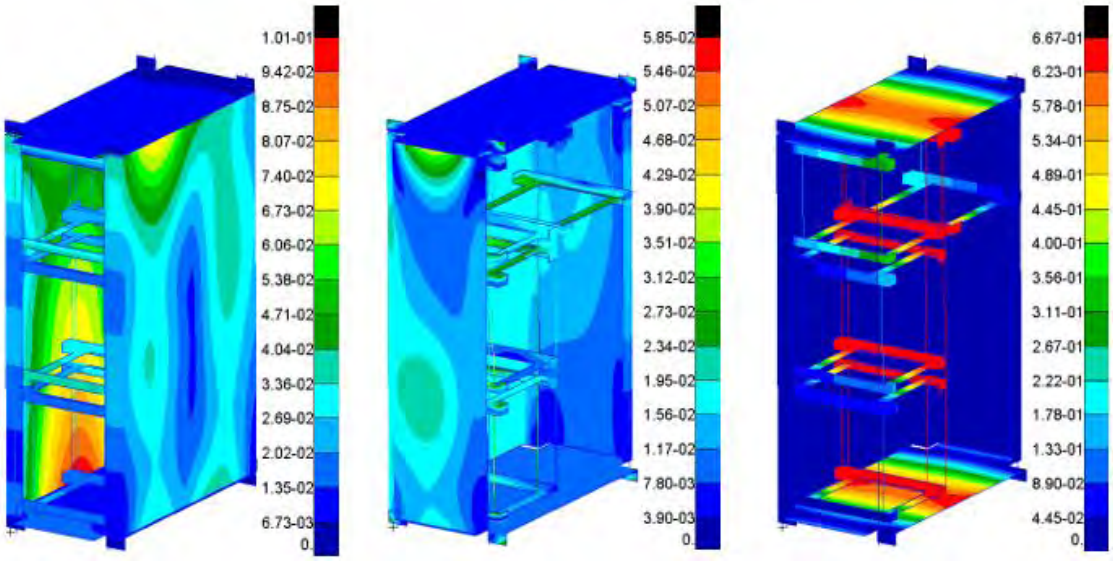


Figure 78: RMS Displacements [mm] for the Z-Axis Loading Case (X-Component [left], Y-Component [middle], Z-Component [right])

It is clear that the maximum nodal displacements are relatively small, with the only exception being the X-Axis loading case, in which the X-Component of the RMS displacement takes the value of 1.25mm. At this point, it is worth mentioning that each result of an RMS analysis reflects a statistical and not a physical quantity, hence describing a standard deviation of the outputs (displacements,

accelerations and stresses) and not their actual value. Furthermore, the 3-sigma (three standard deviations) philosophy indicates 99.73% likelihood that the real results are less than or equal to the calculated value, while the 3-sigma result values are approximately equal to 3-times the calculated result [49].

In the next step, some additional RMS analyses are carried out, with the aim of extracting the behavior of the stresses. It should be noted that the current FEA software, during the implementation of every random analysis, allowed only the calculation of the RMS von Mises and the maximum combined RMS bar stresses. Thus, only the behavior of the aluminum components (rails, rods and decks) can be checked and subsequently presented. Generally, all the calculated stresses lay within the acceptable limits given the strength of the aluminum parts. The worst-case scenario is the X-Axis loading case, during which the maximum RMS von Mises stress occurs near the front right hole of the upper big deck, equaling with 247 MPa. As for the composite panels, no valid conclusions can be drawn, hence it is proposed to re-model the present structure in another FEA-software, which has the ability to adequately capture the behavior of the composites (in terms of stresses or failure indexes or strength ratios), under a random load input.

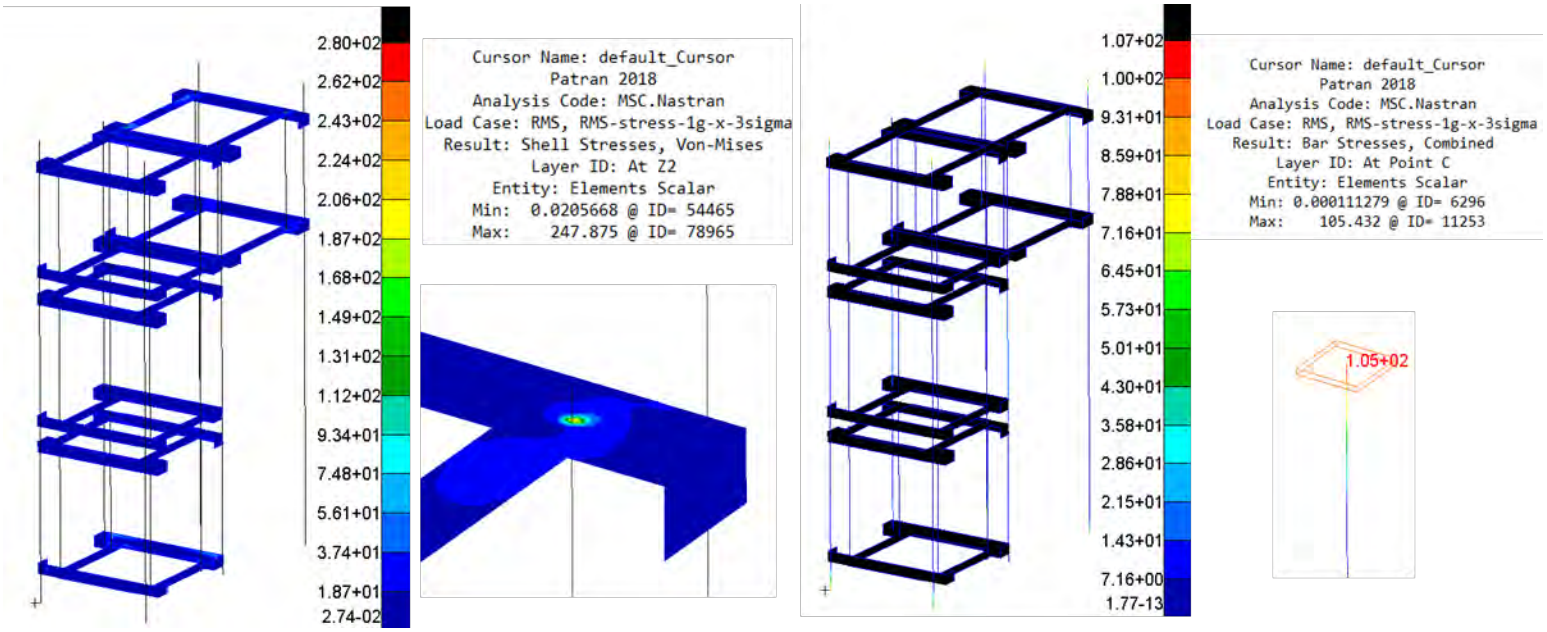


Figure 79: RMS von Mises Stresses [MPa] (left) and Maximum Combined RMS Bar Stresses [MPa] (right) of the X-Axis Loading Case

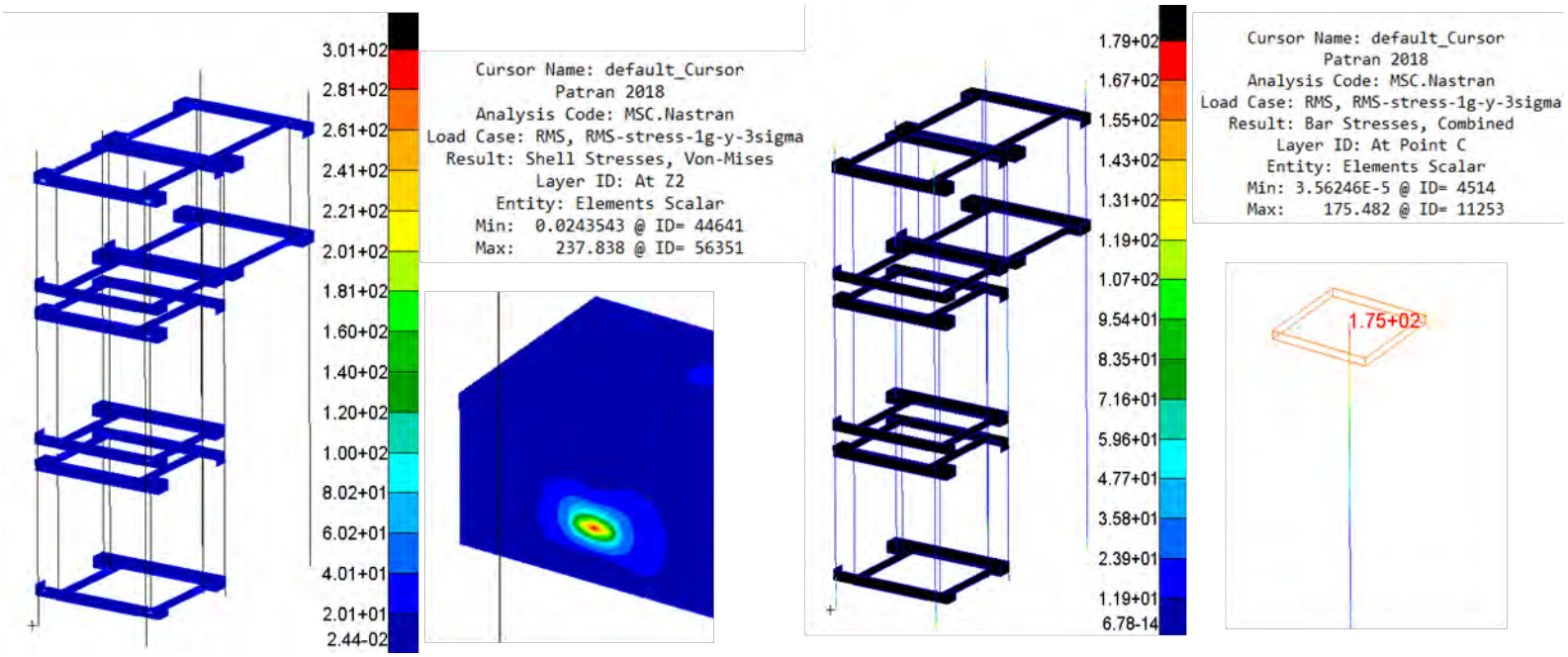


Figure 80: RMS von Mises Stresses [MPa] (left) and Maximum Combined RMS Bar Stresses [MPa] (right) of the Y-Axis Loading Case

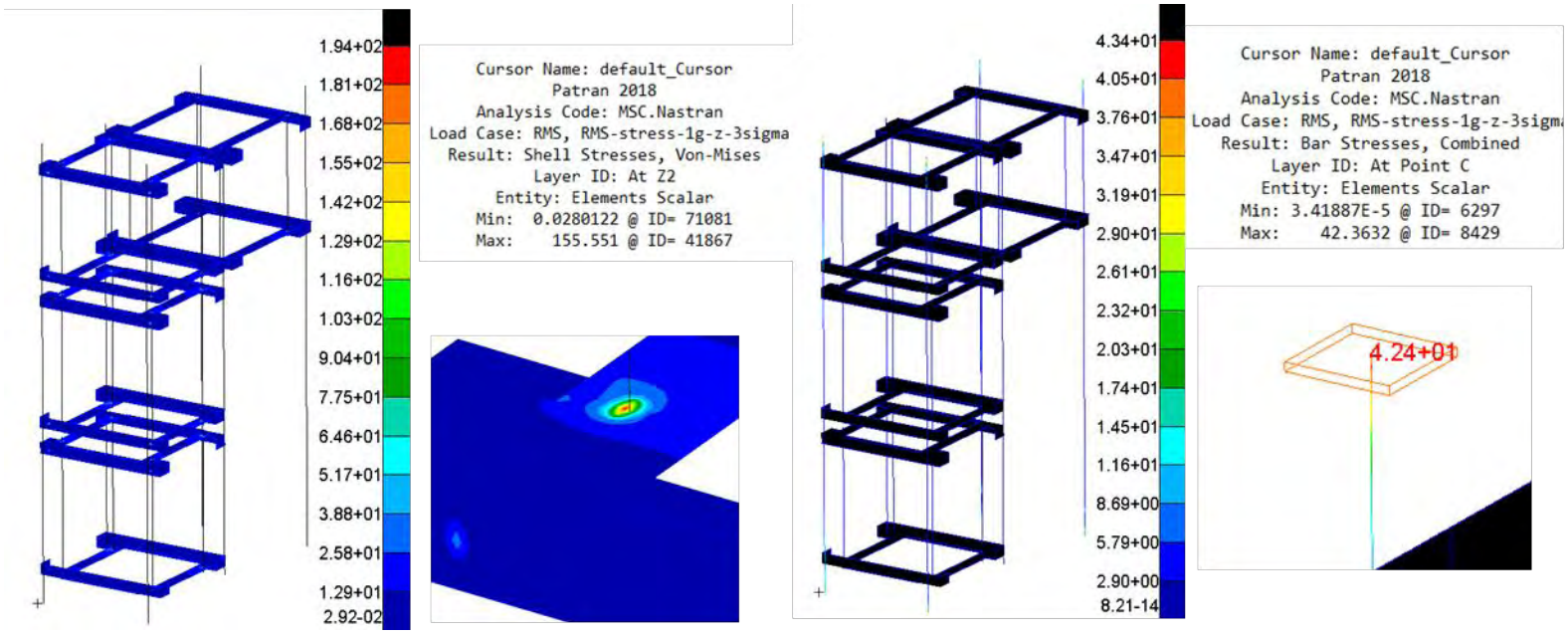


Figure 81: RMS von Mises Stresses [MPa] (left) and Maximum Combined RMS Bar Stresses [MPa] (right) of the Z-Axis Loading Case

4.0 OPTIMIZATION

This chapter deals with the optimization of the previously designed structure, through the use of both different composite materials and stacking sequences in the CubeSat's panels. In the first phase, a comparison is made between the already existed hybrid structure and a geometrically similar to it, which however consists of aluminum panels. Subsequently, chassis walls made of graphite/epoxy system are appropriately tested with the aim of further reducing the total satellite's weight. In the end, the stacking sequence of the finally selected composite is properly changed in order to achieve optimal results in terms of both modal and strength behavior.

4.1 Comparison Between Aluminum and Hybrid Structures

At this point, after an appropriate modification of the existing FE model, composite panels are replaced with aluminum ones, which also have a thickness of 2mm, with the intention of highlighting the advantages of using composites over metals in aerospace applications. One of the most distinctive assets of composite materials is that they form lightweight structures capable of providing the desired structural performance, hence enabling the increase of mass budget used in other subsystems. According to Figure 82, the full-aluminum structure weights about 2.7 kg, presenting an increase of 43.5% concerning the initial hybrid structure (1.89 kg).

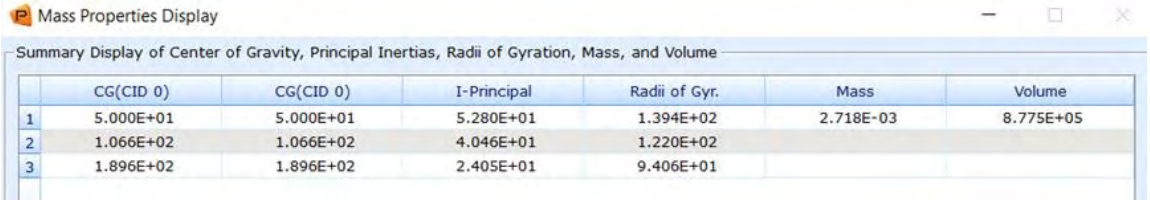


Figure 82: Center of Gravity position (mm), Mass (tons) and Volume (mm^3) of the Full-Aluminum Structure

Following the same philosophy of subchapter 3.4, the normal mode analysis of the aluminum structure is performed and the first 10 natural frequencies are presented in Table 8. It is noteworthy to mention that the fundamental frequency receives a value of 158.57 Hz, which, although smaller, is very close to the relevant one (159.16 Hz) of the hybrid structure. This phenomenon occurs due to the fact that the decks, which remain the same in both cases, continue to have the smallest stiffness to density ratio, hence they oscillate first and lead to almost similar fundamental frequencies. As can be seen from Figure 83, decks drag the bases to take some shape, while in contrast to prior structure, it seems that the aluminum main panel is also affected at this specific frequency, thus leading to the small reduction of the 1st natural frequency. Additionally, it is crucial to note that the upcoming frequencies, at which mode shapes of bending type are developed only in the panels of the chassis wall, are significantly lower than those of the hybrid structure. Everything already stated, confirms the overall better modal behavior of the structure that consists of composite panels and highlights the use of composites over aluminum in such applications.

Table 8: The first 10 Natural Frequencies of the Full-Aluminum Structure

No	Natural Frequency [Hz]	Type
1	**158.57**	Bending
2	160.86	Bending
3	161.08	Bending
4	198.37	Bending
5	198.69	Bending
6	267.14	Bending
7	267.51	Bending
8	311.55	Torsional
9	317.4	Torsional
10	357.82	Torsional

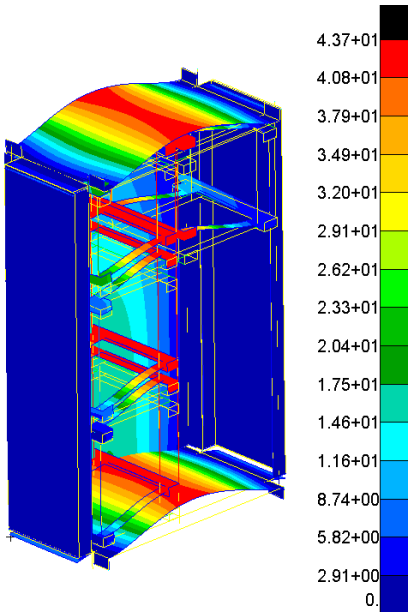


Figure 83: Fundamental Frequency's Mode Shape of the Full-Aluminum Structure

At the next stage, the full-aluminum structure is simulated during the worst quasi-static scenario (-30g along Y-Axis) and its results are compared with the hybrid system ones. It should be noted that no buckling test was performed as this type of analysis calculates extremely high safety margins as already mentioned in page 102. According to Table 9, it is obvious that the structure with composite panels made of CFRP-T300/Fibredux914 presents generally better stress-results compared to the full-aluminum chassis. The only exception is the fact that the full-metal system computes slightly higher safety margins, with their minimum value tending to be equal to 3.3. It is known that in every optimization process, a trade-off situation is occurred, which involves diminishing one property of a designed structure (e.g., decrease of safety margins) in return for gains in other aspects, such as the reduction of the total mass. Nonetheless, the abatement of the safety margin can be considered negligible as detailed commented in page 96, a fact that once again supports the preference for composite materials.

Table 9: Comparison between Hybrid and Aluminum Structures based on the Worst Quasi-Static Scenario

Comparison between Hybrid and Aluminum Structures based on the Worst Quasi-Static Scenario (2nd Load Case)		
	CFRP T300/Fibredux 914	**Aluminum 7075-T6**
CubeSat's Mass [Kg]	**1.893**	**2.718**
Displacement [mm]	0.102	0.105
Stress – Decks (von Mises) [MPa]	20.811	31.395
Stress – Intermediate Rails [MPa]	4	3.895
Stress – Rails and Threaded Rods [MPa]	31.78	42.931
MOS – CFRP (Tsai-Wu-EPFS)	1.655	-
Stress – Panels (von Mises) [MPa]	-	151.054
Worst Safety Margins – Aluminum Parts	15.82	3.3
Worst Safety Margins - CFRP	2.655	-
Worst Safety Margins – All Parts	2.655	3.3

4.2 Optimized Hybrid Structure made of UD Celion GY-70/Epoxy

At this subchapter, an optimization of the present hybrid structure will be carried out, using unidirectional layers of graphite/epoxy system in the modelling of the satellite's panels. It is noted that the following procedure is limited to the composite components, as the aluminum ones remain standardized in dimensions and cannot be changed in order to remain functional. Furthermore, composite parts have a greater research interest in the topic of optimization, as they constitute the most critical elements and directly affect, to a much larger extent, the overall behavior of the CubeSat .

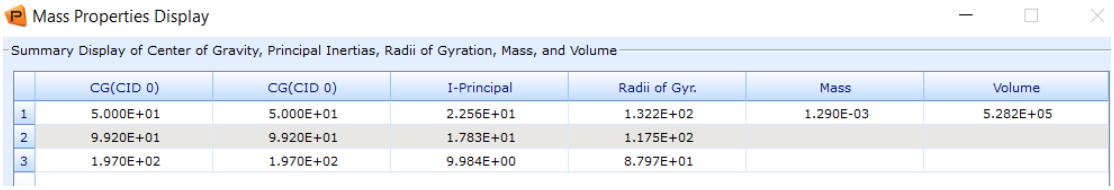
It is important to point out that optimization is an iterative process of finding an optimal solution, which in the present case reflects the minimum weight of the satellite. This procedure is considered anything but simple, as many and independent factors should be taken into account during its implementation. A

typical example is the availability of composites, which limits the final stacking sequence to specific choices of both material properties and thicknesses of each layer, according to the ECSS standards for space approved materials [35]. Moreover, it is important to emphasize that the chassis walls should be reinforced in all directions so that they will be able to receive all the external loads regardless of the placement of the CubeSat inside the POD. Thus, also in this case, the choice of a quasi-isotropic layup, which should be similar for identical components considering the need of structural symmetry, is a one-way road. Beyond the above and given the weight reduction compared to the initial hybrid structure, the final solution should also provide acceptable results in both modal and strength analyses. All the aforestated lead to a final optimized structure, that follows strict standards and regulations, meeting the needs of space industry, without proposing computational solutions that are unfeasible to be manufactured.

At the beginning of the iterations and relying on the initial hybrid structure, a $\pi/4$ quasi-isotropic layup [0/45/90/-45]2S, which was common for each composite panel, was appropriately tested. It is crucial to note that according to Appendix A, the thickness of each GY-70/Epoxy ply is much smaller than the CFRP ones, equaling to 0.06mm, hence in this particular case every composite panel had a total thickness of 0.96mm. The total weight of the CubeSat was reduced by 28.7%, equaling with 1.348 kg, however the finite element analyses calculated again considerably high safety margins, which indicated the ability of the structure to receive further optimization.

Afterwards, every composite component was modelled through a 12-layer layup ([0/45/90/90/-45/0]S), which was inspired by the structural design of the DeorbitSAIL project's 3U CubeSat [46]. The total weight of the satellite was cut down to 1.219 kg, but its modal behavior presented a rather low fundamental frequency of the order of 94 Hz, which is below the allowed limit of 100 Hz, causing the alarm of a resonance condition. It is worth mentioning that the 1st eigen-mode occurred only in the main panels of the CubeSat, confirming that they constituted the most critical elements of the current modal behavior, having the smallest stiffness to mass ratio.

Based on the above observations, an appropriate increase of the plies number, which form the stacking sequence of the composite main panels, was carried out, with the main objective of increasing their stiffness and subsequently shifting the first natural frequency of the entire structure to desired levels. The final lamination chosen for the main panels is the 16-layer layup ([0/45/90/-45]2S), which besides the CFRP structure, was also tested at the beginning of the current iterative process and presented acceptable results, as it not only adequately reinforced all the directions, but also reduced the total mass to a considerable extent. As for the composite bases and side panels, they follow the aforementioned 12-layer layup ([0/45/90/90/-45/0]S), having a total thickness of 0.72 mm, since they did not participate in the first eigen-mode shape, as well as they calculated fair-to-middling safety margins during the quasi-static analyses. According to Figure 84, the final optimized hybrid structure weighs about **1.29 kg**, showing a mass reduction of 31.7% comparing to the initial CFRP-Aluminum one.


Mass Properties Display

Summary Display of Center of Gravity, Principal Inertias, Radii of Gyration, Mass, and Volume

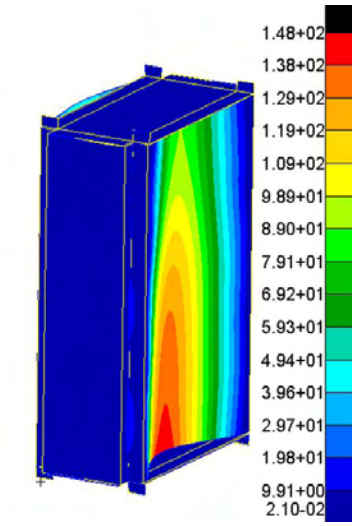
	CG(CID 0)	CG(CID 0)	I-Principal	Radii of Gyr.	Mass	Volume
1	5.000E+01	5.000E+01	2.256E+01	1.322E+02	1.290E-03	5.282E+05
2	9.920E+01	9.920E+01	1.783E+01	1.175E+02		
3	1.970E+02	1.970E+02	9.984E+00	8.797E+01		

Figure 84: Center of Gravity position (mm), Mass (tons) and Volume (mm3) of the Optimized Hybrid Structure

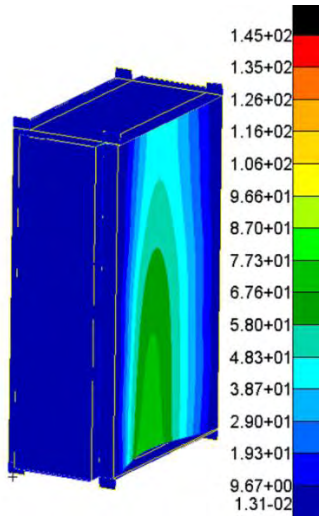
Thereafter, using the Shifted Block Lanczos Method, the first 10 natural frequencies of the optimized CubeSat are calculated and presented in Table 10. As it can be seen, the fundamental frequency equals with 126.8 Hz, hence meeting the appropriate specifications referred to the satellite's modal behavior. It is also noticeable the decrease of all frequencies in relation to the initial structure, a fact that is mainly due to the small thickness of plies used in the current laminates. Regarding the eigen-modes, the first 2 appear to affect only the main panels, which was actually expected from the conclusions of the previous simulations.

Table 10: The first 10 Natural Frequencies of the Optimized Hybrid Structure

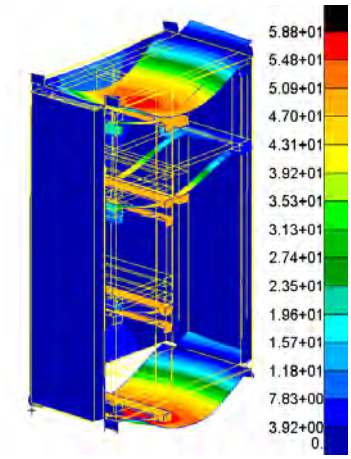
No	Natural Frequency [Hz]	Type
1	**126.80**	Bending
2	126.97	Bending
3	141.75	Bending
4	149.44	Bending
5	149.87	Bending
6	202.89	Bending
7	203.25	Bending
8	252.13	Torsional
9	263.97	Torsional
10	270.46	Torsional



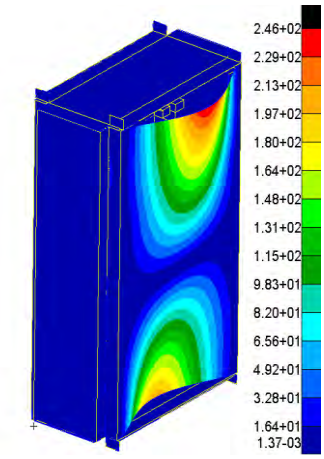
1st Eigen-Mode **[126.8 Hz]**



2nd Eigen-Mode **[126.97 Hz]**



3rd Eigen-Mode **[141.75 Hz]**



4th Eigen-Mode **[149.44 Hz]**

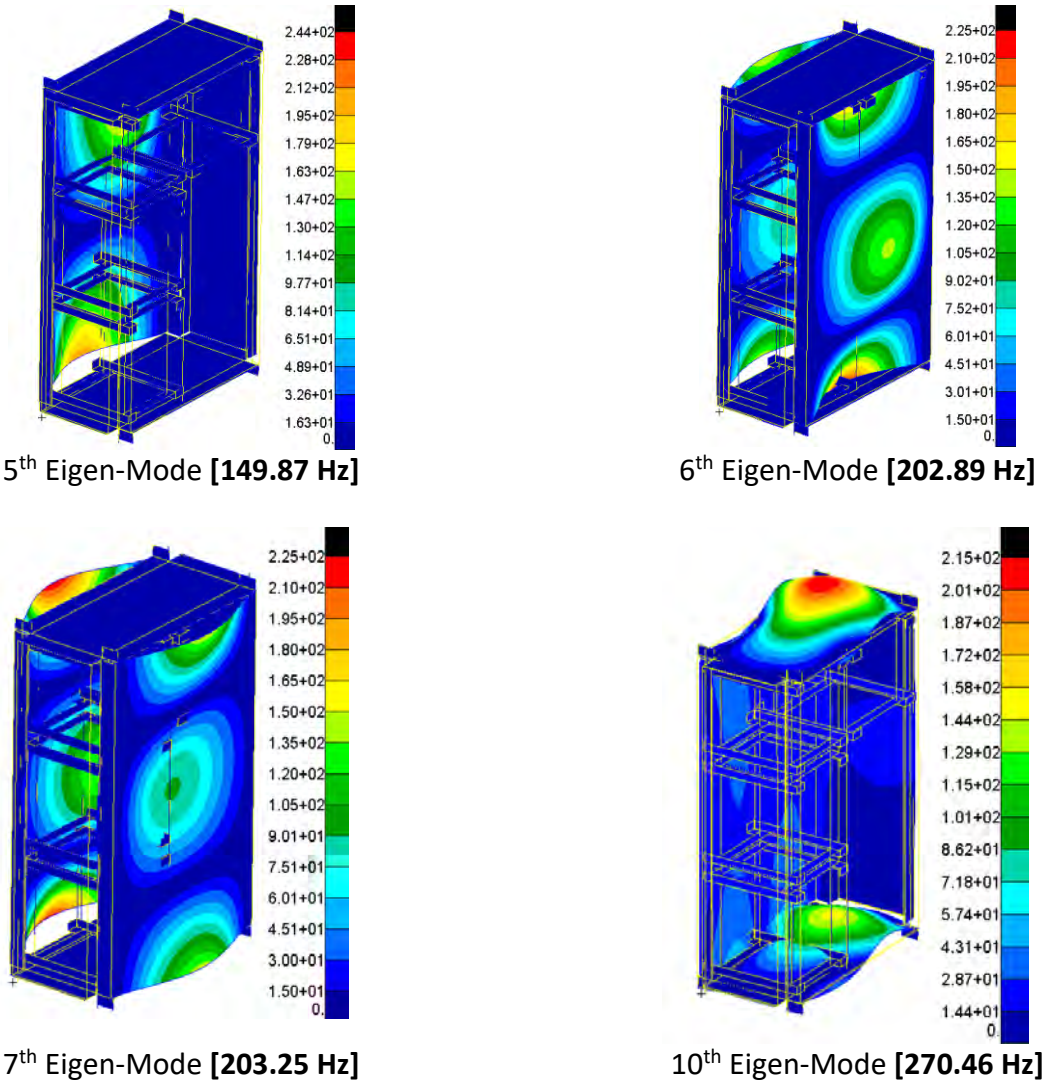


Figure 85: Mode Shapes of the Optimized Hybrid Structure

In the next phase, all the quasi-static simulations of the current optimized structure were carried out, considering, as previously, -30g inertial load applied on each major axis respectively. As for the composite panels, the Tsai-Wu criterion was selected to investigate their disposition to failure, while an interaction F_{12} term, calculated according to EPFS, was chosen because of the epoxy resin that forms the matrix of each lamina. It is also necessary to mention that an FPF-approach was once again followed, indicating the failure of the entire structure as soon as the first, in time period, layer of any lamination fails,

while at the same time it determines the termination of the iterative optimization process. All the required results are summarized in Table 11.

Table 11: Quasi-Static Analyses Results of the Optimized Hybrid Structure (All Cases)

Quasi-Static Analyses of the Optimized Hybrid Structure			
	X-Axis	**Y-Axis**	**Z-Axis**
Displacement [mm]	0.644	0.161	0.495
Stress – decks (von Mises) [MPa]	27.69	29.5	130.97
Stress – intermediate rails [MPa]	6.42	5.44	3.574
Stress – rails and threaded rods [MPa]	31.534	27.785	28.364
MOS – GY70/Epoxy (Tsai-Wu-EPFS)	0.326	**0.055**	0.384
Worst Safety Margins – aluminum parts	15.95	17.05	3.84
Worst Safety Margins – GY70/Epoxy	1.326	1.055	1.384
Best case scenario Moderate case scenario Worst case scenario			

In the first place, it is noticeable that the maximum nodal displacements have increased, fact that indicates the reduction of the overall structure's stiffness compared to the initial CFRP-Aluminum one. Considering the very small panel thicknesses of the present FEA model, a non-linear static simulation could have been carried out, however given the load and the initial safety factors, the above results are accepted. As far as the aluminum components are concerned, they range almost at the same stress levels in relation to the non-optimized hybrid model, presenting very large safety margins. Hence, it is verified, once again, that the most critical components, which will absorb the greater part of the external loads, are the composite panels. Regarding them, it is observed an acute reduction in the MOS of all the scenarios, which was actually expected due to the FPF-approach in the optimization process.

After a further examination, it is noticed that in the 1st case (X-Axis loading) MOS takes a value of 0.326, appearing in the first, from the bottom, RBE2 connection of the left side panel's front flange and more specifically in the second ply, according to the manufacturing operation, which corresponds to a 45^{o} layer of its lamination. It is important to mention that the worst safety margins of this particular case express

the ability of the CubeSat to be further optimized, as it can receive larger loads, however, as it is already referred, the unknown placement of it inside the POD creates an imperative necessity for appropriately responding in all loading conditions without failing.

Moving on to the 3rd case (Z-Axis loading), the calculated MOS equals to 0.384, becoming the highest of all the scenarios, due to the fact that the aluminum decks receive quite a lot of the stress field, causing composites to strain less in comparison with the rest of the quasi-static cases. The above minimum MOS locates in the second, from the top, connection of the rear main panel's left flange and corresponds to the penultimate ply, which tallies with a 45° layer. The relatively high safety margins and the generally fair behavior of the current model reveal that the most acceptable placement of the optimized CubeSat is, yet again, along the Z-Axis.

Last but definitely most important case is the 2nd one (Y-Axis Loading), which based on the extracted results constitutes, once again, the worst possible scenario. This specific model presents both small nodal displacements and insignificant von Mises-stresses in the aluminum parts, however it calculates the smallest and most crucial MOS of the entire process, making the current case the most interesting to comment on. The value of 0.055 may be marginal, tending to be very close to failure, however, remains acceptable as MOS > 0. According to Figure 87, it appears in the first, from the top, connection of the rear main panel's left side and more accurately in the penultimate layer, according to the manufacturing process, which agrees with a 45° ply. As it can be seen in Figure 86, a more intense tendency to failure becomes apparent comparing to the corresponding results (Figure 58) of the initial hybrid structure. Hence, it is confirmed that despite the mass optimization, a trade-off situation prevails, causing a significant reduction in the safety margins. Through a more detailed look, it is again confirmed that mainly the RBE2 connections, which witness the existence of holes in the original CAD-Model, and secondarily the abrupt changes in geometry, constitute the most critical areas of the structure, presenting the lowest margins of safety.

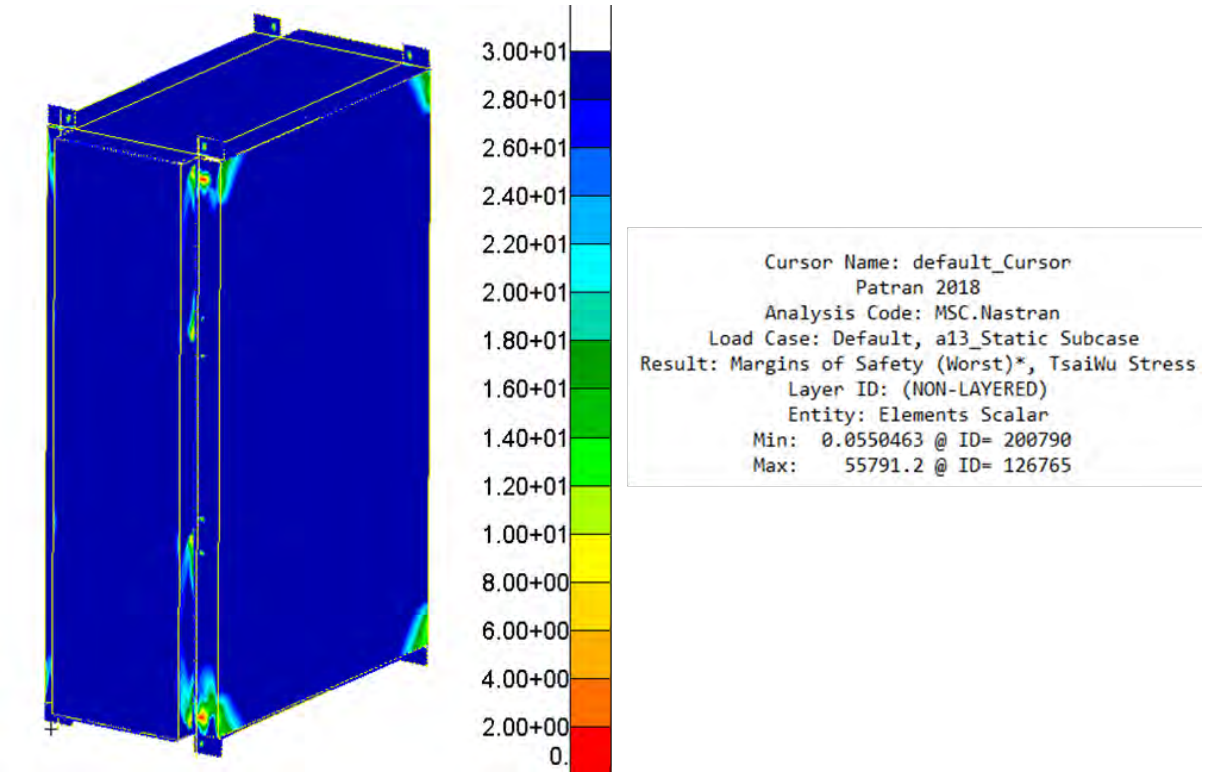


Figure 86: Worst Margins of Safety (MOS) of Composite Parts (Tsai-Wu-EPFS Criterion) during the Worst-Case Scenario (Y-Axis Loading) of the Optimized Hybrid Structure

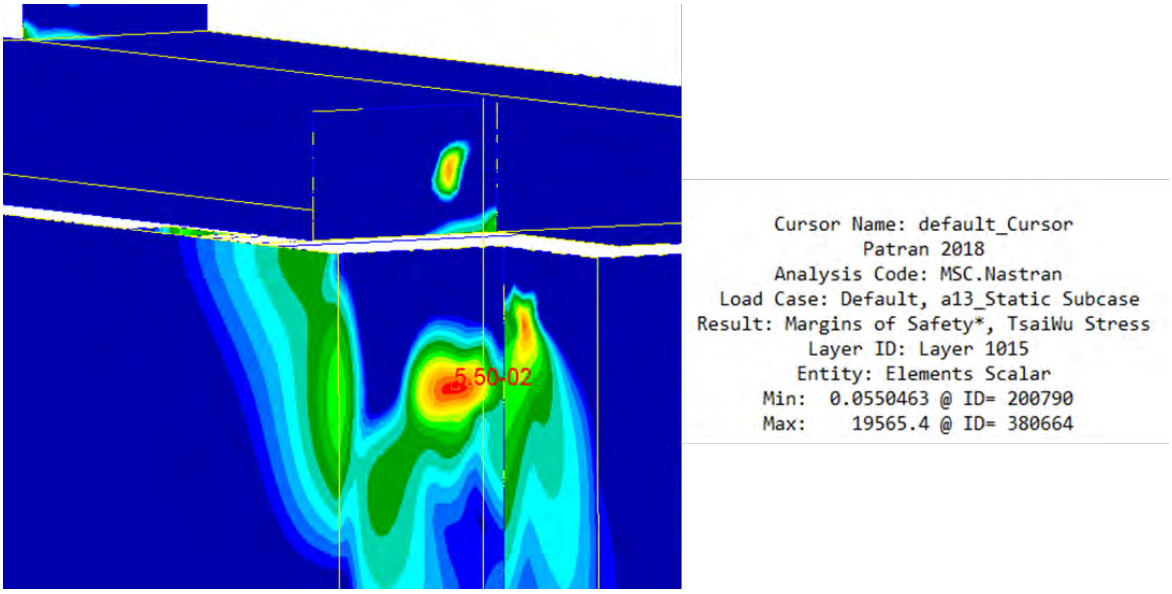


Figure 87: Minimum Margin of Safety detail during the Worst-Case Scenario (Y-Axis Loading) of the Optimized Hybrid Structure

4.2.1 Optimization Remarks

Delving a little further into the philosophy of the above optimization process, it is worth noting that the worst calculated MOS = 0.055, still has room for improvement, at least theoretically. As it has already been understood, the mass reduction is achieved by removing appropriate layers from certain laminated components of the entire structure. Hence, a further weight loss entails an additional burden on the composites, which are already in a limit-state-design, meaning that every small change in the final structure can lead to failure, according to FPF-approach.

A representative example is a pilot FEA-model, similar to the one presented previously, with the only difference being in the stacking sequence of both the side panels, following an 8-layer ([0/45/90/-45]S) lamination. After the appropriate simulations, the worst-case scenario presented a MOS = -0.027, which is calculated on the exact same finite element as the one illustrated in Figure 87. Thus, indicating a crucial sensitivity level of the present model, according to which slight changes in a seemingly independent component (side panel) affect the behavior of the entire satellite, leading to the failure of a different composite part (main panel), that has not changed its lamination in relation to the previous optimization step.

Beyond the risk of failure, hidden in an additional procedure of removing layers in the finally selected FEA-model, it is worth emphasizing that the entire optimization process is driven to a saturation state, according to which the total weight of the CubeSat changes henceforth to an insignificant rate. As shown in the diagrams below, the weight is mostly shifted to the aluminum parts, becoming the heaviest of the entire structure, while due to the appropriate requirements they cannot be changed. It is also characteristic that all the composites take up almost half the weight of the aluminum components, a fact that confirms the aforementioned and officially terminates the optimization process.

Table 12: Mass List of the Optimized Hybrid Structure

	Components	Mass			
		kg	%	kg	%
Aluminum	Decks	0.3967	31	0.8329	65
	Rails	0.287	22		
	Threaded Rods	0.1492	11		
Composites	Main Panels	0.2835	22	0.45727	35
	Side Panels	0.1003	8		
	Bases	0.07347	6		
	Total	**1.29017**	**100**		

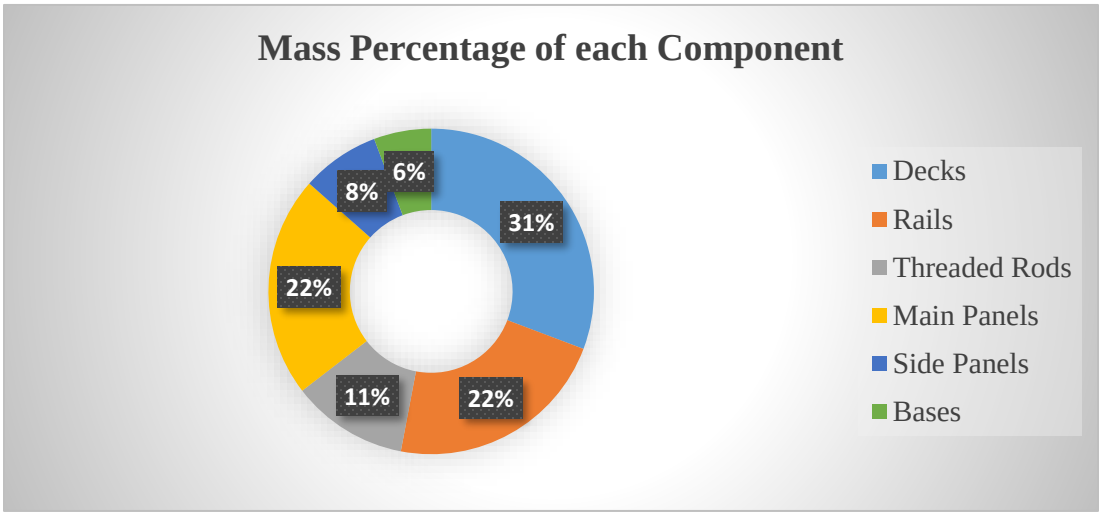


Figure 88: Mass Percentage of each Component of the Optimized Hybrid Structure

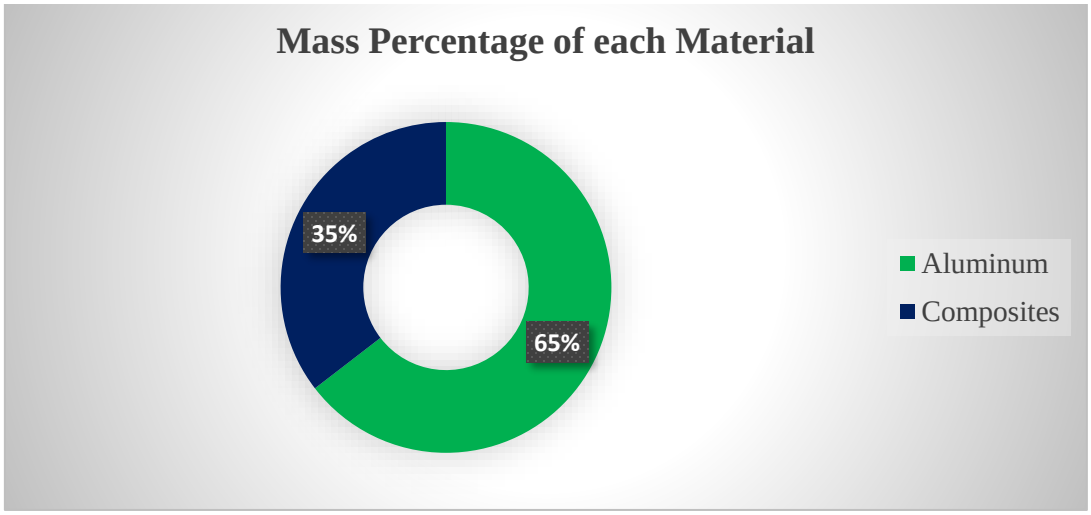


Figure 89: Mass Percentage of each Material used in the Optimized Hybrid Structure

To conclude, in the present chapter it was demonstrated that the use of graphite/epoxy laminate composites, which are characterized by appropriate stacking sequences, are capable of reducing the total mass of the CubeSat to a great extent. Nevertheless, the procedure followed continues to move within empirical frameworks, according to which the designer judges himself the termination of the iterative processes. It should be noted that the strict concept of optimization is based on suitable mathematical algorithms that accurately calculate the optimal solution of a design problem. However, the fact that all the analyses are required to present acceptable results, the large number of finite elements that discretize the structure, the specifications as well as the uncertainties and simplifications of the FEA-model, make the above problem quite demanding. Over and above that, the total mass of composites changes henceforward to a negligible degree, as previously mentioned, which renders the above procedure unnecessary. Lastly, it should be noted that a topology optimization of the aluminum parts could possibly lead to a further weight reduction, however a better FEA-model, consisted of 3D solid elements with the appropriate holes, is definitely needed for the extracted results to be as accurate as possible. Such a process cannot be applied in laminated composites, as the removal of material creates discontinuities in the fibers, destroying their load bearing capacity, with the result that calculating the optimal thicknesses and orientations, becomes the only way to optimize laminated components. All of the above were presented to highlight the fact that the optimization performed, did not necessarily reveal the best but an improved alternative to the initial hybrid structure, setting the stage for a future re-engagement with the present topic.

5.0 CONCLUSIONS AND DISCUSSION

5.1 Conclusions

Coming to the end of the present Diploma Thesis, it can be said that it fulfills its initial purpose as it carries through with the innovative hybrid design of a 6U-XL CubeSat's structure, which also includes an appropriate free inner-space for the transportation of a deployable robotic arm. It is worth mentioning that this specific space can also be used by other components instead of the robotic arm, as long as they do not occupy more than the available free volume (105 x 120 x 200 mm^3).

As already mentioned, the design was an iterative process of transition from the CAD to the FEA model and vice versa. Firstly, the final CAD model is presented in detail, while the reference to the assembly method is also noteworthy. Afterwards, the hybrid structure is modeled in the MSC PATRAN/NASTRAN environment, based on some assumptions and simplifications. In the first place, normal modes analyses are carried out, showing that the first natural frequency, which equals to 159.16 Hz, sits comfortably above the 100 Hz minimum resonant frequency, according to the requirements. Thereafter, the quasi-static analyses confirm the sufficient strength, based on FPF-approach, of the entire structure, while indicating that the optimal placement of the CubeSat, inside the POD, is along its Z-Axis. Additionally, linear buckling analyses calculated very high safety margins, hence confirming that the satellite will not be led to a possible loss of its mechanical stability. Besides that, random vibration analyses are also carried out, showing that the RMS stresses, at least for the aluminum pieces, move at acceptable levels. Lastly, an attempt is made to improve the present hybrid structure through the use of GY-70/Epoxy laminated panels, which presented a total mass reduction of 31.7%. The whole process, however, is not based on any algorithm and moves in empirical frameworks.

5.2 Future Work

All in all, the entire structure can be considered adequately robust, while the current work can proceed to the next stage of building a prototype with the aim of verifying the results of the above computer simulations. However, the whole thesis concept can be further examined. Firstly, a locking mechanism should be installed for the deployable panel, which will be able to activate its movement in space. Also, a more innovative design of the two composite bases, that could contain more points of contact with the rails, may give more rigidity to the chassis, while it is also necessary to deal with the electronic systems. At this point, it must be noted that a further work on the design of the satellite or a possible placement of secondary components (such as solar panels or antennas), will affect the original CAD model, thus a new iterative design process is required, in order to export the final product. As far as the FEA model is concerned, a more appropriate meshing technique could be made . More specifically, it is generally recommended to use 3D-Solid elements for the discretization of both the aluminum decks and the rails, so that the boundary conditions can be more accurately applied. Such a procedure would be easier to follow through a direct import of the CAD model into the FEA software environment, which would also allow the accurate modelling of the entire geometry including holes. In terms of the simulations, the main focus point is dealing with thermal effects, which play a crucial role when the satellite is in orbit. It is also important to investigate the composite parts behavior during the random vibrations, event that could not happen in the post-processor of the MSC PATRAN. Finally, in terms of optimization, an algorithmic campaign (parametric design) would be interesting, however it remains complex due to the multiple analyses that should be carried out as well as the strict standards that the geometry must follow.

REFERENCES

[1] "U. o. W. Science Learning Hub – Pokapū Akoranga Pūtaiao," [Online].

[2] ESA, 2014. [Online]. Available: https://www.esa.int/ESA_Multimedia/Images/2014/09/Rosetta_and_its_target_comet#.YeNwA6ifY1s.link.

[3] U. Nations, "Office for Outer Space Affairs," [Online]. Available: https://www.unoosa.org/oosa/osoindex/index.jspx?lf_id=..

[4] "CubeSats: A bright future for nanosatellites," [Online]. Available: https://www.researchgate.net/publication/226944864_CubeSats_A_bright_future_for_nanosatellites.

[5] [Online]. Available: https://onlinelibrary.wiley.com/doi/pdf/10.1002/9781119971009.fmatter.

[6] [Online]. Available: https://www.nanosats.eu.

[7] Radius Space, [Online]. Available: www.radiusspace.com.

[8] [Online]. Available: https://www.youtube.com/watch?v=CzP8S3ZHyKY&ab_channel=TylerDoering.

[9] "6U CubeSat Design Specification PROVISIONAL," [Online]. Available: https://explorers.larc.nasa.gov/APMIDEX2016/MO/pdf_files/12-6U_CDS_2016-05-19_Provisional.pdf.

[10] ISISPACE, "https://www.isispace.nl/," [Online].

[11] T. Philippidis, "Notes of the Subject "Mechanics of Composite Materials"".

[12] C. D. E. Hwai-Chung Wu, "Strengthening of Concrete Structures using Fiber Reinforced Polymers (FRP)," 2017. [Online]. Available: https://doi.org/10.1016/B978-0-08-100636-8.00003-X.

[13] Gurit, "GUIDE TO COMPOSITES," [Online]. Available: www.gurit.com.

[14] "Composites Design - Guidelines," [Online]. Available: https://www.ist.edu.pk/downloads/amss/lecturers/design-guidelines.pdf.

[15] "DragonPlate," 25 November 2019. [Online]. Available: https://dragonplate.com/carbon-fiber-101-what-do-isotropic-quasi-isotropic-and-anisotropic-mean.

[16] A. Catinaccio, "Modelling Composite Materials: Introduction to ESAComp," CERN EP-DT, 2016. [Online]. Available: https://slideplayer.com/slide/10600241/.

[17] A. B. A. K. V. K. A. Ampatzoglou, "Qualification of composite structure for CubeSat picosatellites as a demonstration for small satellite elements," *International Journal of Aeronautical Science & Aerospace Research (IJASAR)*, October 2014.

[18] "QB50_Systems_Requirements_issue_7".

[19] "Open Source - Greek CubeSat," [Online]. Available: https://upsat.gr/?page_id=9.

[20] A. Ampatzoglou, "Design - Analysis, Optimization and Construction of a Micro-Satellite for the Study of Lower Thermosphere and Re-Entry conditions," in *PhD Dissertation*, Patras, 2017.

[21] "Small Spacecraft State of the Art Report 2015 - Scientific Figure on ResearchGate.," [Online]. Available: https://www.researchgate.net/figure/The-6U-Supernova-Structure-Kit-Image-courtesy-of-Pumpkin-Inc-2015b_fig62_289527097.

[22] "nanoavionics," [Online]. Available: https://nanoavionics.com/cubesat-components/cubesat-structural-frame/.

[23] "satsearch," [Online]. Available: https://satsearch.co/products/aac-clyde-zaphod-6u-structure.

[24] [Online]. Available: https://www.endurosat.com/.

[25] [Online]. Available: https://cervos.space/.

[26] [Online]. Available: https://www.npcspacemind.com.

[27] "Gomspace," [Online]. Available: https://gomspace.com/shop/subsystems/structures/6u-structure.aspx.

[28] Y. Byeloborodov, "2U CUBESAT STRUCTURAL DESIGN AND INTEGRATION," Faculty of the College of Science Morehead State University, 2017.

[29] [Online]. Available: https://www.mcmaster.com/.

[30] S. H. S. K. P. O. S. B. J. S. a. P. H. Adam Thurn, "A nichrome burn wire release mechanism for cubesats," Proceedings of the 41st Aerospace Mechanisms Symposium, Jet Propulsion Laboratory, 2012.

[31] ECSS, "Structural materials handbook," [Online]. Available: http://escies.org/ftp/ecss.nl/Handbooks/ECSS-E-HB-32-20_Part1A.pdf.

[32] "Common Lay Common Lay-up Terms and Conditions," [Online]. Available: https://www.usna.edu/Users/mecheng/pjoyce/composites/Short_Course_2003/7_PAX_Short_Course_Laminate-Orientation-Code.pdf.

[33] SIEMENS, "The Shifted Block Lanczos Method," [Online]. Available: http://www2.me.rochester.edu/courses/ME204/nx_help/index.html#uid:id476911.

[34] J. A. E. A. (JAXA), "JEM Payload Accommodation Handbook - Vol. 8 - Small Satellite Deployment - Interface Control Document," [Online]. Available: https://www.unoosa.org/documents/pdf/psa/hsti/KiboCUBE/JEM_Payload_Accommodation_Handbook.pdf.

[35] ECSS, "Space engineering - Structural general requirements," [Online]. Available: http://everyspec.com/ESA/download.php?spec=ECSS-E-ST-32C_REV-1.048195.pdf.

[36] E. C. L. M. R. G. R. Giorgio Capovilla, "Modular Multifunctional Composite Structure for CubeSat Applications: Preliminary Design and Structural Analysis," *Aerospace,* February 2020.

[37] N. M. M. P. d. Andrada, "Infante's Structural Model: Preliminary Design Process and Analysis," *Master Thesis,* June 2019.

[38] M. B. V. Guedes, "Cubesat Structural and Thermal Analysis Methodology ISTsat-1 Design," *Master Thesis,* June 2019.

[39] R. Talreja, "On Failure Theories for Composite Materials," in *Advanced Methods of Continuum Mechanics for Materials and Structures*, 2016, pp. 379-388.

[40] S. W. T. a. E. M. Wu, "A General Theory of Strength for Anisotropic Materials," 1971.

[41] R. a. H. M. A. Narayanaswami, "Evaluation of the Tensor Polynomial and Hoffman Strength Theories for Composite Materials," Journal of Composite Materials, Vol. II, 1977, p. 366.

[42] P. S. T. a. T. P. Philippidis, "The Paraboloidal Failure Surface of Initially Anisotropic Elastic Solids," 1987, pp. 378-395.

[43] SIEMENS, "NX Nastran User's Guide," [Online]. Available: https://docs.plm.automation.siemens.com/data_services/resources/nxnastran/10/help/en_US/tdocExt/pdf/User.pdf.

[44] C. Stocchi, "Investigation on the mechanical behaviour of single-lap composite joints with countersunk bolts," Imperial College London, 2013.

[45] J. Akin, "Buckling Analysis," [Online]. Available: https://www.clear.rice.edu/mech403/HelpFiles/FEA_Buckling_analysis.pdf.

[46] "Random Analysis, S14-1 NAS122, Section 14," MSC.Software, August 2005. [Online]. Available: http://www.myshared.ru/slide/886647/.

[47] I. Dima, "Comparative study between random vibration and linear static analysis using Miles method," in *International Workshop on Numerical Modelling in Aerospace Sciences, NMAS*, Bucharest Romania, 2017.

[48] *NASA STD 5001B – STRUCTURAL DESIGN AND TEST FACTORS OF SAFETY.*

[49] Autodesk, 30 October 2019. [Online]. Available: https://knowledge.autodesk.com/support/inventor-

nastran/troubleshooting/caas/sfdcarticles/sfdcarticles/How-to-interpret-random-vibration-analysis-results-from-Nastran-and-Simulation-Mechanical.html.

[50] "University of Surrey," [Online]. Available: https://www.surrey.ac.uk/surrey-space-centre/missions/deorbitsail.

[51] SatPy. [Online]. Available: https://www.satpy.com/product/1-u-frame/.

[52] ZAPHOD-1U, "SatCatalog," [Online]. Available: https://www.satcatalog.com/component/zaphod-1u/.

[53] P.-. s. systems. [Online]. Available: https://www.pumpkinspace.com/store/p30/Chassis_Walls.html.

[54] C. Scott, "3D Printing Lattice Structures for a More Lightweight CubeSat Bus".*3DPrint.com.*

APPENDIX A

Composite Materials Properties according to ECSS Standards for Space Projects

9.4.4 T300/ Fibredux 914

Table 9.4-5 - Data sheet for UD carbon HT/epoxy (Ciba Geigy 914C-TS-5-42)

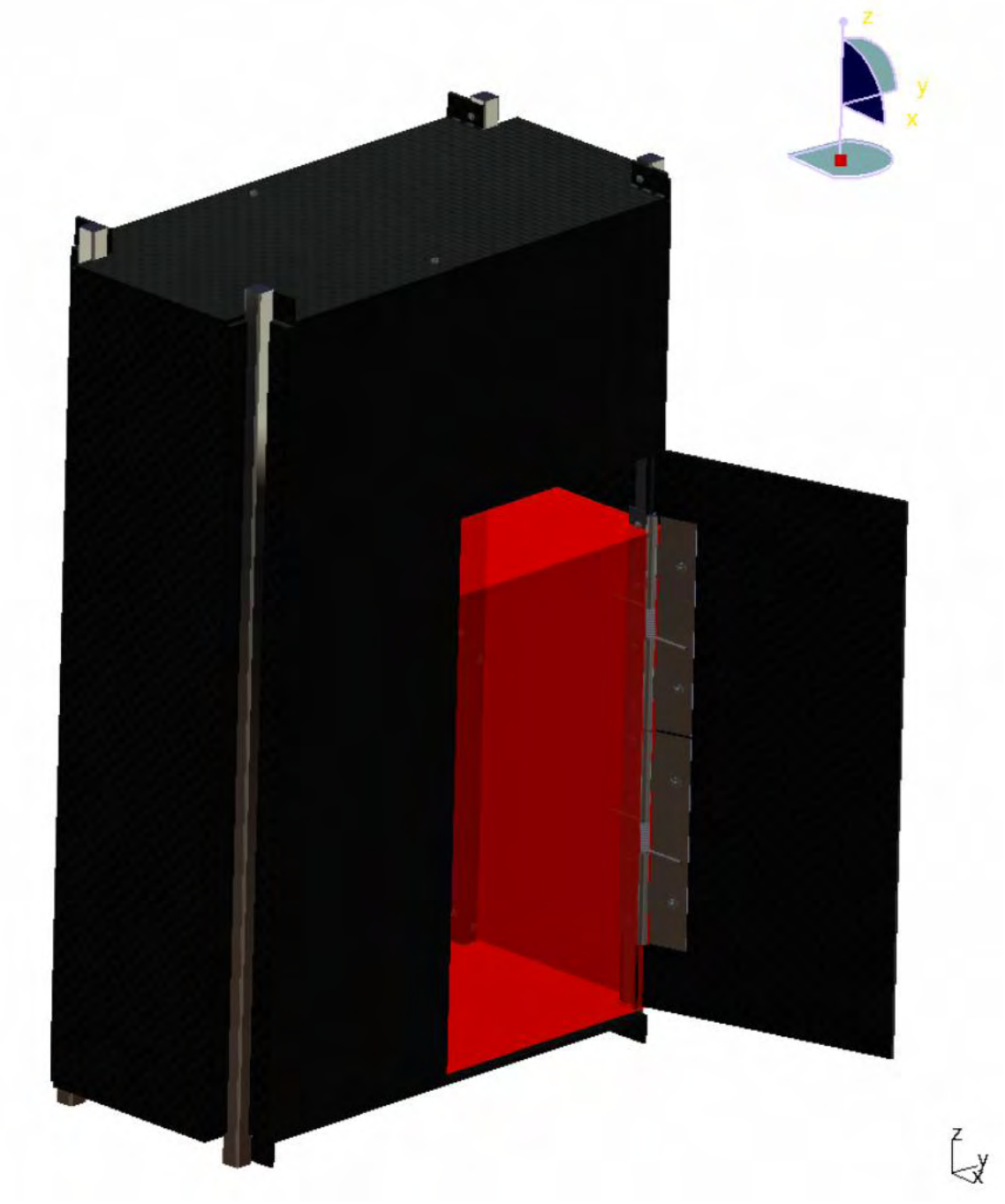
Supplier/Trade Name Ciba Geigy 914C-TS-5-42		Fibre/Resin System T300 (3K) Epoxy: Fibredux 914		Data Source 4
Fibre vol (%): 61.5		t_{ply} (mm): 0.125		Density (kg/m^3): 1580
Areal weight (g/m^2): 225			Year of test: 1985	
Specimen condition: Autoclave cure cycle. 1 hr - 120°C, 1 hr - 175°C, pressure 3.5 bar, vacuum 20 mbar.				
Test environment: 20°C		$\overline{X}$	S.D.	N
Tension:	E_x (GPa)	138.1	7.3	5
ASTM D3039-76	σ_x (MPa)	1573	117	5
	ε_x (%)	1.07	0.07	5
	E_y (GPa)	8.92	0.36	5
	σ_y (MPa)	36.6	6.0	5
	ε_y (%)	0.42	0.07	5
Compression:	E_x (GPa)	120.6	0.82	6
ASTM D3039-76	σ_x (MPa)	-	-	-
	ε_x (%)	-	-	-
	E_y (GPa)	10.25	0.91	6
	σ_y (MPa)	-	-	-
	ε_y (%)	-	-	-
Poisson's ratio: D3039	ν_{xy}	0.37	0.02	5
Shear:	G_{xy} (GPa)	4.97	0.24	5
ASTM D3518-76	τ_{xy} (MPa)	87.0	0.77	5
Interlaminar shear	$\tau_{(0)}$ (MPa)	81.6	5.2	8
(ILSS): I.H.	$\tau_{(0\pm45)}$ (MPa)	-	-	-
Flexural:	$\sigma_{(flex)}$ (MPa)	-	-	-

Table 9.5-3 - Data sheet for UD carbon HM/epoxy (Cyanamid Fothergill: Celion GY70/Code 92)

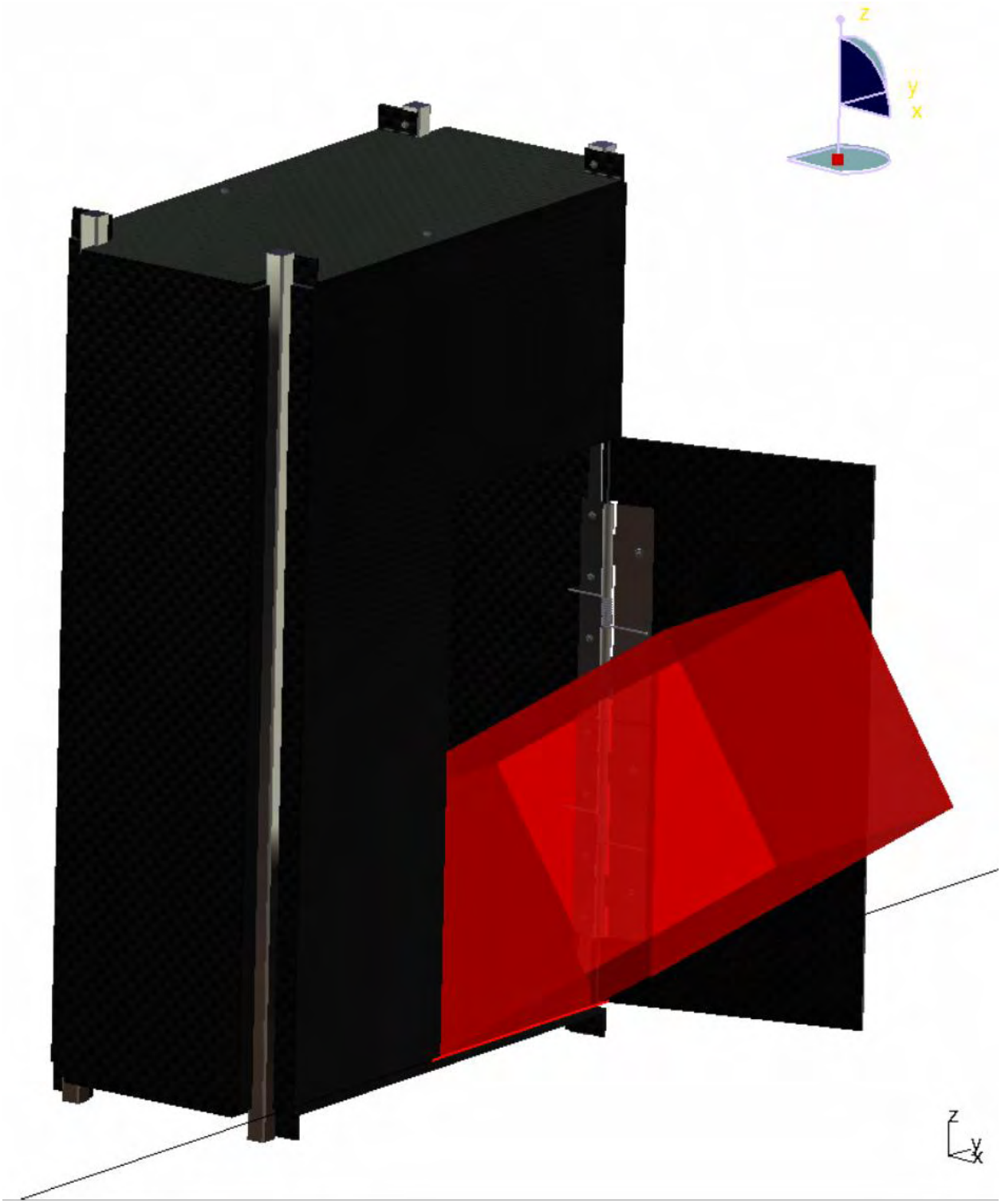
Supplier/Trade Name Cyanamid Fothergill		Fibre/Resin System Celion GY-70 Epoxy: Code 92		Data Source 1
Fibre vol (%): 60	t_{ply} (mm): 0.06		Density (kg/m^{3}): 1600	
Areal weight (g/m^{2}): -			Year of test: -	
Specimen condition: 120°C cure. Specimen dry.				
Test environment: RT.		$\overline{X}$	S.D.	N
Tension:	E_x (GPa)	300.7	13.0	19
	σ_x (MPa)	711.6	67.3	9
	ε_x (%)	0.223	0.011	9
	E_y (GPa)	5.2	0.3	18
	σ_y (MPa)	8.6	1.7	18
	ε_y (%)	0.368	0.048	18
Compression:	E_x (GPa)	275.8	12.6	20
	σ_x (MPa)	509.6	61.3	20
	ε_x (%)	0.196	0.035	20
	E_y (GPa)	-	-	-
	σ_y (MPa)	-	-	-
	ε_y (%)	-	-	-
Poisson's ratio:	ν_{xy}	0.39	0.019	19
Shear:	G_{xy} (GPa)	3.48	0.34	10
	τ_{xy} (MPa)	-	-	-
Interlaminar shear	$\tau_{(0)}$ (MPa)	47.3	4.3	20
(ILSS):	$\tau_{(0\pm45)}$ (MPa)	-	-	-
Flexural:	$\sigma_{(flex)}$ (MPa)	767.7	30.5	10

APPENDIX B

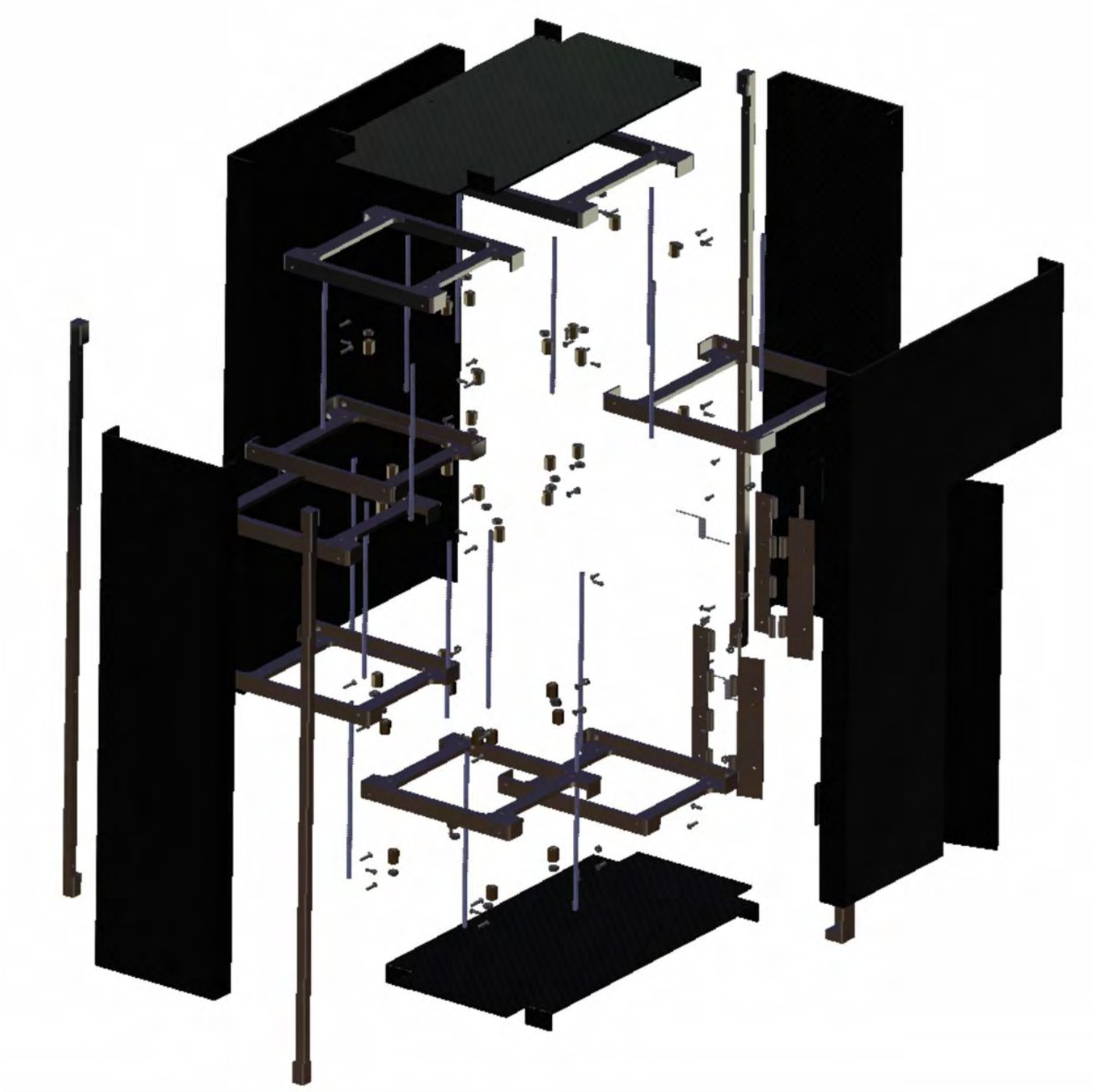
Representation of the payload



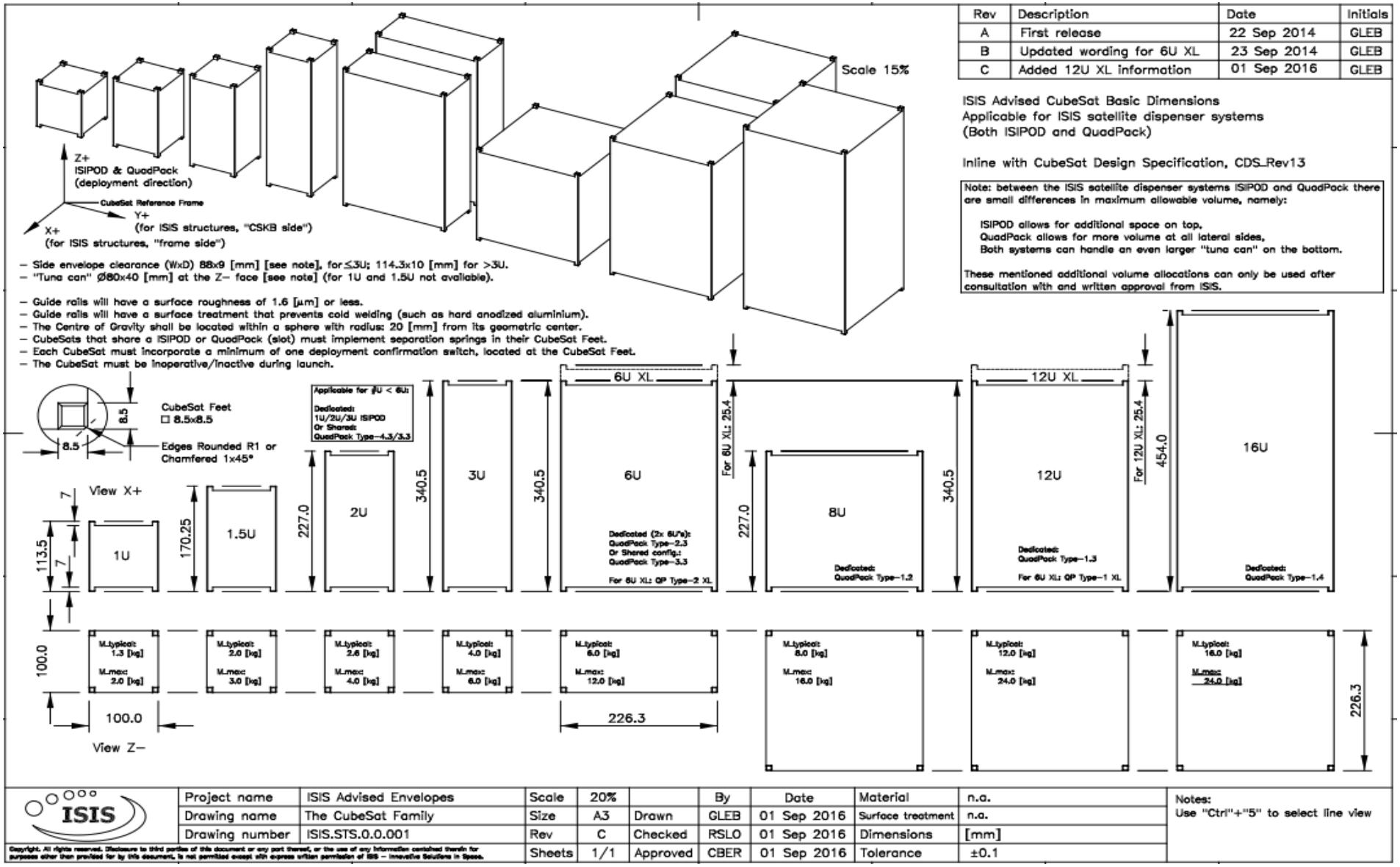
Representation of the payload's deployment



Exploded view



Cubesat Design Specifications Provided By ISISSPACE



Rev	Description	Date	Initials
A	First release	22 Sep 2014	GLEB
B	Updated wording for 6U XL	23 Sep 2014	GLEB
C	Added 12U XL information	01 Sep 2016	GLEB

ISIS Advised CubeSat Basic Dimensions
Applicable for ISIS satellite dispenser systems
(Both ISIPOD and QuadPack)

Inline with CubeSat Design Specification, CDS_Rev13

Note: between the ISIS satellite dispenser systems ISIPOD and QuadPack there are small differences in maximum allowable volume, namely:

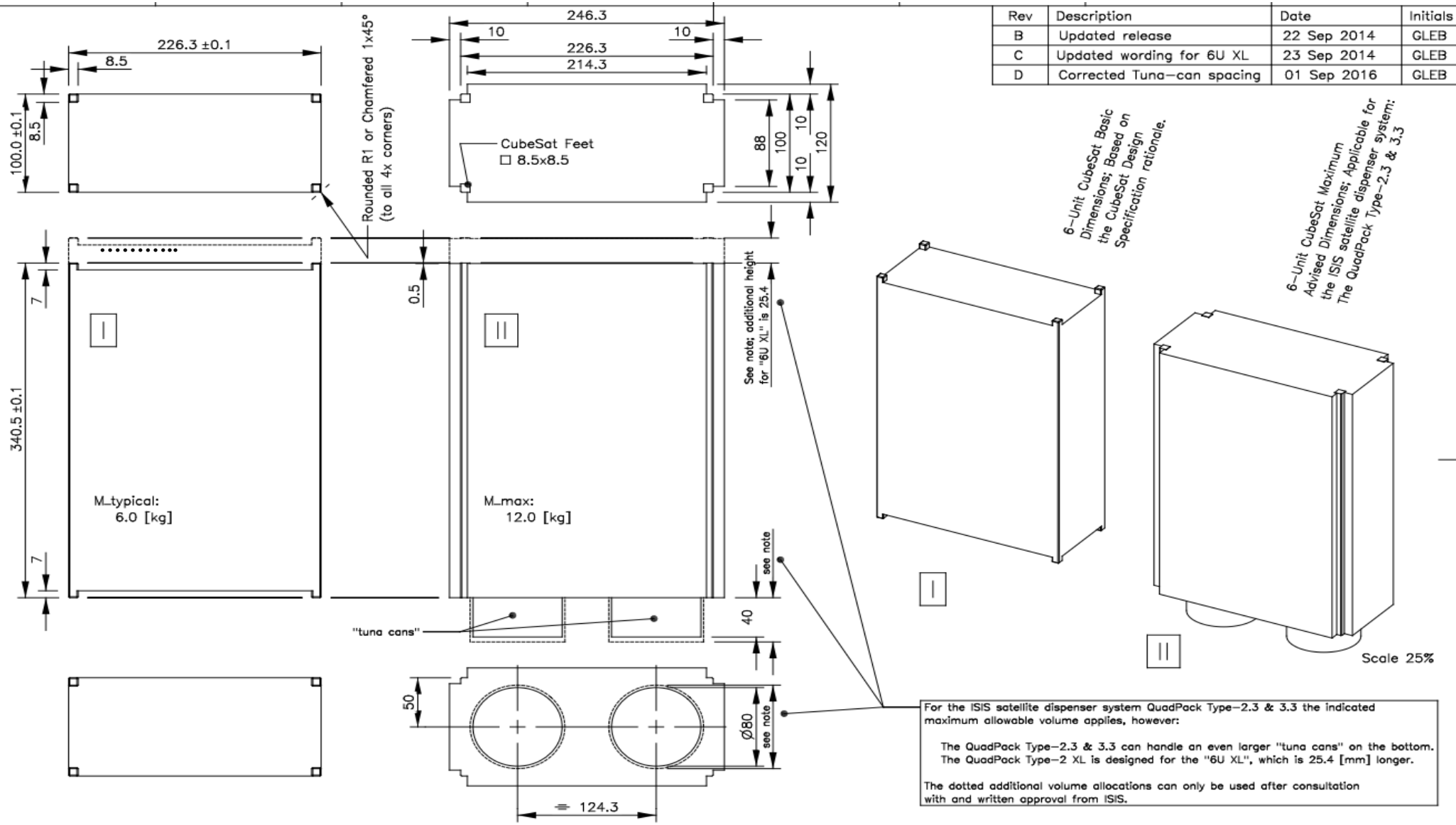
ISIPOD allows for additional space on top.
QuadPack allows for more volume at all lateral sides.
Both systems can handle an even larger "tuna can" on the bottom.

These mentioned additional volume allocations can only be used after consultation with and written approval from ISIS.

ISIS	Project name	ISIS Advised Envelopes	Scale	20%		By	Date	Material	n.a.
	Drawing name	The CubeSat Family	Size	A3	Drawn	GLEB	01 Sep 2016	Surface treatment	n.a.
	Drawing number	ISIS.STS.0.0.001	Rev	C	Checked	RSLO	01 Sep 2016	Dimensions	[mm]
			Sheets	1/1	Approved	CBER	01 Sep 2016	Tolerance	±0.1

Notes:
Use "Ctrl"+"5" to select line view

Copyright. All rights reserved. Disclosure to third parties of this document or any part thereof, or the use of any information contained therein for purposes other than provided for by this document, is not permitted except with express written permission of ISIS – innovative Solutions in Space.



Rev	Description	Date	Initials
B	Updated release	22 Sep 2014	GLEB
C	Updated wording for 6U XL	23 Sep 2014	GLEB
D	Corrected Tuna-can spacing	01 Sep 2016	GLEB

ISIS	Project name	ISIS Advised Envelope	Scale	30%		By	Date	Material	n.a.	Notes: Use "Ctrl"+"5" to select line view
	Drawing name	6-Unit CubeSat Dimensions	Size	A3	Drawn	GLEB	01 Sep 2016	Surface treatment	n.a.	
	Drawing number	ISIS.STS.0.1.006	Rev	D	Checked	RSLO	01 Sep 2016	Dimensions	[mm]	
			Sheets	1/1	Approved	CBER	01 Sep 2016	Tolerance	±0.1	

Copyright. All rights reserved. Disclosure to third parties of this document or any part thereof, or the use of any information contained therein for purposes other than provided for by this document, is not permitted except with express written permission of ISIS – Innovative Solutions in Space.

APPENDIX C

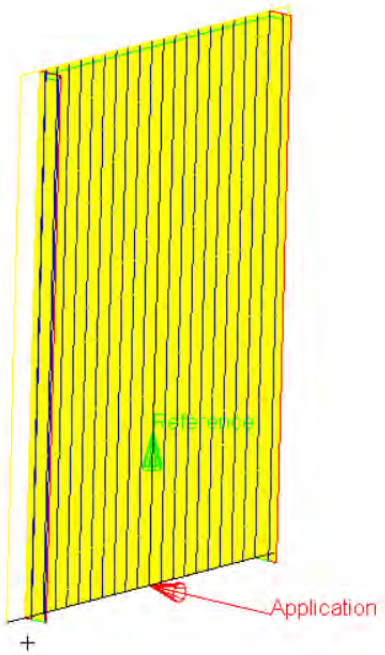
Back Main Panel's Stacking Sequence of the Optimized Hybrid Structure

LM_Layup Definition Summary

Index	LM_Ply	LM_Matl	Thickness	Ref. Angle	Type	Multiplier	Application Direction	Angle Offset
1	Ply_1	Mat_1	0.059999999	0.	Slide	1	Original	0.
2	Ply_2	Mat_1	0.059999999	45.	Slide	1	Original	0.
3	Ply_3	Mat_1	0.059999999	90.	Slide	1	Original	0.
4	Ply_4	Mat_1	0.059999999	-45.	Slide	1	Original	0.
5	Ply_4	Mat_1	0.059999999	-45.	Slide	1	Original	0.
6	Ply_3	Mat_1	0.059999999	90.	Slide	1	Original	0.
7	Ply_2	Mat_1	0.059999999	45.	Slide	1	Original	0.
8	Ply_1	Mat_1	0.059999999	0.	Slide	1	Original	0.
9	Ply_1	Mat_1	0.059999999	0.	Slide	1	Original	0.
10	Ply_2	Mat_1	0.059999999	45.	Slide	1	Original	0.
11	Ply_3	Mat_1	0.059999999	90.	Slide	1	Original	0.
12	Ply_4	Mat_1	0.059999999	-45.	Slide	1	Original	0.
13	Ply_4	Mat_1	0.059999999	-45.	Slide	1	Original	0.
14	Ply_3	Mat_1	0.059999999	90.	Slide	1	Original	0.
15	Ply_2	Mat_1	0.059999999	45.	Slide	1	Original	0.
16	Ply_1	Mat_1	0.059999999	0.	Slide	1	Original	0.

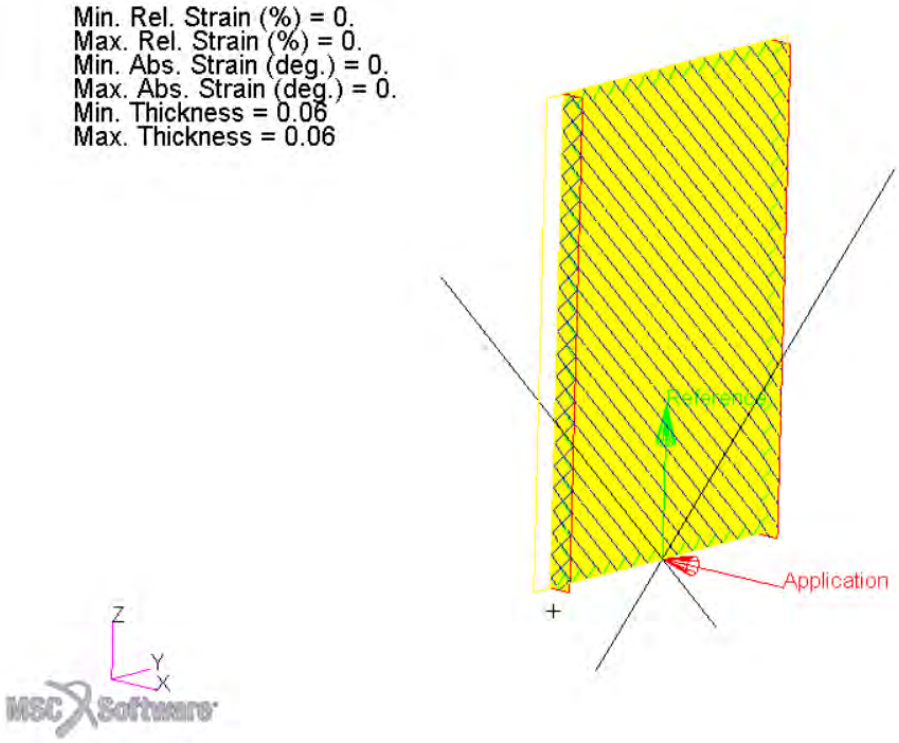
Index	LM_Ply	LM_Matl	Thickness	Ref. Angle	Type	Multiplier	Application Direction	Angle Offset
1	Ply_1	Mat_1	0.059999999	0.	Slide	1	Original	0.

Min. Rel. Strain (%) = 0.
Max. Rel. Strain (%) = 0.
Min. Abs. Strain (deg.) = 0.
Max. Abs. Strain (deg.) = 0.
Min. Thickness = 0.06
Max. Thickness = 0.06

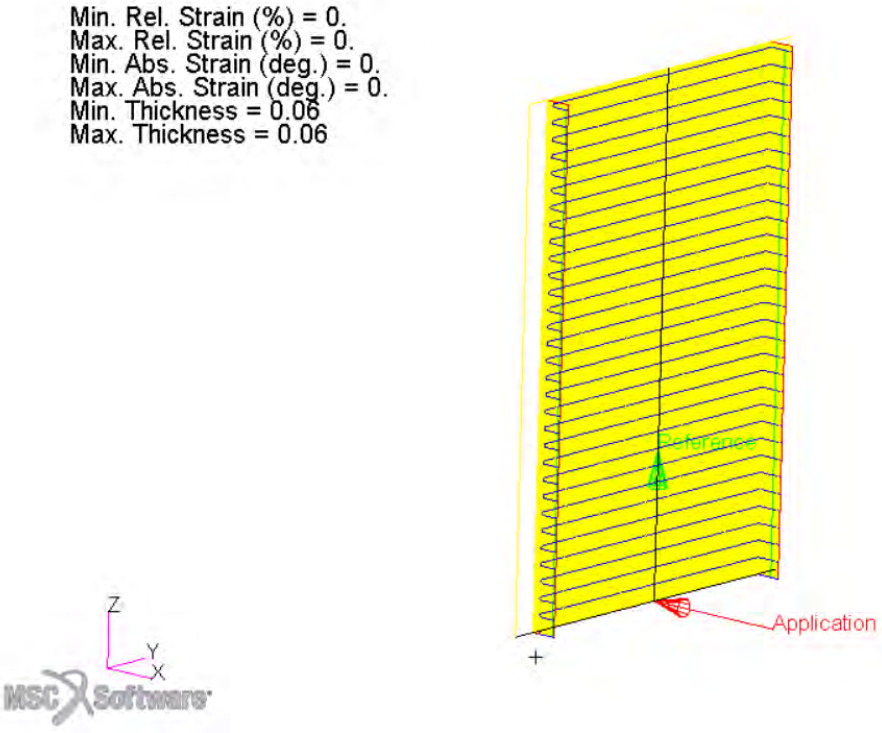




Index	LM_Ply	LM_Matl	Thickness	Ref. Angle	Type	Multiplier	Application Direction	Angle Offset
2	Ply_2	Mat_1	0.059999999	45.	Slide	1	Original	0.

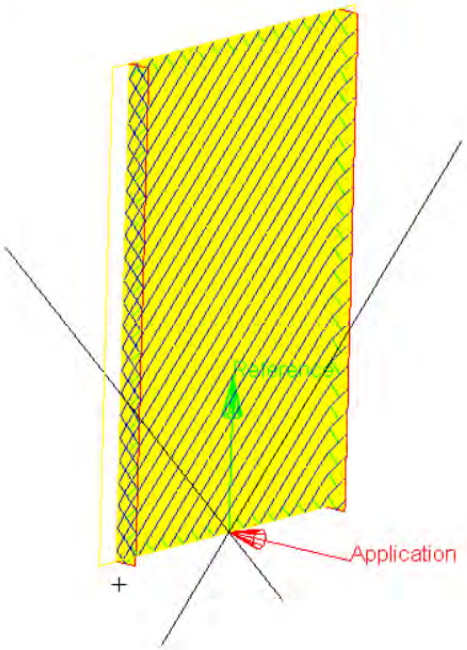


Index	LM_Ply	LM_Matl	Thickness	Ref. Angle	Type	Multiplier	Application Direction	Angle Offset
3	Ply_3	Mat_1	0.059999999	90.	Slide	1	Original	0.



Index	LM_Ply	LM_Matl	Thickness	Ref. Angle	Type	Multiplier	Application Direction	Angle Offset
4	Ply_4	Mat_1	0.059999999	-45.	Slide	1	Original	0.

Min. Rel. Strain (%) = 0.
Max. Rel. Strain (%) = 0.
Min. Abs. Strain (deg.) = 0.
Max. Abs. Strain (deg.) = 0.
Min. Thickness = 0.06
Max. Thickness = 0.06



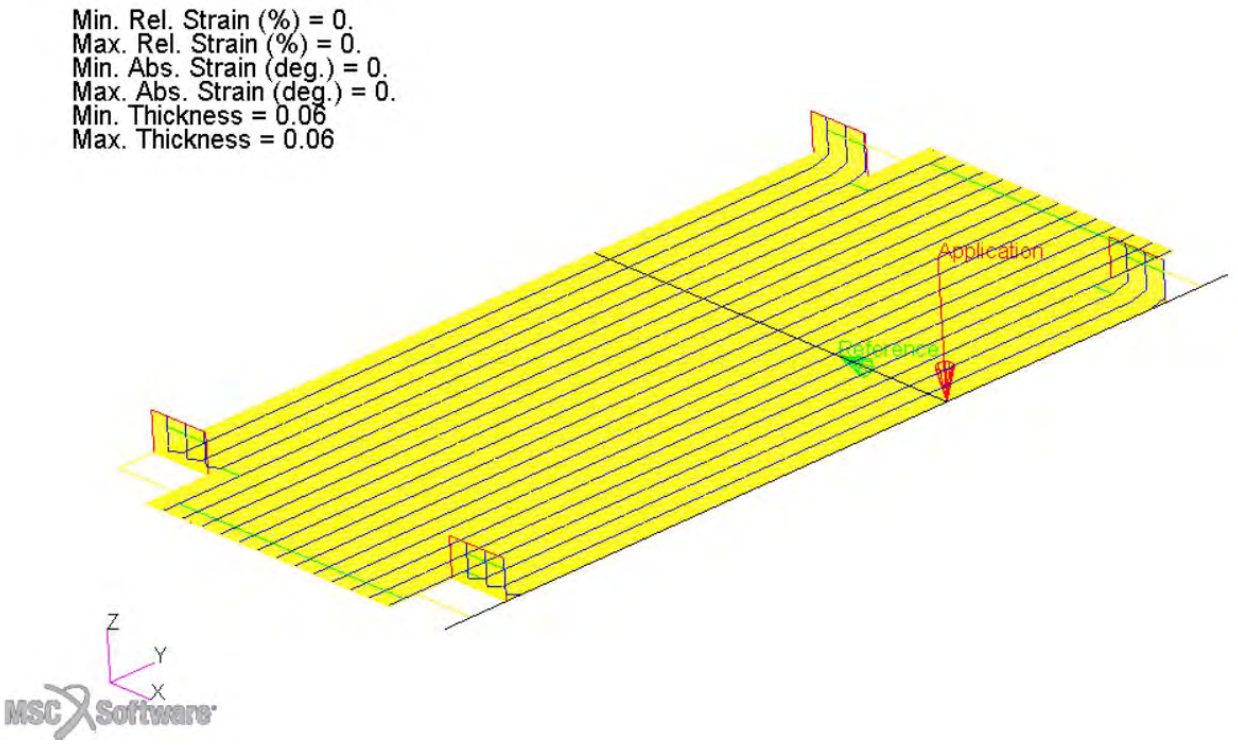


Top Base's Stacking Sequence of the Optimized Hybrid Structure

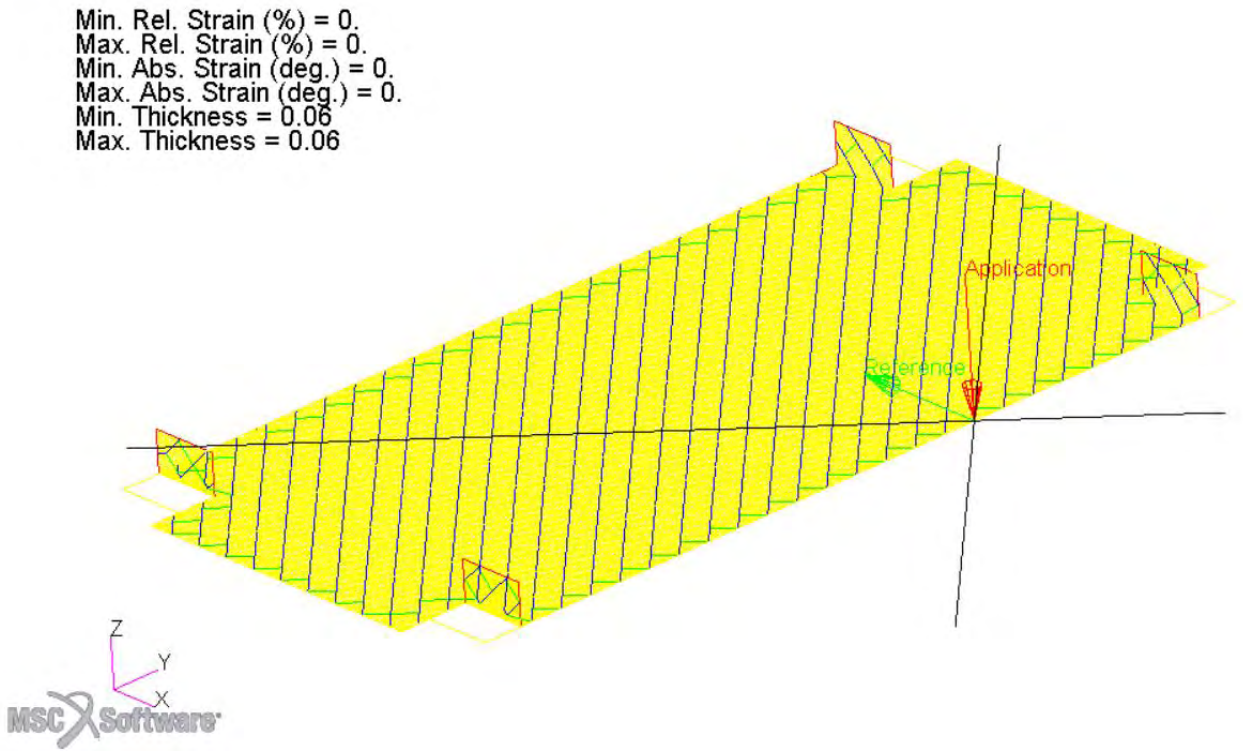
LM_Layup Definition Summary

Index	LM_Ply	LM_Matl	Thickness	Ref. Angle	Type	Multiplier	Application Direction	Angle Offset
1	Ply_22	Mat_6	0.059999999	90.	Slide	1	Original	0.
2	Ply_23	Mat_6	0.059999999	135.	Slide	1	Original	0.
3	Ply_24	Mat_6	0.059999999	180.	Slide	1	Original	0.
4	Ply_24	Mat_6	0.059999999	180.	Slide	1	Original	0.
5	Ply_25	Mat_6	0.059999999	45.	Slide	1	Original	0.
6	Ply_22	Mat_6	0.059999999	90.	Slide	1	Original	0.
7	Ply_22	Mat_6	0.059999999	90.	Slide	1	Original	0.
8	Ply_25	Mat_6	0.059999999	45.	Slide	1	Original	0.
9	Ply_24	Mat_6	0.059999999	180.	Slide	1	Original	0.
10	Ply_24	Mat_6	0.059999999	180.	Slide	1	Original	0.
11	Ply_23	Mat_6	0.059999999	135.	Slide	1	Original	0.
12	Ply_22	Mat_6	0.059999999	90.	Slide	1	Original	0.

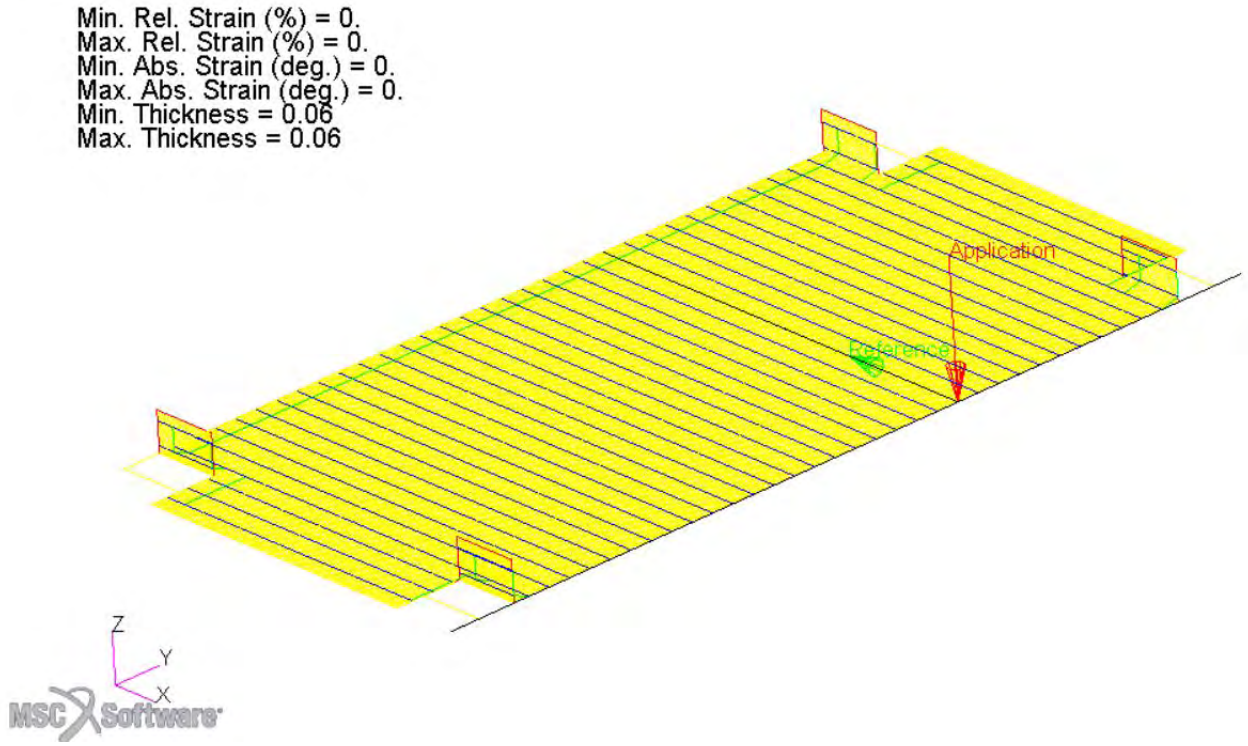
Index	LM_Ply	LM_Matl	Thickness	Ref. Angle	Type	Multiplier	Application Direction	Angle Offset
1	Ply_22	Mat_6	0.059999999	90.	Slide	1	Original	0.



Index	LM_Ply	LM_Matl	Thickness	Ref. Angle	Type	Multiplier	Application Direction	Angle Offset
2	Ply_23	Mat_6	0.059999999	135.	Slide	1	Original	0.



Index	LM_Ply	LM_Matl	Thickness	Ref. Angle	Type	Multiplier	Application Direction	Angle Offset
3	Ply_24	Mat_6	0.059999999	180.	Slide	1	Original	0.



Index	LM_Ply	LM_Matl	Thickness	Ref. Angle	Type	Multiplier	Application Direction	Angle Offset
5	Ply_25	Mat_6	0.059999999	45.	Slide	1	Original	0.

